Master of Science Thesis

Development of the Near Wake behind a Horizontal Axis Wind Turbine

Including the development of a Free Wake Lifting Line Code

M.H.M. Kloosterman

June 17, 2009

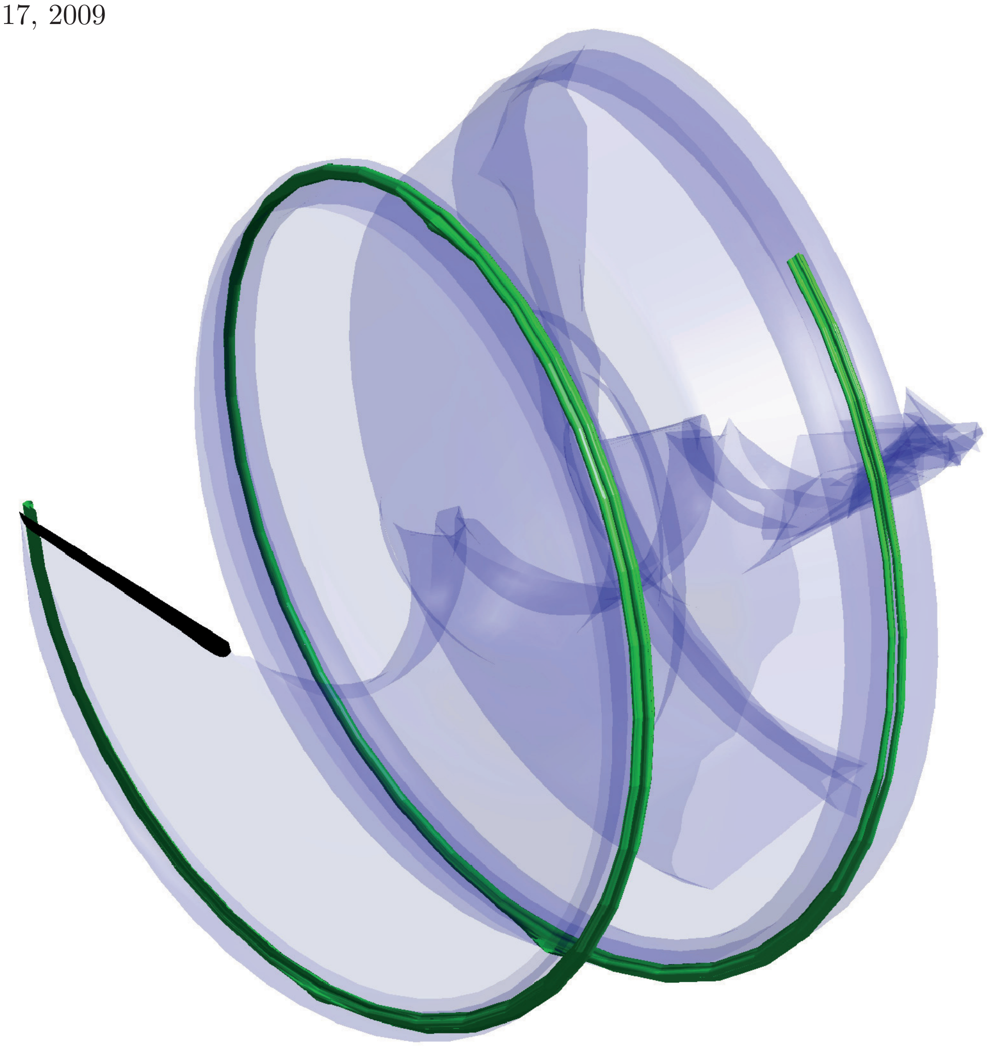

Faculty of Aerospace Engineering

Delft University of Technology

Development of the Near Wake behind a Horizontal Axis Wind Turbine

Including the development of a Free Wake Lifting Line Code

Master of Science Thesis

For obtaining the degree of Master of Science in Aerospace Engineering at Delft University of Technology

M.H.M. Kloosterman

June 17, 2009

Faculty of Aerospace Engineering · Delft University of Technology

Delft University Of Technology
Department Of
Aerodynamics & Wind Energy

The undersigned hereby certify that they have read and recommend to the Faculty of Aerospace Engineering for acceptance a thesis entitled **“Development of the Near Wake behind a Horizontal Axis Wind Turbine”** by **M.H.M. Kloosterman** in partial fulfillment of the requirements for the degree of **Master of Science**.

Dated: June 17, 2009

Supervisor:

prof. dr. G.J.W. van Bussel

Readers:

ir. C.J. Simão Ferreira

ir. W. Haans

dr. ir. L.L.M. Veldhuis

Abstract

A lot of research has been carried out in the past on wind turbine wake aerodynamics. Models exist for both the near field ($\leq 2D$ downstream) and the far wake ($\geq 2D$ downstream). The near wake is governed by a typical vortex structure that gradually decays due to viscous and turbulent mixing effects, forming the less structured far wake region. The formation of the far field from the rotor region and near wake is not completely understood yet. In this thesis an attempt is made to develop a simple model that tries to capture the decay of the vortex wake within the first two diameters downstream of the rotor.

A free wake lifting line vortex model has been developed. Viscous effects have been added to the vortex code in the form of vortex core models and a simple model that describes the turbulent decay of circulation as a function of ambient turbulence intensity. Furthermore models for simulating wind shear and the presence of the nacelle have been implemented.

A thorough validation study of the model has been carried out by means of hot-film and Particle Image Velocimetry (PIV) measurements. Close to the rotor the model compares well with the measured induced velocities measured with a hot-film. PIV measurements show that the model captures the position of the tip vortex quite well within the first diameter downstream. The measured velocity field can however not be reproduced correctly by the code. No measurements were available that can validate the turbulent decay of the vortex wake; instead suggestions are made for an experiment in the Open Jet Facility (OJF) of Delft University of Technology.

The new model is only valid in the region of the wake where the vortex structure of the wake is still in tact which is typically between one or two diameters downstream. Further downstream the outputs from the model may be used as an input for a Reynolds Averaged Navier-Stokes (RANS) model that describes the far wake of the rotor.

Acknowledgments

Delft, June 17, 2009

Eleven months of work on my final thesis brings me to the end of my studies in Aerospace Engineering. Although the final thesis is an individual assignment, the support and feedback from many persons has contributed significantly to the end result. Carlos, many thanks for your guidance during the development of the vortex code and stimulating me to produce nice results and pretty pictures. I will remember the relaxed atmosphere of the wind energy chair; thanks to all my fellow students and staff members for the pleasant months on the fifth floor.

Part of this thesis has been written in collaboration with GE Wind Energy in Salzbergen. I would like to thank Henk-Jan Kooijman and the members from the micrositing team for welcoming me at office in Salzbergen for the second time. Also many thanks to Clarissa Belloni, Christian Aalburg and Stefan Kern from GE Global Research for the frequent phone calls and useful criticism on my work.

Finally a word of gratitude to my parents for welcoming me back in Ter Apel and my girlfriend Suzanne for all the nice weekends in Groningen and Delft.

Menno Kloosterman

Table of Contents

Appendices

List of Figures

List of Tables

Nomenclature

Latin symbols

$a_{i,j}$	Influence coefficient	m/s
b	Wing span	m
c_d	Drag coefficient	-
c_l	Lift coefficient	-
c_n	Local chord length	m
k	Wake Decay Constant (WDC)	-
m	Shear exponent power law	-
q	Turbulent kinetic energy	-
r_c	Vortex core radius	m
$\bar{r}$	Nondimensional distance from vortex core center	-
u_*	Friction velocity	m/s
w	Downwash velocity	m/s
z_0	Roughness length	m
A	Wing aspect ratio	-
C_t	Thrust coefficient	-
C_L	Lift coefficient	-
C_D	Drag coefficient	-
D	Rotor diameter	m
I_∞	Ambient turbulence intensity	-
K_v	Viscous parameter Biot-Savart	-
N	Number of blades	-
N_b	Number of radial blade stations	-
N_ϕ	Number of azimuthal steps	-
N_{rev}	Number of revolutions	-

R	Rotor radius	m
R_r	Root radius	m
R_t	Tip radius	m
R_i	Position of radial station along the blade	m
Re_v	Vortex Reynolds number	-
U_∞	Axial free stream velocity	m/s
U_w	Velocity in the wake	m/s
V_θ	Tangential velocity	m/s
$\bar{V}_{blade}$	Total perceived blade velocity vector	m/s
$\bar{V}_{ind}$	Induced velocity vector	m/s
V_{down}	Downwash velocity	m/s
$\bar{X}$	Position vector of wake nodes	m

Greek symbols

α	Angle of attack	rad
α_L	Lamb constant	-
δ	Turbulent dissipation constant	-
δ_r	Cut off radius Biot Savart	-
ϵ	Vortex filament strain	-
ϵ_{R^2}	R^2 norm	-
η	non dimensional turbulent dissipation rate	-
κ	Von Karman constant	-
λ	Tip Speed Ratio (TSR)	-
μ	Dynamic viscosity	kg/ms
ν	Kinematic viscosity	m^2/s
ξ	Vorticity	$1/s$
ρ	Air density	kg/m^3
τ	Shear stress	N/m^2
ϕ	Blade azimuth angle	rad
$\Phi(x, y, z, t)$	Velocity potential	m^2/s
Γ	Vortex strength	m^2/s
Γ_0	Maximum bound vortex strength elliptic wing	m^2/s
Γ_T	Strength of trailing vortex	m^2/s
Γ_S	Strength of shed vortex	m^2/s

Acronyms

AE Aerospace Engineering

AEP Annual Energy Production

BEM Blade Element Method

CFD Computational Fluid Dynamics

DNW Duits Nederlandse Windtunnels

DWW Dutch Wind Workshops

DUT Delft University of Technology

ECN Energy Research Center Netherlands

EWEC European Wind Energy Conference

GE General Electric

HAWT Horizontal Axis Wind Turbine

HWA Hot Wire Anemometry

LES Large Eddy Simulation

LLF Large Low-speed Facility

LSE Least-Squares Estimator

MEXICO Model Experiments In Controlled Conditions

OJF Open Jet Facility

PIV Particle Image Velocimetry

PLA Phase Locked Average

RANS Reynolds Averaged Navier-Stokes

TSR Tip Speed Ratio

VAWT Vertical Axis Wind Turbine

VDC Vortex Decay Constant

WDC Wake Decay Constant

WRA Wind Resource Assessment

EWTS European Wind Turbine Standards II

LIDAR Light Imaging Detection And Ranging

SNR Signal to Noise Ratio

Chapter 1

Introduction

The past two years there has been a significant decrease in activity of the global economy. Banks received support from governments to prevent their collapse and many companies had to let go part of their staff or close the doors entirely. The economic crisis is also affecting industries that are active in wind energy, for example manufacturer Vestas announced that it has to lay off 1900 staff members in 2009. Although the demand for wind energy has not declined tremendously, private investors are suffering to find the financial resources to pay for the initial investment costs that are involved in development and installation of a wind farm.

Despite the current economic situation both the European Parliament and the US Administration have acknowledged the need for more renewable resources and promised a significant increase in investments in both solar and wind. Moreover large steps are taken in the development of electric cars that are either powered by batteries directly or with hydrogen fuel cells. Either way this means that the percentage of electricity in the worlds total energy demand will increase, leading to even more opportunities for the wind energy industry.

Aerodynamically a wind turbine is the inverse of a propeller or helicopter rotor. A wind turbine slows down the oncoming freestream exerting a force in the opposite direction of the flow whereas a propeller speeds up the flow and applies a force in the same direction as the flow. It is therefore not surprising that many faculties in Aerospace Engineering have also become active in wind energy. Knowledge on low speed aerodynamics and light-weight structures are to a large extent applicable to wind turbine design, therefore wind turbines have become much more advanced in the past decades.

The interaction between wind turbines in wind farms is a topic of great importance as wind turbines are often installed in clusters and therefore shedding wakes to neighbouring turbines. However the effects that govern the interaction are still not fully understood and calculated with simple engineering models, giving relatively large uncertainties in wake energy losses and fatigue loads. Typically a wind farm is supposed to operate for at least twenty years; combined with the uncertainties this often leads to quite conservative layouts and designs. Research institutes, universities and industries are therefore continuously trying to understand rotor and wake aerodynamics and improve the designs of turbines by adding for example smart aerodynamic surfaces for loads control. In this way future wind turbines can be optimized aerodynamically and structurally and wind farm layout can be optimized for maximum Annual Energy Production (AEP) against lowest costs.

1-1 Scope of the thesis

This thesis focuses on the aerodynamics of wind turbine wakes, in particular on the near-wake i.e. distances smaller than two diameters downstream of the rotor. The main thesis goal is to increase the understanding of the development of the wake from the rotor region into the far field. An attempt is made to develop a simple model that describes the development and decay of the near wake. The model is validated by means of wind tunnel measurements and its strengths and weaknesses are discussed.

From a wider perspective the thesis goals fit well within the general objective to design optimal and cost-effective wind turbines and wind farms. Compared to the aviation industry, commercial design and operation of wind turbines has a short history. It may therefore be expected that wind turbine design will improve significantly in the next decades making it an interesting and challenging field for engineers.

1-2 Outline of the thesis

The body of the work is divided in six chapters, summarized below:

Chapter 2 gives an overview of the wake modeling methods that are currently available for both the near and far field. A number of recommendations are made for further research and the thesis goals are explained more thoroughly.

Chapter 3 describes different models for estimating both the turbulent and viscous decay of vortices in the atmosphere. Some of these models are implemented in the new wake model introduced in chapters 4 and 6.

Chapter 4 explains the development of a free wake lifting line model for the simulation of the rotor forces and the near wake. The standard lifting line approach is expanded with vortex decay models that allow modeling of the decay of the vortex strengths in the wake as a function of turbulence intensity and wake age.

Chapter 5 presents a validation study of the vortex code by means of wind tunnel measurements. Firstly, the performance of the code is validated in the rotor region with hot-film measurements very close to the rotor. Also the model is validated against Particle Image Velocimetry (PIV) measurements.

Chapter 6 shows the ability of the code to calculate the induced velocity profile at various downstream positions in the wake, up to two diameters downstream. A sensitivity study is performed on the effect of the vortex decay parameters on the velocity profile. Furthermore, a number of attempts to improve the physical validity of the model are presented. Finally a conceptual experimental setup is discussed allowing for a more thorough validation of the model

Chapter 7 summarizes the conclusions to the work performed and some suggestions for further research.

Throughout the thesis it is assumed that the reader has a basic understanding of low speed (rotor) aerodynamics and wind turbines in general.

Chapter 2

Current and future wake models

This chapter provides the reader with an overview of the most common wind turbine wake models. The first sections describe the modeling methods that are available for both near and far wakes. Secondly an outlook is made into future modeling methods. Finally recommendations are given for further wake research and development and implementation of new models in order to increase the reliability of loads and Annual Energy Production (AEP) calculation for wind turbines in wind farms.

2-1 Challenges in wake modeling

2-1-1 Relevance of wake modeling

During the last decades wind turbines and wind farms have significantly increased in size. Space for installation of wind farms is however limited which raises the question on how to position a maximum amount of turbines within a given area. It is therefore very relevant to be able to accurately predict and describe the aerodynamic interaction effects between wind turbines.

Turbines that experience wake conditions are exposed to reduced wind speeds and increased turbulence levels. The deficit in wind speed reduces the power output of the turbines whereas the increased turbulence levels increase the fatigue loads on the blades and other components.

2-1-2 General wake structure

The flow behind a rotating wing is complex and very unsteady in nature. Immediately downstream of the rotor the flow is governed by unsteady effects, mainly caused by tip vortices, the shedding of the vorticity from the boundary layer and the passage of the blade. Furthermore, there is a strong shear layer between the wake flow and the ambient outer flow.

Due to the shear layer the production of turbulence is increased. The wake flow will therefore mix with the outer flow which eventually leads to the decay of the shear layer and results in a Gaussian-like velocity deficit profile. Within this region the presence of the rotor is no longer noticeable and the large-scale vortices have broken down into smaller scales.

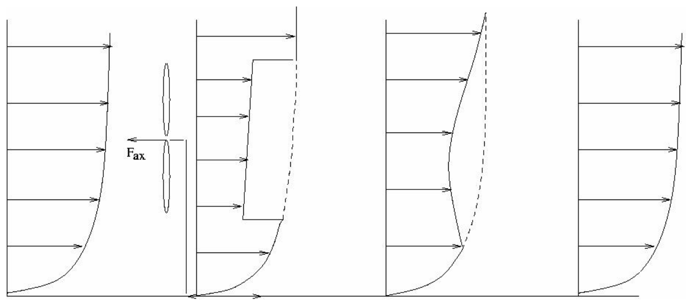

Figure 2-1: Development of the wake downstream of a rotor, *source:* [35]

Though to a lesser extent, the Gaussian velocity deficit profile continues to experience viscous and turbulent dissipation effects and mixing with the ambient outer flow. This induces a continuous expansion of the wake until eventually the wake has completely dissipated. In stable atmospheres the presence of the wake may persist for a long time whereas a more turbulent, unstable atmosphere leads to a much quicker decay of the wake [35].

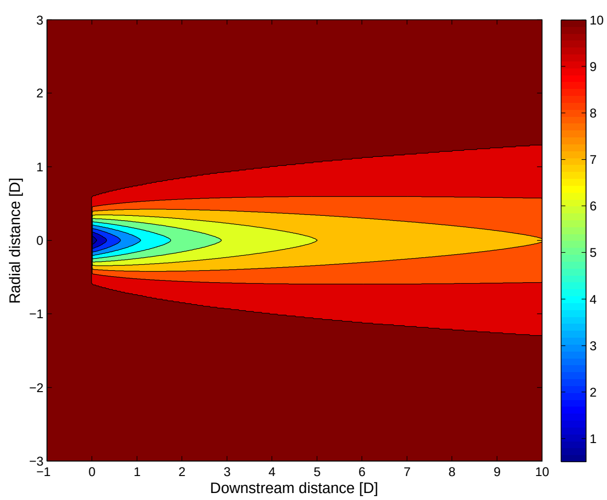

Figure 2-2: Expansion and decay of wind turbine wake, $U_\infty = 10m/s$, colors represent the axial velocity deficit U_w, *source:* [29]

2-1-3 Difficulties in wake modeling

Ideally the flow field in a large wind farm with all wake effects could be calculated by a super computer with a full Navier-Stokes code, which would give a relative accurate prediction of the performance of the wind farm. This is however rather unrealistic since such a simulation would require much computational effort. Therefore simplifications must made to the governing equations that enable relatively quick numerical or analytic solutions to specific flow problems.

Different phenomena drive the wake flow in different areas of the wake. Therefore it is important to use the right modeling assumptions when analyzing certain areas of the wake. For that reason different wake models have been developed focusing on various aspects and stages of wake flow and/or turbine interaction effects.

Despite the numerous wake models that have been developed and experiments conducted the unsteady aerodynamic phenomena in wind farms is still largely not understood [40]. Therefore this field provides interesting topics for research studies aiming at improving efficiency and reliability of wind farms and the design of turbines.

2-2 Near wake models

The 'near wake' is not formally defined. In engineering it is often assumed that downstream distances smaller than two rotor diameters ($\leq 2D$) can be considered as the near wake. Another definition states that the near wake is the area behind the rotor where the properties of the rotor can still be discriminated i.e. number of blades, tip vortices, stalled flow, etc. The latter definition shows that it is important for near wake models that the aerodynamic properties of the blades are modeled correctly whereas for far wake models this is of lesser importance.

2-2-1 Blade Element Methods (BEM)

The Blade Element Method (BEM) method today still is a common way of modeling the lift forces on wind turbine rotors. Its main assumption is that the air flows through annuli that can be modeled independently. Lift and drag forces on the annuli can be calculated by using induction theory and airfoil characteristics. These assumptions make the BEM methods easy and quick to implement in a computer program. Therefore BEM methods have been, and still are the most frequently used design tools in the wind energy industry. The simplicity of the theory is also its main weakness since many higher order effects like unsteady flow and yaw misalignment are not included in the flow. Since wind turbine dimensions have increased rapidly in the past decades these higher order effects may become more important during analysis and design. Listed below are three well-known corrections that can be made to the BEM equations.

- The Prandtl tip correction factor, corrects for the fact that wind turbines only have a finite number of blades. This correction becomes lower as the number of blades increases.

- Glauert's correction recalculates the C_t for heavily loaded turbines by means of an empirical relation.
- The energy loss due to wake rotation can be included, although discussion is still going on whether this effect should be included or not.

These simple correction methods are sufficient to accurately calculate the lift forces and near wake profile for uniform steady conditions. However the ambient freestream experienced by wind turbines is typically unsteady in both velocity and direction; hence the blade forces and the wake are unsteady as well. Furthermore 3D effects that cause stall delay on the outward part of the blade play a predominant role as well. The assumption of the BEM theory that the turbine experiences uniform steady flow is therefore not valid.

Recent research has been carried out into the modification of the BEM codes by T. Sant [32]. Sant improved the BEM codes by adding 3D airfoil information and including yaw errors and unsteady effects. By means of a thorough analysis of induced velocities in yaw with a free wake vortex model Sant derived simple engineering equations that correct the induction factors in BEM for yaw effects.

Currently H. Snel from Energy Research Center Netherlands (ECN) is improving BEM by trying to include wind shear in the simulations. Preliminary results have been presented during the 2008 Dutch Wind Workshops (DWW) in Delft. The relevance of this research is especially high for large turbines since there will be a significant difference in wind speed between upper- and lower tip height.

Despite their limitations BEM models are still frequently used for the analysis and design of wind turbines in industry. Therefore research in improving BEM is relevant and will be continued in the upcoming years.

2-2-2 Generalized actuator disk models

The classical BEM method is limited to steady uniform flow which is not representative for the operating conditions of most wind turbines. Generalized actuator disk models have a lot less limitations since the flow around the turbine is solved by means of Computational Fluid Dynamics (CFD) methods. The flow around the blades is however not resolved numerically but the lift and drag forces are derived from sector-wise characteristics of the airfoils and are corrected for 3D effects [40]. It must be noted that 3D lift characteristics depend on rotational effects which must be considered for implementation in a BEM simulation tool. Furthermore gusts of wind may cause dynamic stall which is currently not accounted for.

These methods prove to be quite suitable to study various operating conditions and wake dynamics. Validation studies performed by Sørensen in [36] show promising results. Full CFD calculations of the surrounding flow will however be quite time consuming and therefore less applicable for large wind farms.

2-2-3 Vortex models

In potential flow solutions vortices are used to represent lift on a wing or other lifting surfaces. The main assumption of a potential flow vortex is that all vorticity is concentrated in the core of the vortex (see. [19]). Especially in low speed aerodynamics where compressibility does not play a significant role vortex methods are frequently used. This entails that vortex methods lose accuracy as the Reynolds number decreases and viscosity becomes more important. As with any potential flow the solution of the system must satisfy Laplace's equation which represents the Navier-Stokes equations for incompressible and inviscid flow. Numerical vortex methods are always based on solving a special case of Laplace's equation on every grid point of the geometry.

$$\nabla \cdot \nabla \Phi(x, y, z, t) = 0 \tag{2-1}$$

Panel methods

The geometry of an airfoil (2D) or a wing (3D) can be discretized with small panels; each panel has a constant vortex strength. Based on the geometry and the inflow properties the strength of each panel can be determined by applying a non-entry boundary condition at the center point of each panel. A detailed description of 2D panel methods can be found in reference [21]. A popular code based on implementation of panel methods is XFOIL, a numerical airfoil design tool that can quickly assess the main properties of a given airfoil.

For wind turbine applications 3D panel codes can be implemented that can be used to evaluate pressures and loads on the blades and the velocities in the near field. Kristian Dixon describes the development of a Free-Wake panel method for the simulation of Vertical Axis Wind Turbine (VAWT) in reference [3].

With panel methods a detailed information can be acquired on the velocity distribution at the blade in both span- and chord wise direction. This enables a detailed evaluation of the pressures and loads on the blades and a possible coupling with an elastic model.

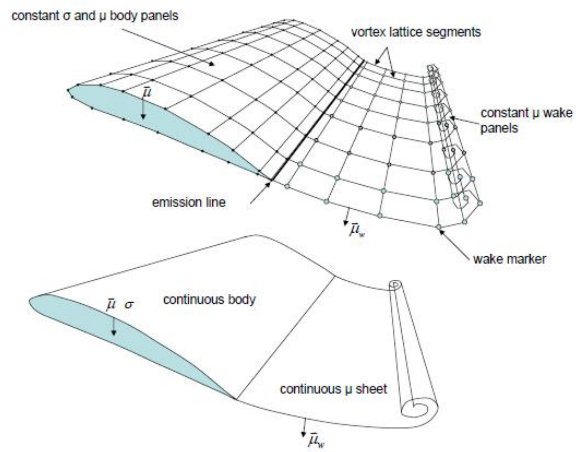

Figure 2-3: Three dimensional discretization of wing and wake, *source:[3]*

Lifting line solutions

Instead of modeling the blade with a finite amount of panels, the blade can also be modeled as a single lifting line with a bound vortex as suggested by Prandtl in 1909 (see: [19]). This method gives a lower level of detail of the velocities at the blade and is more suitable for evaluation of velocities in the near wake. In chapter 4 the principles of lifting line solutions for wind turbines are described in more detail.

Performance of vortex models

For calculation of the steady blade forces most vortex methods perform on par with the classical BEM methods. However the main advantage of the vortex methods is their ability to easily cope with unsteady and yawed flows, i.e. operating conditions that frequently occur for wind turbines. Furthermore, vortex methods are able to calculate the near vortex wake in the vicinity of the rotor.

Performing unsteady calculations is however time consuming and some methods experience stability problems. Other sources of error can derive from the implementation of 3D airfoil data and the effect of dynamic stall on turbine performance (see [41]). For far-wake calculations the methods are less suitable due to their inviscid nature.

2-2-4 Navier-Stokes codes

Solving the full Navier-Stokes equations for the domain around a wind turbine rotor could give an accurate prediction of the flow phenomena that occur at the rotor blades and the near wake. However, the computer power demands to perform a full viscous and turbulent simulation are so high that it is necessary to simplify the Navier-Stokes equations. This is however a difficult job since too much simplification will reduce the accuracy of the solution of the unsteady flow that occurs the vicinity of the rotor.

Reynolds Averaged Navier-Stokes (RANS)

A way to go around the need for solving the fully turbulent Navier-Stokes equations is by assuming that a turbulent flow consists of a mean flow and a fluctuating part (see [22]).

$$u_i = \bar{u}_i + u_i' \tag{2-2}$$

Substituting equation 2-2 in the momentum and continuity equations and taking the time average gives the Reynolds Averaged Navier-Stokes (RANS) equations. These equations are quite similar to the original expressions, with the main difference being an additional term in the momentum equation, the so-called Reynolds stress, which is typically the average of the product of two fluctuating velocity components. This term can be interpreted as an additional turbulent viscosity, which becomes part of the viscous stress tensor.

$$\tau_{turb} = -\rho_0 u_i \bar{u}_j \tag{2-3}$$

The Reynolds stress tensor includes additional unknowns in the RANS equations hence additional relations are required to get a closed system of equations. The only way to get a closed system of RANS equations is by assuming other types of relations between the Reynolds stresses and the average flow field. These relations are from here on referred to as turbulence models. Well known solutions are the $k-\epsilon$ methods, where ϵ represents the viscous dissipation of turbulent kinetic energy k. Crespo describes the usage of $k-\epsilon$ methods for wind turbine applications in reference [6].Turbulence models are however quite empirical and often used to tune the calculations to fit experimental data. The effect of turbulence is more explicitly modeled by means of a Large Eddy Simulation (LES).

Large Eddy Simulations (LES)

Wind turbines operate at large Reynolds numbers in the order of $1 \cdot 10^6$, hence here is a significant difference between the smallest and largest length scales of the vortices or eddies in the flow. It is therefore not possible to perform a full Navier-Stokes simulation since the required grid size will be too time consuming for any computer to solve. A Large Eddy Simulation only takes into account the eddies in the flow that are larger than the grid size. In this way the large scale turbulent motions that govern diffusion, momentum and energy exchange are calculated explicitly and only the dissipative small scale motions have to be modeled with a turbulence model. Interesting features of the flow like turbulence intensity, axial momentum loss, flow separation and spatial coherence of turbulence can be modeled with an LES.

Jimenez compared the results of LES for wind speed deficit and added turbulence intensity with field measurements for both near and far wake (see [17]). In his results he also added calculations of the Frandsen turbulence model. However due to lack of measurement data it is not clearly visible which turbulence model performs better. Nevertheless simplified LES is interesting for wind farm calculations since it enables a direct calculation of wind speed deficit and added turbulence intensity.

2-3 Far wake models

In rotor aerodynamics downstream distances larger than $2D$ from the rotor plane are generally considered as the far wake. At these distances the wake has fully developed and the shear layer between the wake and outer flow is no longer present (see figure 2-1). Also the aerodynamic properties of the rotor are not noticeable anymore which makes modeling the far wake somewhat simpler than the near wake. In engineering models that are used for wind farm energy predictions there is often a clear distinction between near and far wake models, whereas in reality the regions are evidently related. Furthermore kinematic far wake models separate the effects of wind speed deficit and wake added turbulence intensity while in reality these phenomena are connected.

2-3-1 Kinematic models

Kinematic models are relatively simple wake models that can be solved analytically, hence their computational effort is very low making them suitable for the evaluation of wind speed deficits in large wind farms. Due to their simplicity the models are not able to describe the increase in turbulence intensity that occurs in the wake and therefore have to be coupled with a separate turbulence model. Three well known kinematic models are the solutions by N.O. Jensen, G.C. Larsen and S. Frandsen.

Jensen model

One of the oldest and most commonly used wake models is the model by N.O. Jensen [16]. It is quite a simple wake model, assuming a linearly expanding wake with a velocity deficit that is only dependent on the distance behind the rotor.

$$D_w = D(1 + 2ks) \tag{2-4}$$

$$U_w = U_\infty \left[1 - \frac{1 - \sqrt{1 - C_T}}{(1 + 2ks)^2}\right] \tag{2-5}$$

Where k represents the Wake Decay Constant (WDC) and s the downstream distance expressed in rotor diameters. The velocity in the wake only depends on the downstream distance and not on the radial position in the wake. This results in a so-called hat shaped velocity profile with a uniform velocity within the wake. In reality however the velocity profile varies across the plane of the rotor.

Larsen model

The model by G.C. Larsen (referred to as the Larsen model from now, but also known as the EWTSII model) is based on the Prandtl turbulent boundary layer equations and has closed-form solutions for the width of the wake and the mean velocity profile in the wake. Compared to the Jensen model this model captures the Gaussian shape of the wind speed deficit profile in the wake and also depends on the ambient turbulence intensity. This semi-analytical model enables a quick assessment of the velocity-deficit as a function of downstream and radial position. Details of the model can be found in [23].

Frandsen model

More recently S. Frandsen presented his Storkpark analytical wake model for offshore wind farms at the European Wind Energy Conference (EWEC) 2006 [9]. This model is similar to the Jensen model as it also assumes a hat-shaped wind speed deficit profile. The interaction of neighboring turbines and addition of multiple wakes is however modeled more carefully.

- The wake expansion is limited to upward expansion only as soon as neighboring wakes intersect.
- In multiple wakes, addition of wind speed deficits converges to a minimum wake flow speed.
- Information on the internal earth boundary layer is necessary to model the flow regime in between turbines correctly.

No thorough validation studies of this model are currently available.

2-3-2 Field models

Field models are more advanced than kinematic models and solve the RANS equations in order to obtain the flow field in the entire wind farm. Solving the equations requires more time since numerical techniques have to be applied.

Ainslie model

A well known field model is the model by Ainslie, which assumes two dimensional, axi-symmetric flow and hence solves the 2D turbulent momentum equation with a $k - \epsilon$ method for closure. The model is not able to calculate the flow in the near wake, due to neglecting the stream wise pressure gradient in the flow. Therefore the model has to be initialized, Ainslie assumes a Gaussian wind speed deficit profile as initialization.

UPMWAKE

The theory behind the UPMWAKE code are the 3D parabolized RANS equations as developed by Crespo with a $k - \epsilon$ model for closure [6]. ECN implemented this code in the Wakefarm program, again the near wake is initialized assuming a Gaussian wind speed deficit profile [34]. The evaluation of the code in a cluster of wind turbines is relatively fast due to the parabolic equations (only upstream effects are modeled).

UPMWAKE is able to incorporate 3D effects like the downward deflection of the wake centerline and wake meandering. To capture the wake meandering effect an accurate wind rose is however required as an input. Incorporation of wake meandering in this case means that several steady calculations are performed for different wind directions of which the average is taken. Validation studies for both wind speed deficit and turbulence intensity show good results but the simulation results are very sensitive to input parameters and high quality measurements are required for proper comparison with simulations [34].

Elliptic field models

Though elliptic field models are able to capture many phenomena in the (near) wake in great detail they are very computationally intensive. In [25] and [38], simulations are performed for only one and three turbines respectively. The Robert Gordon University (RGU) used a fully elliptic three-dimensional Navier Stokes code with a turbulent $k-\epsilon$ closure during the ENDOW project. It required about 12 hours of calculation time in 2001 [34] compared to seconds or minutes for the other models, while not yielding significant better results. Usage of these models is at the moment not feasible for energy and load calculations of large wind farms.

2-4 Combined models

A way of working around the limitations of different wake models is to use different models in the region of the wake where they are most applicable. In this way models can be combined in a clever way such that the entire flow field from rotor to far field is resolved.

2-4-1 Hybrid model by Voutsinas

An elegant solution is presented by Voutsinas et al. in references [43] and [42]. The computational domain is divided into three regions in which different models are used for resolving the flow field.

1. The rotor is modeled by means of a potential flow lifting line code. An iterative scheme is applied to resolve the bound vortex strength. The solution is used to generate a flow field in a plane $0.05D$ downstream of the rotor.
2. The output from the vortex model is used as an input for a viscous RANS code with a $k-\epsilon$ model for closure. This model calculates the flow field up to $3-4D$ downstream of the rotor
3. The output of the viscous flow solves is used as a boundary condition for the integration of the boundary layer equations to calculate the velocity deficit profile at distances larger than $4D$ downstream. In this case, a self similar velocity profile is assumed.

The results of the calculations are compared with single wake measurements taken from NIBE turbines at $2.5D$, $4D$ and $7.5D$ downstream of the rotor. More validation studies may be necessary to clearly state whether this method performs better or worse than simpler far wake models. Voutsinas et al. clearly showed that it is possible to combine various wake models and derive an elegant simulation of the entire flow field downstream of a wind turbine.

Another interesting finding from this work is that the decay of vorticity in the flow is concentrated in the near field ($< 2D$). Strong tip vortices that are shed into the wake lose their strength quite quickly in the turbulent environment and are broken down into smaller scales.

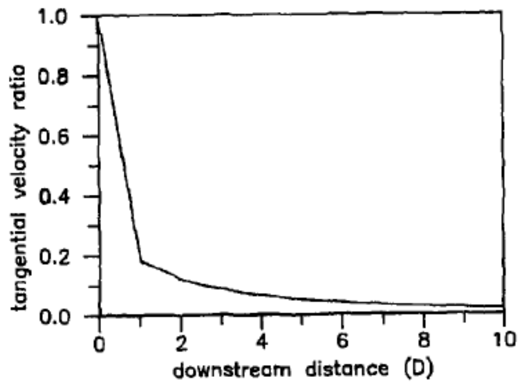

Figure 2-4: Swirl decay as a function of downstream distance, *source: [43]*

2-4-2 Hybrid model by Kasmi

Another effort to more connect the near and far fields has been carried out by A. El Kasmi and C. Masson in reference [20]. Their method models the rotor using a classical BEM approach. Alternatively the rotor can be modeled with standard induction theory, assuming a uniformly loaded rotor. Additionally the influence of the nacelle is taken into account on the induced velocities just downstream of the rotor. The wake is then extended from the near field into the far wake by means of a RANS simulation. Furthermore an additional term describing the energy transfer between large scale and small scale turbulence has been included in the RANS equations which gives a better description of production and dissipation of turbulent kinetic energy.

Comparison of the simulation results with single wake measurements taken at various wind speeds and ambient turbulence levels showed that the new model performs significantly better than the $k - \epsilon$ model developed by Crespo et al in 1985. Also the decay of axial turbulence intensity with downstream distance is modeled with more accuracy.

Future work with this model is focused on generalizing the turbulence models such that they are applicable for more complex terrains.

2-5 Future research

A broad range of research studies has been carried out on the topic of understanding the flow field behind a single or several wind turbines. Full CFD applications are still too time consuming and therefore compromises have to be made between computational time and simulation accuracy. New generation quantum computers may be able to solve the Navier-Stokes equations much more quickly, nevertheless it may take up to two decades before full CFD becomes feasible for wind farm applications [5].

Engineering expressions will remain important especially for industrial applications where computational time must stay as low as possible. Therefore it is important to continue to search for elegant methods that have a high accuracy to cost ratio. For example one of the conclusions of the DWW 2008 was that BEM will continue to be used in industry which shows that research into expanding these methods to deal with unsteady $3D$ flow is very relevant.

The connection between different wake regions by applying different models seems a promising path. The computational effort remains within limits since each model is optimized for the domain of computation to which it is applied. A promising area of research would be to expand hybrid models with an upstream model that correctly simulates the inflow conditions. According to Vermeerr the correct modelling of the inflow is still a great challenge [40].

This chapter shows that most models either simulate the near or the far wake regions. In reality the two regions are not seperated but there will be a gradual transition. Voutsinas shows that the near wake region is governed by vortex decay by means of a RANS simulation in [43]. Perhaps some models are available that can simulate the decay of a vortex as a function of its age and atmospheric conditions. These models can then be implemented in a near wake model possibly extending the near wake model to give reasonable predictions at one or two diameters downstream. The next chapter gives an overview of the different vortex decay models that are currently available and the physical phenomena that drive vortex flow.

Chapter 3

Vortex decay models

In chapter 2 it is identified that the decay of the vortex wake is a predominant process within the first two diameters downstream of the rotor. This chapter describes two important mechanisms that govern the decay of trailing vortices downstream of a wing or a rotor. One can imagine that a vortex has a finite lifetime when it is shed into the atmosphere. Atmospheric mixing effects and vortex core growth will lead to a reduction in strength and the eventual demise of the vortex. In this chapter models are presented that describe both the viscous and turbulent decay of vortices. Some of these models are implemented in the vortex model that is described in chapter 4.

3-1 Formation of vortices in the atmosphere

Before diving into the models and equations of vortex flow it is desirable to establish a more general overview on the driving factors behind the formation of vortices in the atmosphere. Well known examples of vortices are trailing tip vortices behind aircraft and tropical cyclones. Although these two vortices seem completely different phenomena it turns out that their formation can (partially) be explained by the presence of local strong pressure differences. The next three paragraphs will give a short outline of the formation of different types of vortices, their differences and similarities.

3-1-1 Tip vortices from lifting surfaces

The formation of tip vortices behind aircraft or in general behind any lifting surface with finite dimensions is inherently related to the presence of a lift force. The lift on a wing is generated by an airfoil that causes a low pressure area on the upper surface and a high pressure area on the lower surface of the wing (see Figure 3-1). Naturally air flows from high pressure regions to regions with low pressure, hence near the tips of the wing a swirling motion forms from the lower to the upper surface. The pressure difference between the upper and lower surface of the wing is therefore the driving factor for the formation of the tip vortex. Note that in steady conditions the pressure difference near the trailing edge of the airfoil is zero which is also known as the Kutta-condition.

The strength of the tip vortex can be influenced by the for example the aspect ratio of the wing or the local chord length near the wing tip. Modern commercial jet aircraft are often equipped with winglets that reduce the pressure gradient near the wing tip and the strength of the tip vortex increasing the aerodynamic efficiency of the wing.

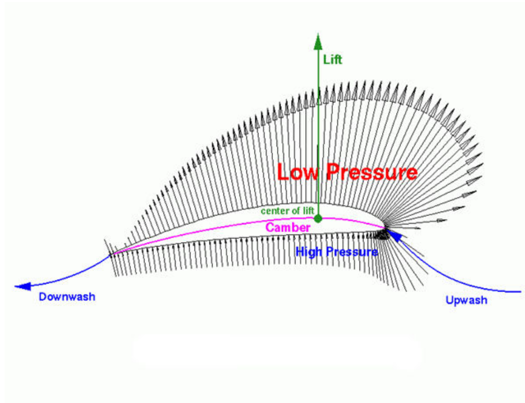

Figure 3-1: Visualization of high and low pressure areas on an airfoil

3-1-2 Vortex shedding

Vortex shedding is an instationary flow where vortices are (periodically) shed from typically a bluff budy that experiences a steady free stream. In fluid dynamics, the flow around a cylinder is often used as an example. The oncoming flow is not able to follow the contours of the cylinder and separates, giving a high pressure region in front of the cylinder and a low pressure region behind the cylinder. This pressure difference causes an alternating shedding of vortices into the flow downstream. When a single vortex is shed, an asymmetrical flow pattern forms around the body and changes the pressure distribution which may induce a periodical shedding of vortices. The periodic wake that is created is often referred to as a Von Karman vortex sheet(see Figure 3-2).

Lifting surfaces experiencing sudden changes in lift will also shed vortices in the wake which can again be explained by the fact that there is a sudden change in pressure distribution such that temporarily a pressure difference occurs near the trailing edge of the wing causing the formation of a shed vortex.

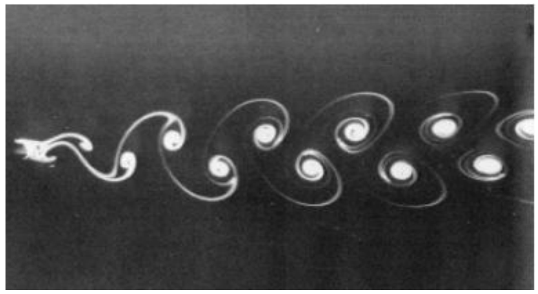

Figure 3-2: Von Karman vortex sheet behind a cylinder in uniform flow at $Re = 300$, *source: [7]*

3-1-3 Cyclones

Cyclones are not caused by the flow around a lifting surface or bluff body and seem to have a completely different origin. Although the exact trigger is not exactly known, reference [30] indicates that the presence of tropical depressions with very low atmospheric pressure over warm water is one of the main sources causing the formation of cyclones. Again a difference in pressure is a key driver in the formation of this type of vortex.

Figure 3-3: Sattelite image of a tropical cyclone

3-2 Vortex modeling

The basic formation mechanisms of vortices have been discussed in the previous section. This section discusses some of the mathematical models that are available to quantify their behaviour.

3-2-1 Potential flow vortex

The simplest model of a vortex that is a solution of the inviscid incompressible Navier-Stokes equations is the potential solution that assumes concentric streamlines around a given point. The velocity along the streamlines is constant however varies with radial distance from the vortex core.

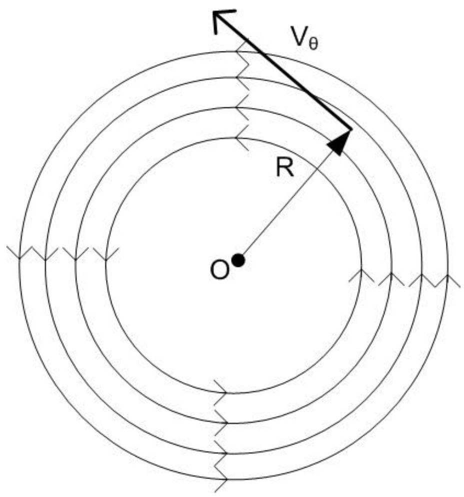

Figure 3-4: Representation of a potential flow vortex with associated tangential velocity $V_\theta(r)$

From the definition of a vortex, the following equations can be derived for the radial and tangential velocity components.

$$V_\theta = \frac{const}{r} = \frac{C}{r} \tag{3-1}$$

$$V_r = 0 \tag{3-2}$$

The constant C can be evaluated by calculating the total circulation of a vortex around a given circular streamline.

$$\Gamma = -\oint_C \mathbf{V} \cdot \mathbf{ds} = -V_\theta 2\pi r \tag{3-3}$$

or

$$V_\theta = -\frac{\Gamma}{2\pi r} \tag{3-4}$$

From the previous equation it becomes clear that the induced velocity becomes unbounded as $r \to 0$. Furthermore all vorticity is contained in the core of the vortex and becomes unbounded as well as r approaches zero. The latter can be proved if the following integral is evaluated, which relates circulation to vorticity.

$$\Gamma = -\int\int_S (\nabla \times \mathbf{V}) \cdot \mathbf{dS} \tag{3-5}$$

$$2\pi C = -\int\int_S (\nabla \times \mathbf{V}) \cdot \mathbf{dS} \tag{3-6}$$

Close to the origin the circle around the origin will be infinitesimally small but the circulation will still remain $\Gamma = -2\pi C$, hence solving for the vorticity and letting $dS \to 0$ the vorticity becomes infinitely large.

In a real physical vortex these singularities cannot exist of course. More realistic models are in that case required that solve for the viscous behavior of the vortex core.

3-2-2 Viscous vortex models

The potential flow solution of a vortex gives an infinitely high swirl velocity in the origin of the vortex while in reality this velocity should typically be zero. Viscous vortex models try to describe the behavior of the region around the vortex origin by modeling the vortex as a two layered system with a finite core size (r_c) and a surrounding outside flow.

Rankine vortex

The simplest model of a vortex with a finite core is the Rankine vortex where the swirl velocity is given by.

$$V_\theta(\bar{r}) = \begin{cases} \left(\frac{\Gamma}{2\pi r_c}\right)\bar{r}, & 0 \le \bar{r} \le 1 \\ \left(\frac{\Gamma}{2\pi r_c}\right)\frac{1}{\bar{r}}, & \bar{r} > 1 \end{cases} \tag{3-7}$$

The core is in this case modeled as a solid body rotation, hence the swirl velocity increases linearly with the radius. The flow outside the vortex core behaves similarly as a potential vortex. However the assumption of solid body rotation in the core area of the vortex is not entirely valid and therefore produces unrealistically high swirl velocities and circulation (see [24]).

Lamb-Oseen vortex

An alternative representation of a two dimensional axisymmetric vortex is given by Lamb and Oseen [24]. The incompressible momentum equation for axisymmetric laminar vortex flow in polar coordinates is given by.

$$\rho\frac{DV_\theta}{Dt} = \frac{\partial}{\partial r}\left[\mu\frac{\partial V_\theta}{\partial r} - \mu\frac{V_\theta}{r}\right] + \frac{2\mu}{r}\left[\frac{\partial V_\theta}{\partial r} - \frac{V_\theta}{r}\right] \tag{3-8}$$

For the swirl velocity the following expression is an exact solution of equation 3-8.

$$V_\theta(\bar{r}) = \frac{\Gamma}{2\pi r_c \bar{r}} \left(1 - e^{-\alpha_L \bar{r}^2}\right), \alpha_L = 1.25643 \tag{3-9}$$

The assumption by Lamb that the flow is entirely laminar is only valid for small vortex Reynolds numbers. High Reynolds numbers vortices are prone to transition to turbulent flow via a transition layer as depicted in Figure 3-5.

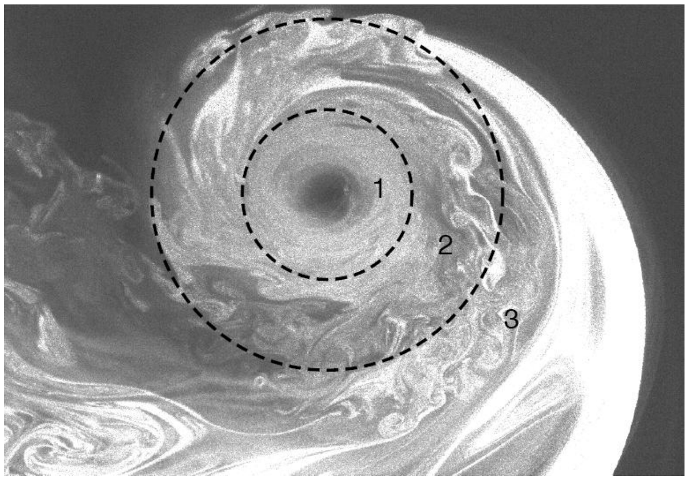

Figure 3-5: Visualization of tip vortex showing three regions (1) Laminar region (2) Transitional region (3) turbulent region, *source: [26]*

Ramasay and Leishman solution

This complex behavior of a vortex is described by Leishman and Ramasamy in references [27] and [28]. The eddy viscosity is modeled by applying Prandtl mixing length theory and introduced a similarity parameter η which eventually leads to a differential equation that relates the circulation γ to η. By means of a Runge-Kutta integration scheme numerical solutions are obtained for various vortex Reynolds numbers (Re_v).

$$Re_v = \frac{\Gamma}{\nu} \tag{3-10}$$

Furthermore an analytic approximation is presented in the work such that users of the model can get a reasonable result in a short time frame. For the swirl velocity the following expression holds:

$$V_\theta = \frac{\Gamma}{2\pi r} \left[1 - \Sigma_{n=1}^{3} a_n e^{-b_n \bar{r}^2}\right] \tag{3-11}$$

Where a_n and b_n are curve-fitting constants that depend on the vortex Reynolds number. Leishman and Ramasamy present values for these constants in their work.

Note that for full scale multi-megawatt wind turbines the tip vortex Reynolds numbers that occur are of the order of $1 \cdot 10^6$ which is at the high end of the transitional regime. However in this case a fully turbulent vortex model may have more validity.

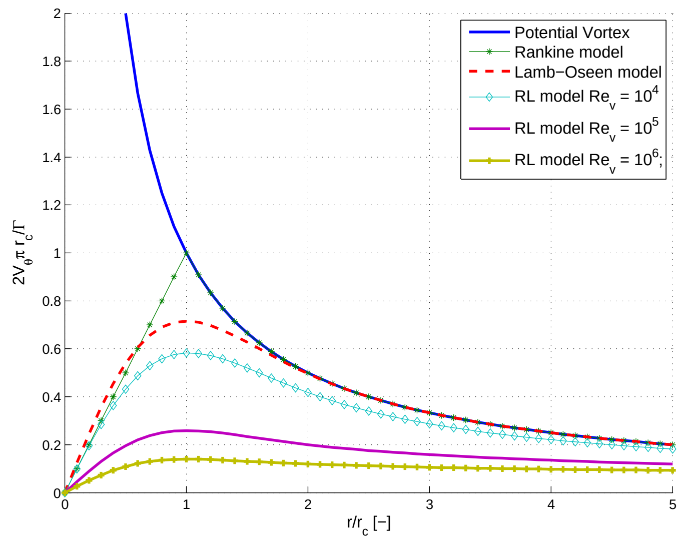

Figure 3-6: Comparison of tangential velocity distributions with distance from the vortex core for different vortex core models

3-3 Decay of vortices in the atmosphere

Two decay mechanisms of vortices in the atmosphere are identified in this section. Inside a vortex viscous forces counteract the swirling motion of the vortex causing a decay in tangential velocity and a growth of the vortex core. Two models are presented that describe the viscous decay of the vortex as a function of time.

On the other hand one can imagine that the decay of a vortex may also be influenced by external factors such as ambient turbulence, shear, temperature difference etc. For wind energy applications no significant research has been carried out in this area. However for aviation applications this topic is very relevant as aircraft trailing vortices limit the capacity of runways. Results of various studies on the influence of external factors and in particular ambient turbulence are presented in this section as well.

3-3-1 Core growth models

Due to viscous diffusion of the vorticity the core of any vortex will grow with its lifetime. As a consequence of this core grow the induced velocities will reduce and the velocity profile will flatten as shown in figure 3-7. Several models are available that attempt to capture this phenomenon.

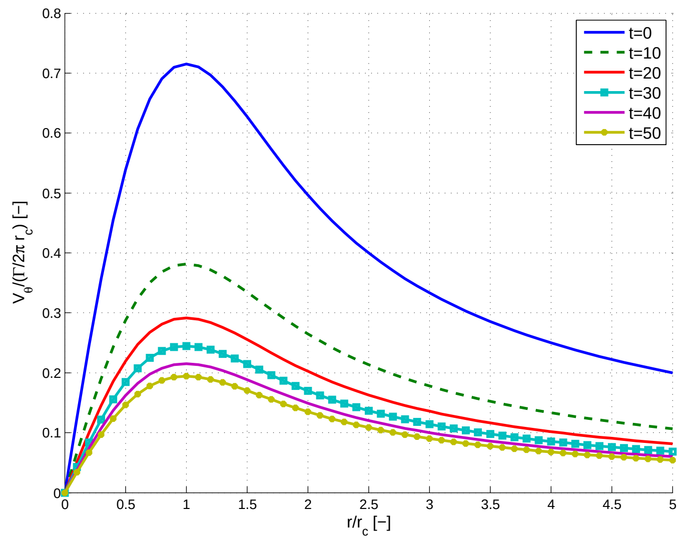

Figure 3-7: Decay of induced velocities as a function of time for the LO-model: $\delta = 50$

Lamb-Oseen model

The laminar vortex model model from Lamb and Oseen gives a very simple expression for core growth due to viscous (molecular) diffusion inside the vortex.

$$r_c(t) = \sqrt{4\alpha\nu t} \tag{3-12}$$

In reality viscous diffusion is however not the only cause of core growth. Depending on the Reynolds number vortices generate turbulence which leads to a much quicker turbulent dissipation of vorticity. Furthermore any turbulence that is present in the boundary layer may contribute to this phenomenon as well. Therefore Bhwagwat and Leishman added a turbulent parameter δ that represents the extra turbulent dissipation.

$$r_c(t) = \sqrt{4\alpha\nu\delta t} \tag{3-13}$$

Typically the value of δ lies between $10 - 100$ depending on the turbine type that is considered. In [32] Sant describes a sensitivity study where he examines the effect of changes in the viscous parameters on the induced velocities and core size. Furthermore the models are compared with measurements of induced velocities on the rotor blades. Luckily the induced velocities turn out to be quite insensitive to changes in δ except for the root and tip area.

Squire [37] assumed a fully turbulent vortex and defined a simple relation between δ and the vortex Reynolds number. For high Reynolds number applications this model may be applicable.

$$\delta = 1 + a_1 Re_v \tag{3-14}$$

Where a_1 is an empirical constant that depends on the assumptions made on the distribution of eddy-viscosity across the vortex. Squire assumed this to be uniform.

Ramasamy and Leishman model

For Reynolds numbers in the transitional range $(1000 - 1e6)$ Ramasamy and Leishman [28] and [27] proposed a core growth models that explicitly models the transition from laminar to turbulent flow in the vortex.(See Figure 3-5)

$$r_c = \sqrt{r_0^2 + 4\alpha\nu(1 + a_1 Re_v)t} \tag{3-15}$$

The following figure shows that the laminar LO model gives a very gradual growth of the vortex core whereas the turbulent LO model and the RL give a much more rapid growth of the vortex core.

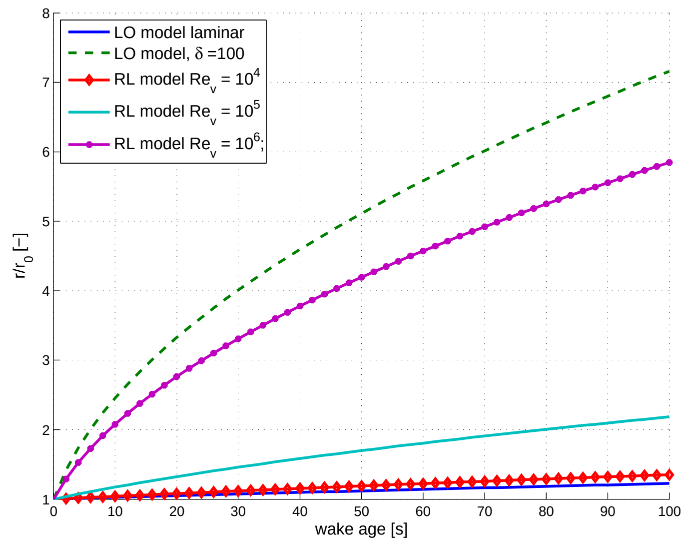

Figure 3-8: Comparison of different core growth models with wake age

3-3-2 Effect of ambient turbulence on vortex decay

Many studies have shown that the strength of a vortex is strongly influenced by the environmental turbulence intensity. Since wind turbines typically operate in an atmosphere with turbulence intensities varying between $10 - 20\%$ it becomes very relevant to be able to capture the effect of vortex decay downstream of the rotor. In this way one might get a good indication of the wake conditions at larger downstream distances from the turbine.

Since the turbulent decay of a vortex is a complex phenomenon many studies are based on numerical simulation of the vortex and its surrounding turbulent flow. For example Holzäpfel ([14] and [13]) has carried out research and provided useful insight on the turbulent decay of single vortices and vortex pairs in various atmospheric conditions. The following figure shows some of his simulation results where the decay in cirulation strength (Γ) is plotted against non-dimensional time (t^*). It is obvious that strong ambient turbulence intensities (25%) lead to a much faster decay than low intensities

(5.5%) for both single vortices (SV) and vortex pairs (VP). Furthermore the effect of atmospheric stratification and the presence of shear in the flow are examined.

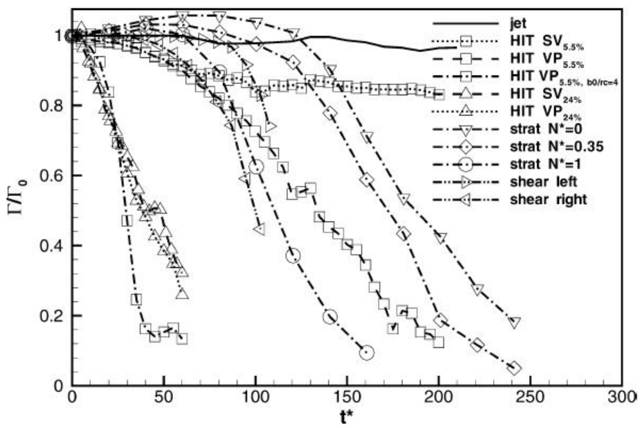

Figure 3-9: Effect of turbulence intensity, shear and stratification on the deay in circulation of a single vortex (SV) or a vortex pair (VP) as a function of time, *source: [14]*

The results obtained by Holzäpfel are obtained by means of Large Eddy Simulations Large Eddy Simulation (LES). This way of simulating is very convenient for modeling complex vortex behavior, but the calculations are very time consuming and therefore not suitable for implementation in a vortex code. Furthermore the level of detail that is obtained by performing an LES is not required in this case.

A much simpler model for tip vortex decay has been presented by Greene in 1986 [10]. His analysis assumes a trailing vortex pair that descents through the atmosphere as typically occurs when an aircraft approaches the airport. For Wind turbine applications this is less relevant, since the turbines are stationary. Nevertheless, in his analysis Greene shows that the turbulent decay of a vortex pair may be modeled as follows:

$$\frac{d\Gamma}{dt} = -0.82\frac{q\Gamma}{b} \tag{3-16}$$

Where q is the turbulent kinetic energy, and b the wing span or initial separation distance between the vortices. This equation shows that turbulent vortex decay may be modeled as an asymptotic process, a result supported by Han in [12]. Han performs an LES for vortices in various environmental conditions but he uses the results of the simulations to come up with two very simple models for the temporal change in vortex strength as a function of turbulence intensity and radial distance from the vortex core. For weak and moderate turbulence the circulation follows a Gaussian function.

$$\frac{d\Gamma}{dT} = -2c_2\frac{\eta^2 T}{R^2}\Gamma \tag{3-17}$$

$$\Gamma = \Gamma_0 e^{-\frac{c_2\eta^2}{R^2}T^2} \tag{3-18}$$

Where T is a non dimensional time, η is the non dimensional turbulent dissipation rate and R the radial distance from the vortex center. For strong turbulence the circulation follows an asymptotic function.

$$\frac{d\Gamma}{dT} = -c_1 \frac{\eta}{R^2}\Gamma \tag{3-19}$$

$$\Gamma = \Gamma_0 e^{\frac{-c_1\eta}{R^2}T} \tag{3-20}$$

Where c_1 and c_2 are empirical constants that are used to tune the model to match the LES simulations. The following two figures show the dependency of the vortex decay on turbulence intensity and radial distance from the vortex core.

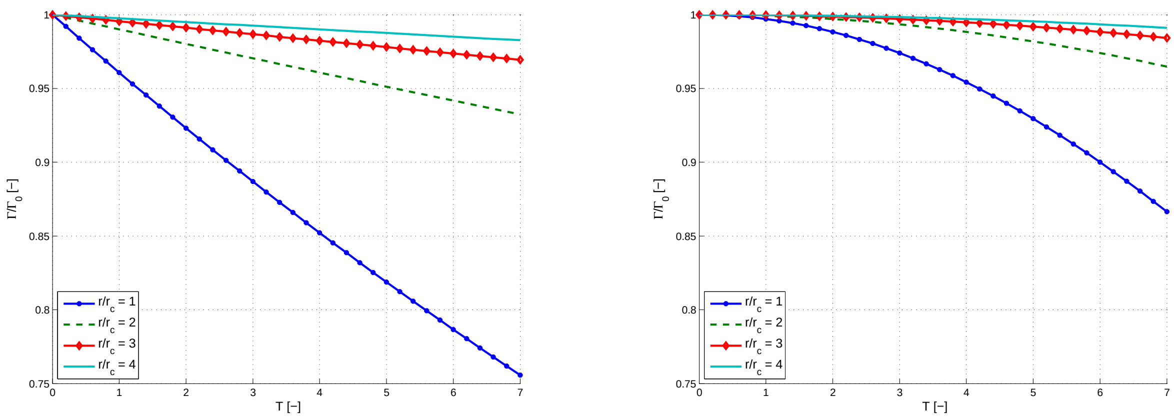

Figure 3-10: Effect of Turbulence intensity and radial distance from vortex core on vortex decay according to the models in equations 3-17 and 3-19, left: $\eta = 0.5$, right: $\eta = 0.15$

3-4 Next steps

This chapter has provided an overview of the different (simple) vortex decay models that are currently available that describe both the turbulent and viscous decay. The main goal of this thesis is to try to develop a new wake model that captures both the formation and decay of the vortex wake downstream of a wind turbine within the first one to two rotor diameters.

To be able to describe the vortex wake behind a wind turbine it is necessary to develop a numerical model that simulates wind turbines with different geometrical and aerodynamic properties. A full $3D$ Computational Fluid Dynamics (CFD) solver will be able to solve the complete turbulent flow and vortex structure around the wind turbine. Such CFD methods are however complex and time consuming and may not always give more physical insight in the governing parameters that drive the dynamics and decay of the vortex wake.

Instead it is desirable to try to use the simple vortex decay models as described in this chapter on a near wake model from chapter 2. It is chosen to use a free wake lifting line code as a baseline model for the near wake. Viscous effects are added to the code by implementing a vortex core model and a turbulent decay model as presented in sections 3-2-2 and 3-3-2. The next chapter describes the development of a free wake lifting line code and the implementation of the decay models.

Chapter 4

Development of a Free-Wake lifting line model

This chapter gives a thorough description of the free wake lifting line code that has been developed. The first section explains the general theory on lifting line codes. Secondly the implementation of the lifting line theory for wind turbines is described. Finally initial verification tests are presented by comparing the predictions of the code with an analytic solution and another similar lifting line code.

4-1 Introduction to lifting line models

The first practical theory for predicting the aerodynamic properties of a finite wing was developed by Ludwig Prandtl and his colleagues at Göttingen during the period 1911-1918 [19]. The method is still in use today for design calculations of aircraft wings. The main assumption made by Prandtl is that he replaced a finite wing with a bound vortex filament which moves with the same fluid elements through the flow. The bound vortex filament experiences a lift-force equal to $L = \rho_\infty V_\infty \Gamma$. The bound vortex filament stretches from $-b/2$ to $+b/2$, however based on Helmholtz' theorem a vortex tube cannot start or end in a flow [31]. Therefore the bound vortex is part of a vortex ring with trailing vortices that extend infinitely far downstream of the wing, which leads to the well known horseshoe-vortex representation of a wing. In this way Kelvin's theorem is also satisfied which states that the total vorticity of a set of fluid particles remains constant in time.

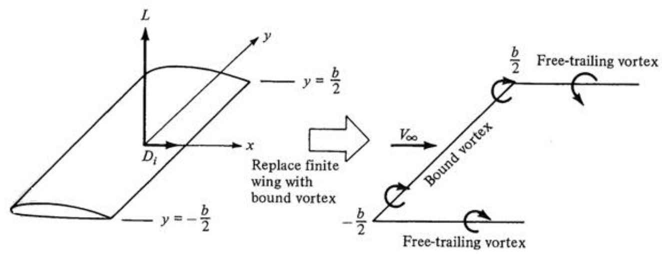

Figure 4-1: Replacement of a finite wing with a horseshoe vortex, *source:[19]*

Representing a finite wing by a single horseshoe-vortex is however not physically correct. For example the down wash $w(y)$ induced by the trailing vortices at the bound vortex can be evaluated with the following expression.

$$w(y) = \frac{-\Gamma}{4\pi(b/2 + y)} - \frac{\Gamma}{4\pi(b/2 - y)} \tag{4-1}$$

From this expression it is clear that the induced velocities approach infinity near the wing tips which cannot be true in a physical environment. Prandtl's solution to this problem was to represent the wing by a superposition of horse-shoe vortices as depicted in the following figure.

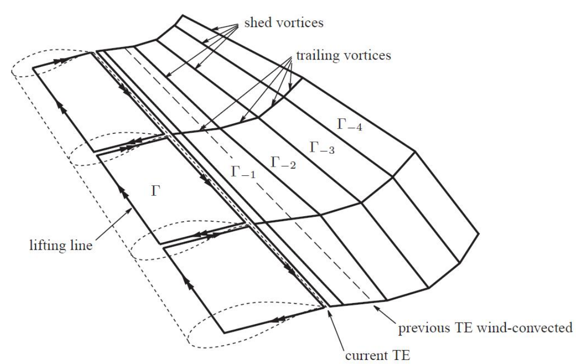

Figure 4-2: Superposition of a finite number of horseshoe vortices to represent a finite wing, *Source:[39]*

Mathematically one can even superimpose an infinite number of horseshoe-vortices which leads to a continuous bound vortex distribution and a continuous trailing vortex sheet. The down wash just upstream of the blade induced by all vortices at position y_0 can evaluated with the following integral.

$$w(y_0) = -\frac{1}{4\pi} \int_{-b/2}^{b/2} \frac{(d\Gamma/dy)dy}{y - y_0} \tag{4-2}$$

4-1-1 Analytic result for an elliptic wing

A famous analytic result in potential flow is the lift distribution that occurs for a wing with an elliptic planform at small angles of attack in steady flow conditions. The associated lift or bound circulation distribution is also elliptic.

$$\Gamma(y) = \Gamma_0 \sqrt{1 - \left(\frac{2y}{b}\right)^2} \tag{4-3}$$

With simple mathematics it can be shown that the downwash just upstream of the blade is constant and depends only on the wingspan (b) and the maximum bound vortex strength (Γ_0). This elegant result can be used as a benchmark case for numerical lifting line codes or panel methods. The numerical results should, depending on the grid resolution, be very close to the analytic solution.

$$w(y_0) = -\frac{\Gamma_0}{2b} \tag{4-4}$$

The value of Γ_0 can also be derived analytically using the lifting line theory. In [19] the following result is given for the constant lift coefficient along the span of an elliptic wing.

$$C_L = \frac{2\pi\alpha}{1 + \frac{2}{A}} \tag{4-5}$$

Where α is the geometric angle of attack and A the aspect ratio of the wing. Using this relation the following expression can be derived for Γ_0.

$$\Gamma_0 = \frac{4bV_\infty}{A+2}\alpha \tag{4-6}$$

Where b is the span of the blade and V_∞ the undisturbed free stream velocity.

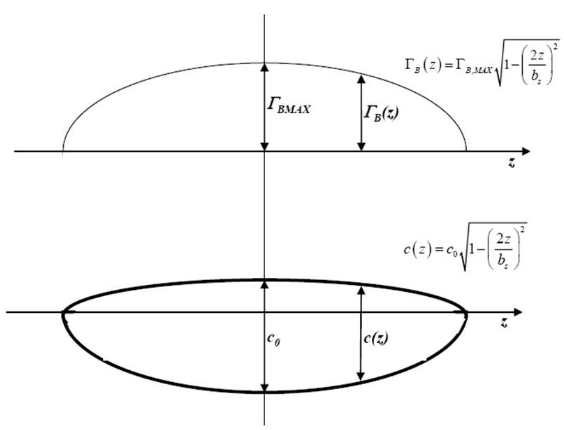

Figure 4-3: Geometry of an elliptical planform and associated lift distribution

4-2 Lifting line computations applied to a wind turbine

Wind turbines typically operate at wind speeds ranging between $3m/s$ and $25m/s$. Depending on the Tip Speed Ratio (TSR) the effective flow velocity at the tip will reach typically $80m/s$ for large multi-megawatt machines. At these flow velocities the air may still be considered as incompressible. Furthermore Reynolds numbers of large wind turbine will be in the order of $1 \cdot 10^6$ which means that viscous forces are small compared to inertia forces. Note however that drag forces can be included in the potential flow code by estimating the drag forces from $C_d - \alpha$ curves. From these observations it may be concluded that a potential flow approach is applicable for wind turbines.

The lifting line approach is chosen since it provides a reasonable estimate of the span wise lift distribution and performance of the turbine. A panel code as developed in [3] gives much more detail on the local pressure distributions. This is level of detail is not needed for research on the wake where the presence of the rotor is no longer predominant. The development of the wake is however for both methods very similar and therefore it is not required to use an advanced panel code for the development of the wake.

4-2-1 Geometry of the wake

The vortex sheet downstream of a wing that flies in a straight path is trailing behind the wing in the same direction. In case of a free wake the edges the sheet roll up due to the induction of the tip vortex. The structure of the vortex sheet downstream a rotating wind turbine blade is more complicated. Due to both the rotational and axial velocity components the wake obtains a typical helical shape (Figure 4-4).

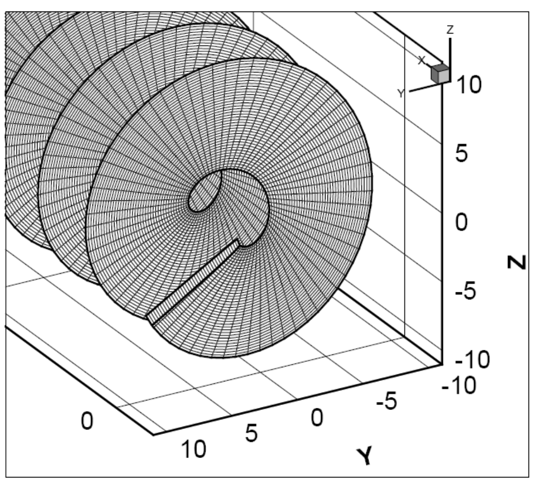

Figure 4-4: Helical wake structure behind a rotating blade

As visible in figure 4-4, the trailing vortex filaments follow a circular path. For numerical applications it is however difficult to use curved vortex filaments, therefore the wake is discretized in small straight vortex filaments. Depending on the resolution of the grid this discretization becomes more accurate.

4-2-2 Discretization of the wake

There are two ways of discretizing a vortex wake behind a rotating blade. The simplest method is to prescribe the geometry of the wake and divide it in a fixed number of radial and azimuthal nodes. With the known wake geometry it is possible to directly assess the bound circulation distribution for various wind speeds and rotational velocities. However, this so-called fixed-wake approach requires assumptions on the induction in the rotor plane and downstream of the rotor which means that the aerodynamic properties of the rotor have to be known to some extend before the simulation.

Instead of prescribing the wake it is possible to use a time integration method. In this case the position of the wake nodes is updated after each time step by calculating the influence of all vortex filaments in the grid on all wake nodes. After each time step new wake-nodes are released into the flow such that the wake gradually develops as time goes by. This approach does not require a predetermined assumption of the wake geometry and the induced velocities and is therefore more physically correct. Figure 4-5 shows how the grid is updated after each time step and the release of new wake nodes from the trailing edge of the blade.

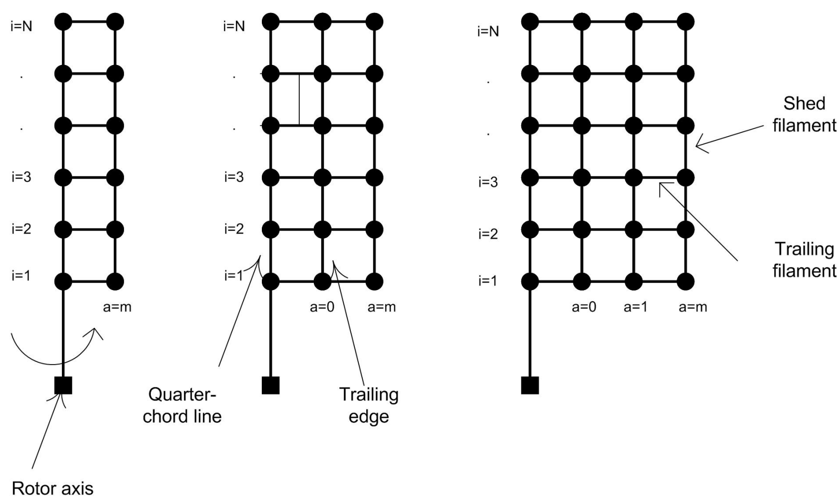

Figure 4-5: Structure of the mesh at $a = 0, a = 1, a = 2$, showing the extension of the mesh after each time step

4-2-3 Boundary and initial conditions

The main boundary condition for the solution of the entire system of blades and wake is based on Kelvin's theorem that states that the total circulation within the domain should remain constant or that the time rate of change of the circulation is equal to zero. The initial condition that the total circulation at $t = 0$ equals zero is automatically satisfied. In order to solve for the strength of the bound circulation different local boundary conditions are imposed that are discussed in section 4-4.

$$\frac{D\Gamma}{Dt} = 0 \tag{4-7}$$

The strength of the trailing and shed vortex filaments that are released during each time step depend on the bound vorticity (Γ_B) at the current and previous time-step. Bearing in mind that the total circulation in the domain should remain constant the following two expressions can be derived for the trailing and shed vortex strengths.

$$(\Gamma_T)_{i,m} = (\Gamma_B)_{i,m} - (\Gamma_B)_{i+1,m} \tag{4-8}$$

$$(\Gamma_S)_{i,m} = (\Gamma_B)_{i,m-1} - (\Gamma_B)_{i+1,m} \tag{4-9}$$

4-2-4 Discretization of blade and bound circulation

Performing numerical simulations means that continuous media have to be discretized in a finite number of elements. The same holds for the turbine blades and its associated lift distribution. Typically the lift distribution shows large gradients near the tip and root of the blade and is relatively constant in the middle sections. It is therefore convenient to cluster the radial stations near the root and tip which can be done with a cosine relation.

$$R_i = \left(\frac{R_r + R_t}{2}\right) - \left(\frac{R_t - R_r}{2}\right) cos(\gamma_i) \tag{4-10}$$

$$\begin{gathered} \gamma_{i+1} = \gamma_i + \tfrac{\pi}{N-1} \\ 0 \leq i \leq N-1; \gamma_0 = 0 \end{gathered} \tag{4-11}$$

In reality the strength of the bound vortex varies continuously along the span of the blade but is numerically discretized in $N-1$ sections that have a constant value across each section. Again the clustering of sections near the root and tip is desirable to reduce the numerical error in the areas with strong gradients.

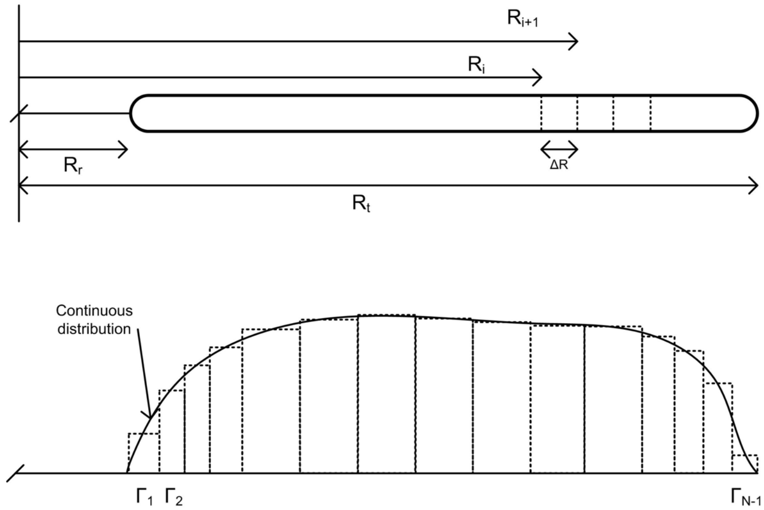

Figure 4-6: Discretization of the blade in N radial stations and $N-1$ discrete bound vortices

4-2-5 Evaluation of induced velocities in wake nodes

In order to properly describe the evolution of the wake, the influence of each vortex filament on all wake nodes must be evaluated during each time step. As mentioned in the previous chapter, the induction of any vortex filament on a point in space can be determined with the Biot-Savart law. Since in this case all vortex filaments are straight lines it is possible to simplify the Biot-Savart vector equation to three geometrical equations that represent the three components of the induced velocity in a particular point C. For a vortex filament with strength Γ that begins in point A, ends in point B and induces in point C the following relation holds for the induced velocity vector $\bar{V}_{ind}$.

$$\bar{V}_{ind} = \frac{\Gamma}{4\pi}\frac{(r_1+r_2)(\bar{r}_1\times\bar{r}_2)}{r_1 r_2(r_1 r_2+\bar{r}_1\cdot\bar{r}_2)} \tag{4-12}$$

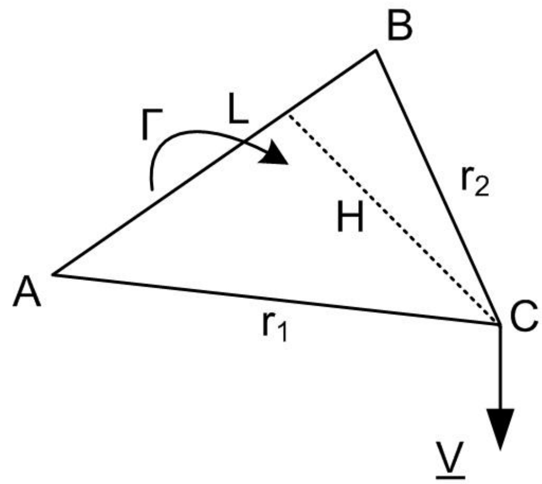

Figure 4-7: Schematization of vortex filament AB with strength Γ and length L inducing in point C

The vector relation above can be expanded into a geometrical relationship by expanding the dot and cross products giving three equations for the three induced velocity components $U_{ind}, V_{ind}, W_{ind}$.

$$U_{ind} = \frac{(r_1 + r_2)}{2\pi r_1 r_2 \left[(r_1 + r_2)^2 - L^2\right]} \left[(z_c - z_b)(y_b - y_a) - (y_c - y_b)(z_b - z_a)\right] \quad (4\text{-}13)$$

$$V_{ind} = \frac{(r_1 + r_2)}{2\pi r_1 r_2 \left[(r_1 + r_2)^2 - L^2\right]} \left[(x_c - x_b)(z_b - z_a) - (z_c - z_b)(x_b - x_a)\right] \quad (4\text{-}14)$$

$$W_{ind} = \frac{(r_1 + r_2)}{2\pi r_1 r_2 \left[(r_1 + r_2)^2 - L^2\right]} \left[(y_c - y_b)(x_b - x_a) - (x_c - x_b)(y_b - y_a)\right] \quad (4\text{-}15)$$

Where r_1, r_2 and L represent the sides of triangle ABC which can be determined as follows.

$$r_1 = \sqrt{(x_c - x_a)^2 + (y_c - y_a)^2 + (z_c - z_a)^2} \quad (4\text{-}16)$$

$$r_2 = \sqrt{(x_c - x_b)^2 + (y_c - y_b)^2 + (z_c - z_b)^2} \quad (4\text{-}17)$$

$$L = \sqrt{(x_a - x_b)^2 + (y_a - y_b)^2 + (z_a - z_b)^2} \quad (4\text{-}18)$$

These simple expressions can easily be evaluated for all grid nodes and vortex filaments if the grid-coordinates and the corresponding vortex strengths are known.

4-2-6 Modeling of viscous effects

The Biot-Savart equations show singular behavior as point C coincides with the vortex filament. Also induced velocities may become unrealistically high if point C is located close to filament $A-B$. This singular behavior can be dealt with by implementation of a viscous core model in the Biot-Savart equations. Moreover, the exponential increase for points near the filament is removed in this way.

A convenient model that can be easily implemented is the well known Lamb-Oseen vortex relation as presented in the previous chapter. The Lamb-Oseen vortex can be implemented in the code by multiplying the Biot-Savart law with a viscous parameter K_v which has been defined by Leishman in [24]. In this way, the induced velocity gradually decreases to zero as point C gets closer to the vortex center.

$$K_v = \frac{H^2}{(r_c^4 + H^4)^{1/2}} \tag{4-19}$$

An alternative approach of removing the singular behavior is by implementing a cut-off radius δ_r as suggested by van Garrel in [39]. This adaptation also makes sure that the swirl velocity smoothly goes to zero as point C approaches the vortex filament. Van Garrel suggests that for wake roll up calculations the cut-off radius should be between $1-10\%$ whereas a smaller value of 0.01% is suggested for bound vortex calculations at the blade (see [39]).

$$\bar{V}_{ind} = \frac{\Gamma}{4\pi} \frac{(r_1 + r_2)(\bar{r}_1 \times \bar{r}_2)}{r_1 r_2 (r_1 r_2 + \bar{r}_1 \cdot \bar{r}_2) + (\delta_r L)^2} \tag{4-20}$$

4-2-7 Position of the wake nodes

During every time step the position of all free wake nodes is updated. This is done by vectorially adding the free stream velocities and instantaneous induced velocities for every wake node ($\bar{V}_{node} = \bar{V}_\infty + \bar{V}_{ind}$). The new position of the wake nodes is then calculated with a simple explicit Euler scheme that uses an average of the current and previous node convection velocity to estimate the next position of each wake node. This method gives improved stability compared to a simple Euler forward method but still is first order in accuracy. In section 4-10 the implementation of higher order time integration methods is discussed.

$$\bar{X}_{t+1} = \bar{X}_t + \frac{1}{2}[(\bar{V}_{node})_t + (\bar{V}_{node})_{t+1}]\Delta t \tag{4-21}$$

4-2-8 Vortex filament stretching

In a free-wake vortex code the wake nodes are allowed to convect freely, thereby causing the vortex filaments to be strained. According to Helmholtz's third law, the net strength of a vortex filament should remain constant hence an increase in length of a vortex filament results in a reduction of the effective core size. Based on this theorem the core size of each filament in the wake is corrected for straining effects.

$$r_{c_{eff}} = r_c \left(\frac{1}{\sqrt{1+\epsilon}} \right) \tag{4-22}$$

It must be noted that this formula is derived based on the assumption that all vorticity of the vortex filament is concentrated in the vortex core and is constant along the radius of the core. For a Rankine vortex this assumption is true, but for the Lamb-Oseen model all vorticity is located within the first two core radii. An improvement may then be to integrate the vorticity along the radius of the core before calculating the new core size.

The vortex filament strain ϵ at time step t can be determined using the local node velocity $\bar{V}(t)$ by approximating the filaments length change ΔL during time increment Δt with an Euler forward discretization.

$$\epsilon = \frac{L + \Delta L}{L} \tag{4-23}$$

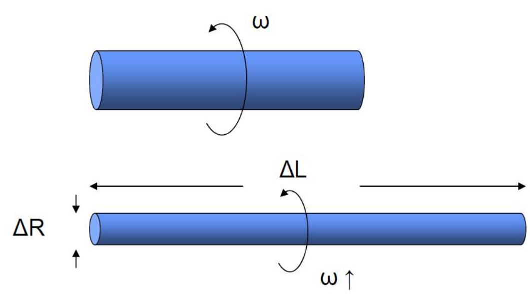

Figure 4-8: Modeling of vortex filament strain, *source:* [3]

4-3 Coordinate system

The code works with two sets of coordinate systems. The global or inertial system (X, Y, Z) has its origin in the center of the turbine hub. For each blade a local coordinate system (x, y, z) has been defined which has its origin at the blade root. The y-axis of the local system is aligned in span wise direction with the quarter chord line of the blade.

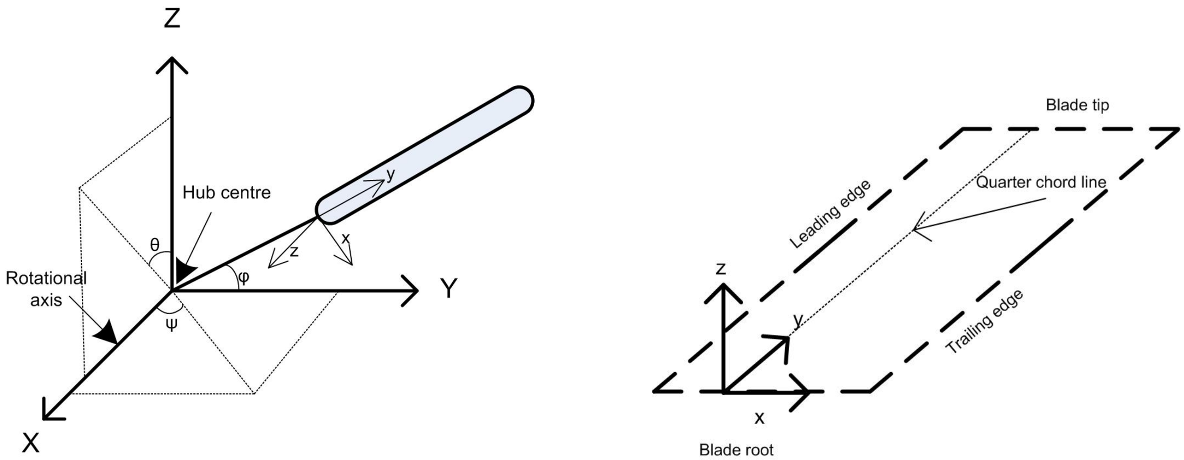

Figure 4-9: Global (left) and local (right) coordinate systems used in vortex code

Releasing wake nodes at the trailing edge of the blades during each time step requires knowledge of the position of each blade's trailing edge in the global coordinate system. This can be achieved by using coordinate transformation matrices that represent the rotations (ϕ, θ, ψ) around the X, Y and Z axes respectively. Furthermore the origin of the local system is translated with respect to the origin of the global system with a vector $[X_0, Y_0, Z_0]$. The coordinate transformation matrices to transform local- to global coordinates are defined as follows.

$$C_\phi = \begin{bmatrix} 1 & 0 & 0 \\ 0 & cos[\phi(t)] & sin[\phi(t)] \\ 0 & -sin[\phi(t)] & cos[\phi(t)] \end{bmatrix} \tag{4-24}$$

$$C_\theta = \begin{bmatrix} cos[\theta(t)] & 0 & -sin[\theta(t)] \\ 0 & 1 & 0 \\ sin[\theta(t)] & 0 & cos[\theta(t)] \end{bmatrix} \tag{4-25}$$

$$C_\psi = \begin{bmatrix} cos[\psi(t)] & sin[\psi(t)] & 0 \\ -sin[\psi(t)] & cos[\psi(t)] & 0 \\ 0 & 0 & 1 \end{bmatrix} \tag{4-26}$$

Local coordinates can now be translated to global coordinates as follows.

$$\begin{bmatrix} X \\ Y \\ Z \end{bmatrix} = C_\phi^T C_\theta^T C_\psi^T \begin{bmatrix} x \\ y \\ z \end{bmatrix} + \begin{bmatrix} X_0 \\ Y_0 \\ Z_0 \end{bmatrix} \tag{4-27}$$

4-4 Calculation of bound vortex strength

During every time-step the strength of the bound vortex is unknown and must be either prescribed or extracted from the local flow velocities at the control points. Prescribing the bound vorticity requires thorough aerodynamic knowledge of the blade under consideration. To enable more flexibility in the geometry of the turbine, it is useful to calculate the bound vortex instead. Two methods have been implemented in the code that are able to do so. The first method, from now on referred to as method one, matches the lift force that is calculated with the Kutta-Jukouwski theorem to the lift associated with the local flow direction through an iterative process. Method two is a direct method that uses a non-entry boundary condition, i.e. the flow velocity normal to a solid object should equal to zero.

4-4-1 Method one

As mentioned before, this method runs an iteration procedure at each time step to solve the strength of the bound vortex. The routine is based on the fact that the lift on a blade can be calculated using either the lifting line approach or sectional lift coefficients and local flow angle. By means of an iteration procedure, a solution is found. The required steps of the method are summarized below.

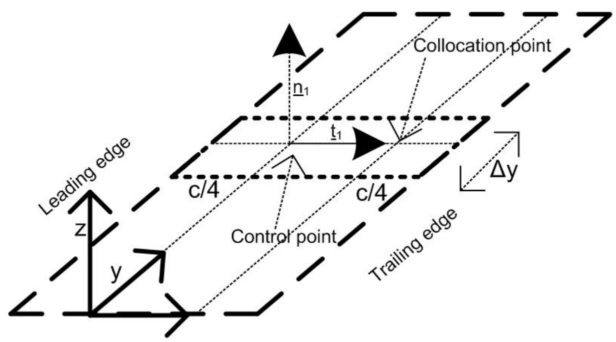

Figure 4-10: Spanwise segmentation of blade showing normal ($\bar{a}_1$) and tangential ($\bar{t}_1$) directions of a single blade panel

1. Divide the wing into N span wise stations. The control points are located at the quarter-chord point in the middle of two adjacent stations.(See figure 4-10)

2. Assume an initial lift distribution along the span. Either an elliptic distribution or the solution from the previous time step are useful options.

3. Calculate the total velocity vector as perceived by the blade due to induced velocities, wind speed and blade motion.

$$\bar{V}_{blade} = \bar{V}_{\infty} + \bar{V}_{ind} + \bar{V}_{motion} \tag{4-28}$$

The perceived velocity due to motion can be easily evaluated by numerical differentiation of the current and previous position of the blade.

$$\bar{V}_{motion} = -\frac{(\bar{X}_{t+1} - \bar{X}_t)}{\Delta t} \tag{4-29}$$

4. Determine the normal and tangential velocity in each station and calculate the effective angle of attack.

$$\alpha_{eff} = tan^{-1}\left(\frac{\bar{V}_{blade} \cdot \bar{n}_1}{\bar{V}_{blade} \cdot \bar{t}_1}\right) \tag{4-30}$$

5. Equate the lift due to circulation to the lift calculated with the angle of attack and find a new value for the circulation in every station.

$$\begin{aligned} \rho_\infty V_{blade}\Gamma &= \tfrac{1}{2}\rho_\infty V_{blade}^2 c_n c_{l_\alpha} \alpha_{eff} \\ \Gamma &= \tfrac{1}{2}\rho_\infty V_{blade} c_n c_{l_\alpha} \alpha_{eff} \end{aligned} \tag{4-31}$$

6. Update the input value of the circulation in each station, where D is a damping factor that is required to prevent the solution from diverging. Experience has found that values of D are typically on the order of 0.05.(See [19])

$$\Gamma_{input} = \Gamma_{old} + D(\Gamma_{new} - \Gamma_{old}) \tag{4-32}$$

7. Repeat the previous steps until a user defined convergence has been obtained. In this case the method is cut-off if the maximum difference with the previous step is less than one percent.

4-4-2 Method two

Alternatively it is possible to solve for the bound vortex with a direct method. The basis of this method is that the flow cannot enter a solid object, i.e. the flow should be tangential to the surface of the blade. This tangency requirement is imposed in collocation points located at the three-quarter-chord points. Choosing this location is not random because in 2D flow imposing the tangency condition at $3c/4$ gives exactly the same result as using thin airfoil theory. Summarizing, for every collocation point the following equation must be solved.

$$(\bar{V}_\Gamma + \bar{V}_\infty + \bar{V}_{wake} + \bar{V}_{motion}) \cdot \bar{n} = 0 \tag{4-33}$$

Where $\bar{V}_\Gamma$ is the induced velocity by the bound vortices and first set of trailing vortices. $\bar{V}_{wake}$ represents the influence of all trailing and shed vortices that are in the wake.

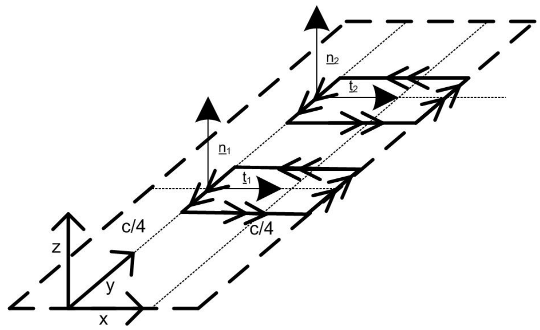

Figure 4-11: Positioning of unit-strength vortex rings on the blade

Instead of assuming an initial lift distribution, the wing is covered with vortex rings that have unit strength. Now the influence of every vortex on every collocation point can be determined by evaluating the Biot-Savart law. This results in a matrix of influence coefficients $a_{i,j}$ that represent the influence of vortex i on point j. The tangency condition can now be expressed as a matrix-vector equation.

$$\begin{pmatrix} a_{1,1} & a_{1,2} & \cdots & a_{1,N} \\ a_{2,1} & a_{2,2} & \cdots & a_{2,N} \\ \vdots & \vdots & \ddots & \vdots \\ a_{N,1} & a_{N,1} & \cdots & a_{N,N} \end{pmatrix} \begin{bmatrix} \Gamma_1 \\ \Gamma_2 \\ \vdots \\ \Gamma_N \end{bmatrix} = - \begin{bmatrix} (\bar{V}_\infty + \bar{V}_{wake} + \bar{V}_{motion}) \cdot \bar{n_1} \\ (\bar{V}_\infty + \bar{V}_{wake} + \bar{V}_{motion}) \cdot \bar{n_2} \\ \vdots \\ (\bar{V}_\infty + \bar{V}_{wake} + \bar{V}_{motion}) \cdot \bar{n_N} \end{bmatrix} \tag{4-34}$$

The inverse of this matrix equation can simply be found, which directly gives the solution for the unknown vortex strengths.

Note that it is not convenient to include the sectional characteristics of the airfoil explicitly for this method. Therefore the applicability of this method is limited to wings or blades that operate at small angles of attack and have a lift curve slope of approximately $C_{l_\alpha} = 2\pi$.

4-5 Initialization and flowchart of the code

The governing equations needed for calculating the relevant numerical parameters have been presented in the previous section while the focus of this section will be the structure of the code. A numerical time-marching algorithm has been implemented in the code. Before this algorithm can function properly it requires input data which is summarized below.

1. Data of blade geometry: chord (c) and twist (θ) distributions, number of blades (B), amount of radial stations (N_b), root radius (R_r) and tip radius (R_t)

2. Operating conditions: Free stream velocities ($U_\infty, V_\infty, W_\infty$), TSR ($\lambda$), turbulence intensity (TI), yaw angle (Ψ), air density (ρ)

3. Numerical parameters: Number of azimuthal steps N_ϕ and number of revolutions N_{rev}
4. Options: bound circulation method, core growth model, turbulent decay, near wake nodes treatment, filament strain, initial core size method.

If all input parameters are known the code is ready to start the calculations. It must be noted here that the code does not start impulsively but is gradually sped up during the first twenty time steps. In this way, the starting vortex is not shed immediately which prevents the code from becoming unstable due to large sudden changes in the bound vortex strength. Furthermore, an impulsive start is physically not possible hence this approach mimics reality more closely. Many vortex codes assume a constant rotational velocity of the rotor however in this case it is chosen to determine the rotational velocity from the TSR which enables temporal variations in free stream velocity. Figure 4-12 summarizes the different calculation steps for every time-step.

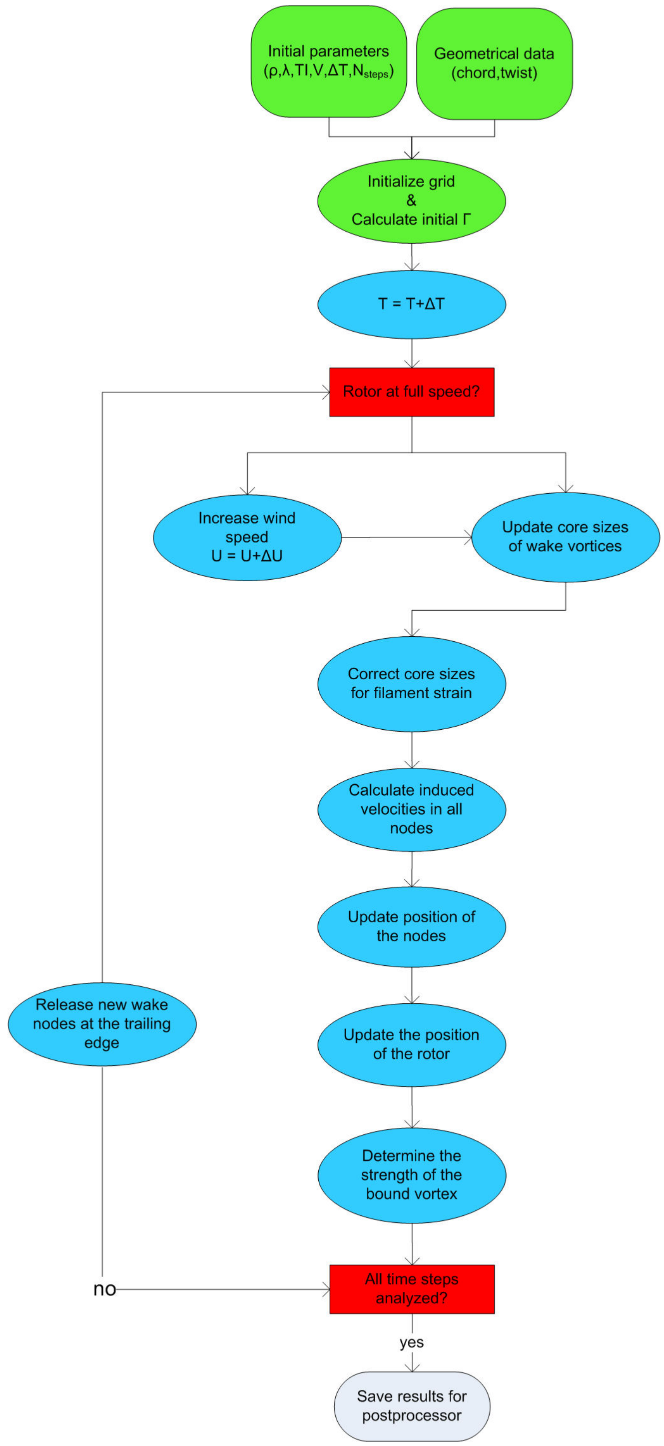

Figure 4-12: Succession of calculations of free wake vortex code during a simulation

4-6 Airfoil interpolation

Depending on the structural and aerodynamic requirements, a wind turbine blade contains multiple airfoils along its span. A realistic simulation of the blades forces requires a method that is able to cope with the different airfoils along the blade. Method two is not suitable in this case since airfoil data is not explicitly taken into account. Implementing various airfoils along the span should however not be a problem within method one. In the code discrete breaks are defined for the transition between two types of airfoils. This may give rise to discontinuities in lift and drag distributions along the blade. In reality the transition from one airfoil to the other should be smooth and continuous. Therefore the code is adapted in such a way that it can interpolate between the sectional characteristics to ensure a smooth transition from one airfoil to the other. The definition of airfoil break locations along the blade are depicted in Figure 4-13.

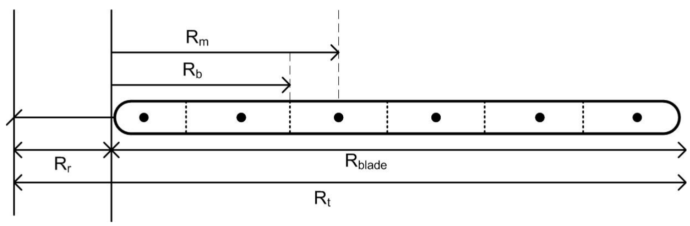

Figure 4-13: Definition of airfoil break locations (R_b) and mid points (R_m) along the blade span

The code is able to interpolate either between the break points R_{b_i} or between the mid points R_{m_i} that are located in the middle between the break points. The value of the lift in a point R located somewhere between two interpolation boundaries can now be linearly averaged as follows:

$$C_L(R) = \frac{(r - R_{b_i})C_{L_{i+1}} + (R_{b_{i+1}} - r)C_{L_i}}{R_{b_{i+1}} - R_{b_i}} \tag{4-35}$$

The drag can be interpolated in a similar way or one could use the mid points as interpolation boundaries. As an example, figure 4-14 shows how the interpolation routines can change the solution. When using no interpolation the solution shows jumps at the airfoil locations, whereas the linear interpolation schemes show a gradual transition between the breakpoints.

It must be noted that this interpolation method is a purely numerical artifact; in reality one must be careful when interpolating the properties of airfoils, since small variations in airfoil shape can lead to large differences in lift and drag characteristics. It may therefore be possible that the transition between two airfoils is non-linear as opposed to the linear model used here.

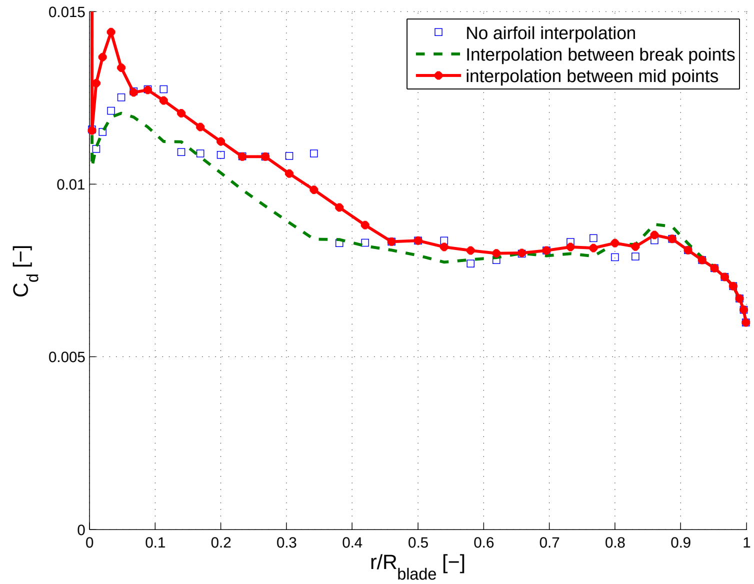

Figure 4-14: Effect of different interpolation methods on the C_l distribution along the span of the blade showing discrete jumps or a smooth transitions between different types of airfoils

4-7 Simplification to a prescribed wake

The most time consuming calculation of the free wake vortex code is the evaluation of the induction of the wake onto itself. By predefining the geometry of the wake a lot of calculation time can be saved. Downside of this simplification is that the wake roll-up process and expansion is not captured reducing the physical validity of the model. Also in case of yawed flow a prescribed wake model is less suitable than a free wake model. However in this thesis the focus is on axial inflow. A prescribed wake model is therefore suitable to quickly perform some test cases. Before doing so one should be aware of the differences between a fixed and free wake model for axial flow.

The following figure shows the difference between the wake development of a fixed and free wake simulation. Clearly the initial expansion and the roll-up of the wake is not present in the right figure, nor are the instabilities that occur at the end of the wake. The colors in the plot represent the strength of the trailing vortices. The free wake plot clearly shows the roll-up process of the wake whereas the fixed keeps its helical structure. For the fixed wake it is assumed that all wake nodes are convected with an axial velocity of $U_{nodes} = 2/3U_{\infty}$, which corresponds to the optimal induction factor that is derived from momentum theory.

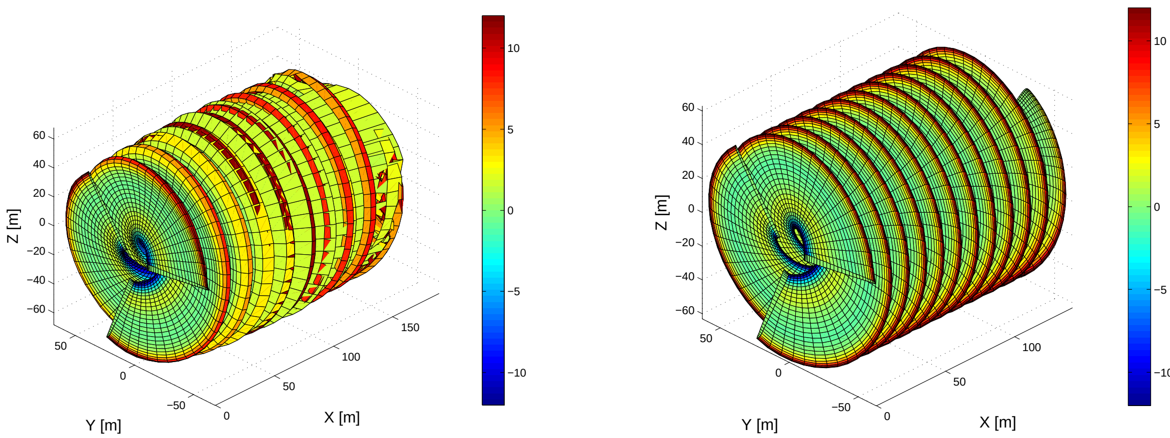

(a) Free wake (b) Prescribed wake

Figure 4-15: Surface plot of fixed and free wake, $N_b = 30$, $N_{rev} = 4$, $N_\phi = 50$, Colors correspond to strength of trailing vortices Γ_t

Figure 4-16 shows the differences in bound vortex strength distribution and the vertical induced velocity profile at $1D$ downstream between a fixed and free wake solution. Clearly, the free wake calculation gives locally higher values for the bound vortex strength. Possible cause is the fact that the first shed vortices remain a bit closer to the blade in the free wake case, which causes locally higher induced velocities. Further downstream the induced velocities are lower than the fixed wake case, hence the wakes travels faster downstream. Also the axial induced velocity profile has a different shape which is mainly caused by the roll-up of the vortex sheet.

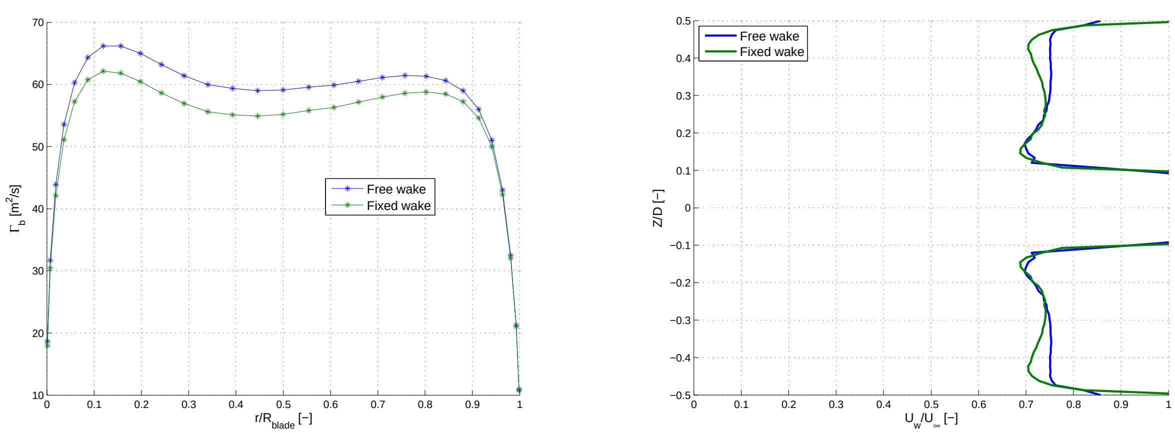

(a) Bound vortex (b) Wake profile $1D$

Figure 4-16: Bound vortex distribution along the blade and vertical velocity deficit profile for fixed and free wake, $N_b = 30$, $N_{rev} = 4$, $N_\phi = 50$

4-8 Grid study

A fundamental step that must be taken before further analysis of the code is a thorough grid study. A heavy grid captures the flow in detail but requires much more computation time than a coarser grid. Therefore it is important to make a trade-off between computation time and solution accuracy. In this section the effect of the number of blade nodes (N_b), number of azimuthal steps N_ϕ and the number of revolutions (N_{rev}) is considered. The effect of the resolution of the sampling plane (N_{wake}) on the induced velocities downstream in the wake is also taken into consideration. To save calculation time the first part of the grid study is performed with a prescribed wake instead of a free wake.

4-8-1 Effect of number of blade nodes and azimuthal steps

Five simulations have been performed with increasing N_b and N_ϕ. Figure 4-17 and shows how the lift distribution and velocity profile change with increasing number of blade nodes and azimuthal steps. The lift distribution for $N_b = 20$ is slightly lower in the middle of the blade and relatively unsmooth. For $N_b = 40$ the solution is much smoother and compares better to the solutions at $N_b = 50$ and $N_b = 70$. It must be noted that blade nodes are clustered near the root and tip of the blades in order to capture the strong gradients that occur in that area. Also the velocity profile does not change significantly for mesh sizes larger than $N_b = 40$.

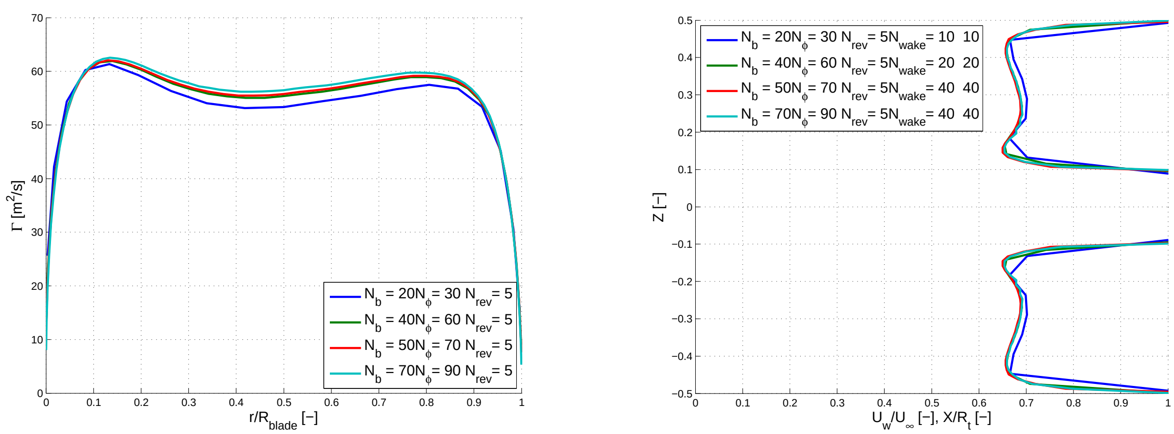

Figure 4-17: Effect of N_b and N_ϕ on bound vortex distribution $\Gamma_b(y)$ and vertical velocity deficit profile $U_w(z)$ at $1D$ downstream

Instead of considering the absolute values of lift and induced velocities, more insight can be gained by observing the convergence of the code as a function of grid size. Figure 4-18 shows the convergence of the solution. The error is calculated in two different ways. The first way is to calculate the absolute percentage difference of a relevant simulation parameter (ξ) and its reference (ξ_{ref}). Typically the reference solution is taken from the simulation performed with the finest grid. It is clear that the relative error goes down with increasing grid size which is a sign of convergence of the solution.

$$\epsilon = \left| \frac{\xi - \xi_{ref}}{\xi_{ref}} \right| \tag{4-36}$$

In order to reduce ϵ to a single value the error is quadratically averaged, which gives the so-called R^2-norm.

$$\epsilon_{R^2} = \frac{\Sigma_{i=1}^{N} \epsilon_i^2}{N} \tag{4-37}$$

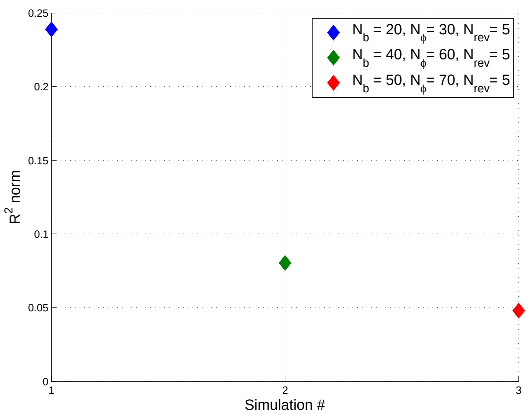

(a) $\Gamma_b(y)$

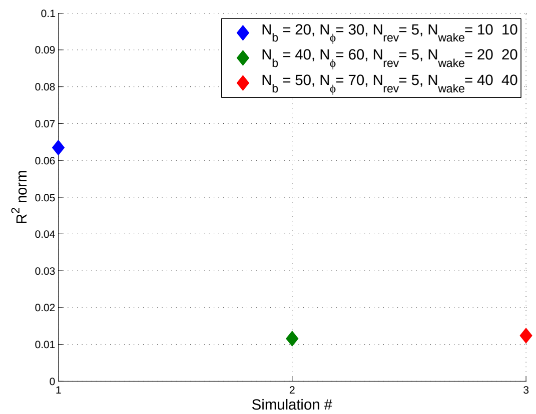

(b) $U_{we}(z)$ at $1D$

Figure 4-18: Effect of N_b and N_ϕ on $\Gamma_b(y)$ and $U_w(z)$; reference simulation: $N_b = 70$, $N_\phi = 90$, $N_{rev} = 5$

4-8-2 Effect of number of revolutions

As the number of revolutions (N_{rev}) increases the wake will accordingly extend further downstream. At some point the shed vortices are convected so far away from the blade that their influence on the blade becomes negligible. In that case the solution has converged and the simulation can be stopped. Since in this case the attention is focused on the wake, it is important to have insight in the number of revolutions or downstream convection of the wake that is required before the induced velocities at different downstream positions reach a steady state.

The axial induced velocities are calculated at $0.5D$, $1D$ and $2D$ for an increasing number of revolutions. With increasing N_{rev} the wake travels, depending on the tip vortex pitch, further downstream. For interpretation of the results it is beneficial to use the non dimensional downstream travel distance (X/D) instead of N_{rev}. The behavior of the mean error as a function of downstream distance is depicted in figure 4-19. From the results can be derived that after ten rotations the wake has traveled sufficiently far downstream to obtain a converged velocity profile at $2D$ downstream.

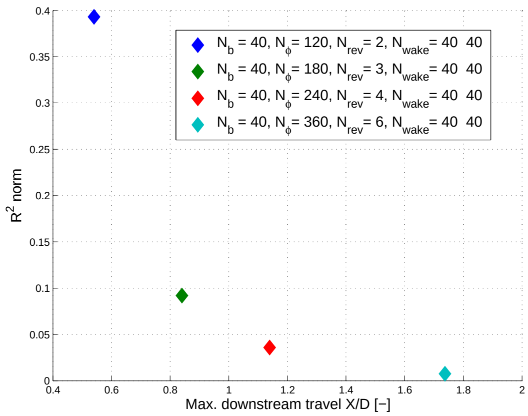

(a) $0.5D$

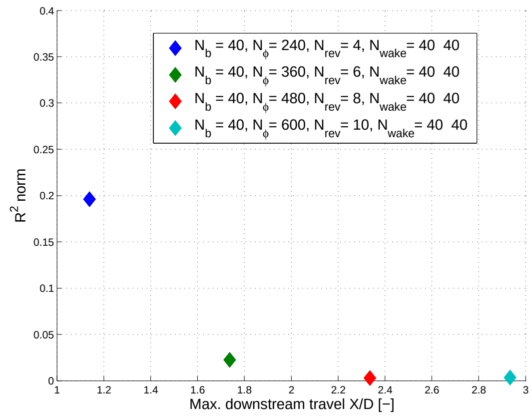

(b) $1.0D$

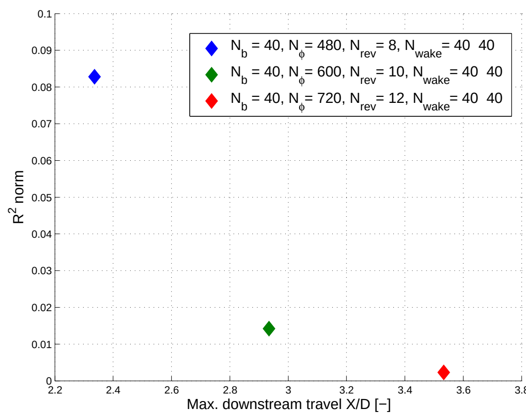

(c) $2.0D$

Figure 4-19: Effect of the maximum downstream travel distance of the wake (X/D) on $U_w(z)$ at $0.5D$, $1D$ and $2D$ downstream

4-8-3 Effect of sample volume on velocity profile

As mentioned before the velocity profile of the wake is obtained by calculating the induced velocities of all vortices in a vertical and circular plane located at a particular downstream position. Subsequently a 2D velocity profile is obtained by averaging over the azimuth of the vertical disk.

Vortex filaments that are sufficiently far away may not have a negligible influence on the induced velocities in the sampling plane. Instead all vortex filaments located within a cylinder with a particular dimension (D_{sample}) that is centered around the vertical disk may be sufficient to obtain a correct velocity profile. Hence Figure 4-20 shows the effect the sample volume D_{sample} on the mean squared error in the velocity profile

A sampling volume of $2D$ is already quite accurate and gives an error of approximately 4%. The wake is typically evaluated at $0.5 - 2D$, this means that all upstream vortices

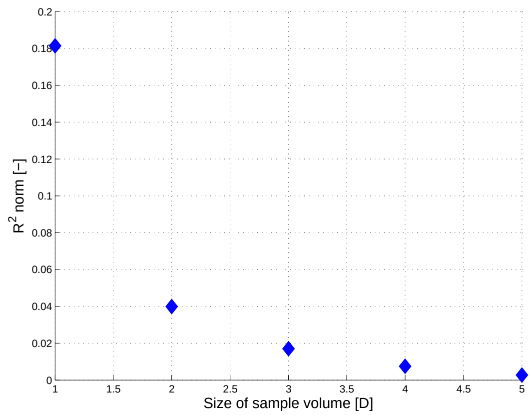

Figure 4-20: Effect of D_{sample} on velocity profile; reference simulation: $N_b = 40$, $N_\phi = 60$, $N_{rev} = 15$, $D_{sample} = 6D$

should be included in the velocity profile calculation and, depending on N_{rev}, all or part of the downstream vortices.

In conclusion it may be stated that it is important to apply a sufficient number of revolutions and sample volume to obtain consistent results when evaluating the wake at different downstream locations. The number of span wise blade nodes and azimuthal steps are less critical, typically $N_b = 40$ and $N_\phi = 60$ give satisfactory results.

4-8-4 Convergence of free wake code

The previous analyses have been performed with a prescribed wake only. Similarly, the convergence of the free wake code should be tested since calculating the position of the wake during every time step is an extra source of numerical errors. The maximum resolution that is used as a reference is lower than in the previous cases since the calculation time increases quadratically with the number of grid points in the wake. For example in this case the calculation of the reference simulation took up to 48 hours on a single workstation using only one CPU.

Clearly, also the free wake code converges and depending on the required accuracy of the calculation N_b should be between $30 - 40$ and N_ϕ between $50 - 60$.

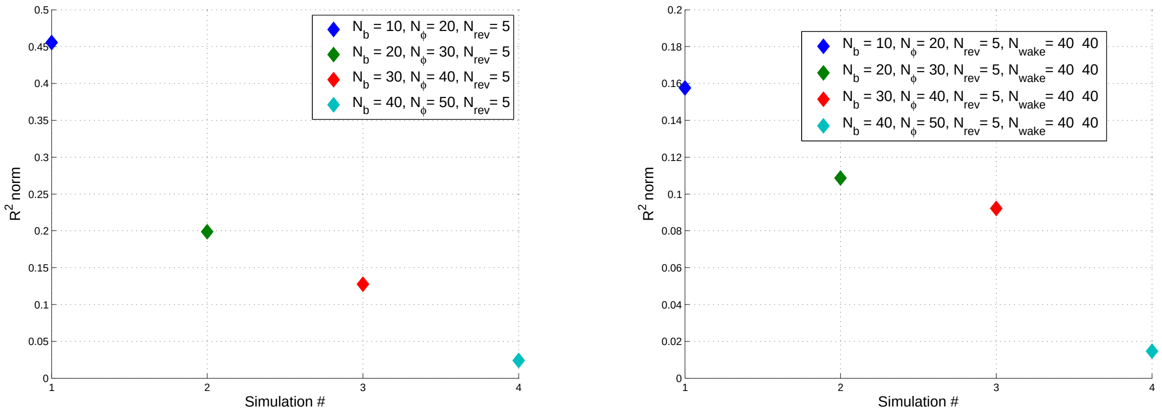

(a) $\Gamma_b(y)$ (b) $U_w(z)$ at $0.5D$

Figure 4-21: Effect of grid size on $\Gamma_b(y)$ and $U_w(z)$ at $0.5D$ downstream in case of a free wake simulation; reference simulation: $N_b = 50$, $N_\phi = 60$, $N_{rev} = 5$

4-9 Verification of the code

4-9-1 Comparison with the analytic solution for an elliptic wing

A nice test case that gives immediate comparison of the code with an analytic solution is the case of an elliptic wing that is flying straight ahead. As known from theory an elliptical planform should give an elliptical lift distribution and a constant downwash along the span of the blade. This case can be mimicked by the code by rotating a blade with a very large root radius, in this way the blade virtually flies straight ahead. Table 4-1 summarizes the case that is examined for using both routines to calculate the bound vortex strength.

Table 4-1: Geometry of elliptic wing simulation

Parameter	Value	Unit
c_0	2	m
R_r	1000	m
R_t	1010	m
U_∞	2	m/s
λ	10	-
θ	0	deg
N	40	-
Δt	0.1	s

Results from the Angle of Attack routine very closely match with the analytic solution as presented in the following two figures. The downwash is constant along the span of the blades except for the tips where a strong increase is visible. Unfortunately the direct non-entry method is slightly off compared to the analytic solution. A possible

4-10 Reduction of computation time

A disadvantage of the Free Wake time integration is the high computational costs. Simulations on a coarse mesh can be performed within a few hours but a similar simulation with a very fine mesh takes a couple of days. To calculate the induced velocities on mesh with NxM points, a number of N^2xM^2 calculations need to be performed every time step. This explains why the calculation time increases rapidly with the size of the mesh. Especially for commercial use it is desirable to be able to reduce the computation time and still achieve an accurate solution.

4-10-1 Parallel computation of Biot-Savart law

By far the most demanding calculation during every time step is calculating the induction of every trailing and shed vortex filament in the wake on every wake node. These calculations are however mutually independent and are therefore suitable to be carried out in parallel.

Nowadays many desktop and laptop computers are standardly equipped with a dual-core processors; slightly more expensive computers may even posses quad-core processors. These processors are able to carry out heavy computations in parallel, or use only one core for calculation and another for normal usage of the operating system. By default Matlab uses only one of the cores and therefore only half of the total computational capacity of the dual-core processor. However the latest versions of Matlab are able to perform calculations in parallel by using a parallel for-loop or *parfor*. This feature in Matlab allows multiple processor cores and can therefore, depending on the number of cores, speed up the computation considerably.

The subroutine *velocity.m* has been modified to allow for the usage of the *parfor* loops. Using two cores does not reduce the computation time by a factor of two since all other subroutines are still carried out on a single core. Moreover it takes a while to initialize the multiple Matlab sessions that are required to calculate in parallel. Much more can be gained by using a quad-core processor or a cluster of computers.

4-10-2 Predictor/Corrector method

Currently, time integration is performed with a simple Euler explicit first order method. The accuracy of the calculations can be increased by implementing a second order method such as the modified Euler or Predictor/Corrector method [4] and [24]. By applying a simple Euler forward method the new position of the wake nodes is predicted.

$$\bar{X}_{pred} = \bar{X}_t + (\bar{V}_{node})_{t+1}\Delta t \tag{4-38}$$

Based on the predicted position of the wake nodes the velocity field is re-evaluated giving V_{pred} and applied to finally calculate the corrected position of the wake nodes based on V_{node} and V_{pred}.

$$\bar{X}_{t+1} = \bar{X}_t + \frac{\Delta t}{2}[(\bar{V}_{node})_{t+1} + (\bar{V}_{pred})_{t+1}] \tag{4-39}$$

Downside of this method is the fact that every time step two evaluations of the induced velocities are required which may slow down the computations considerably. However a higher accuracy is obtained with a smaller grid size; for example to double the accuracy the first order method requires a reduction in time step by a factor of two whereas a second order method only requires a reduction with a factor of $\sqrt{2}$. In terms of calculation time and accuracy the methods are therefore comparable.

4-10-3 Adams-Bashforth method

The previously mentioned Predictor/Corrector methods requires two calculations of the induced velocity field per time step. As this is an intensive calculation it is desirable to use a scheme that requires only one calculation during every time step. An example is the Adams-Bashforth method. Similar to the explicit Euler scheme that is used by default this method uses the induced velocity field from the current and previous time step giving the following relation.

$$\bar{X}_{t+1} = \bar{X}_t + \frac{3\Delta t}{2}(\bar{V}_{node})_{t+1} - \frac{\Delta t}{2}(\bar{V}_{node})_t \tag{4-40}$$

The Adams-Bashforth method is more unstable than the Euler and Predictor/Corrector methods and requires a time step that is twice as small. This makes the method not particularly faster than the Euler method but may give more accurate solutions on a coarser grid.

Both methods have been implemented in the vortex code. Unfortunately there has not been enough time to perform a sufficient amount of simulations for comparison with the Euler time integration scheme.

Chapter 5

Validation of the vortex code with PIV and Hot Film measurements

This chapter gives an overview of the different validation studies that have been performed to verify the performance of the vortex code in the near wake region. Section 5-1 presents a comparison between the vortex code and Hot-Film measurements at very small distances downstream of the rotor. The evolution and decay of the tip vortex at low turbulence levels within the first diameter is studied by means of Particle Image Velocimetry (PIV) measurements and compared with predictions from the vortex code. Additionally, a validation study is presented of the vortex core models that are described in chapter 3 and also implemented in the vortex code.

5-1 Hot-Film measurements in rotor region

Lifting line methods for wind turbines are mostly used to predict the forces on the rotor blades and flow field close to the rotor. Typically in this region, the flow is not governed by drag forces which justifies the potential flow approach as used in the vortex code. Note however that part of the wake viscosity is included by the implementation of the viscous core models as mentioned in the previous chapter. Before proceeding with any further validation studies, it is necessary to validate that the code captures the physics of the flow in the rotor region.

5-1-1 Test set-up

A series of experiments were carried out in the Delft University of Technology open jet tunnel facility. The experiments consisted of detailed hot-film measurements in the near wake and smoke visualization experiments to trace the tip vortex path. Measurements have been performed in both yawed and axial conditions, however in this case the attention is focused on the axial flow case. The measurement campaigns were part of the PHD projects of T. Sant and W. Haans. An extensive description of the measurements and post processing of the results can be found in [32]; the final report by W. Haans is yet to be published.

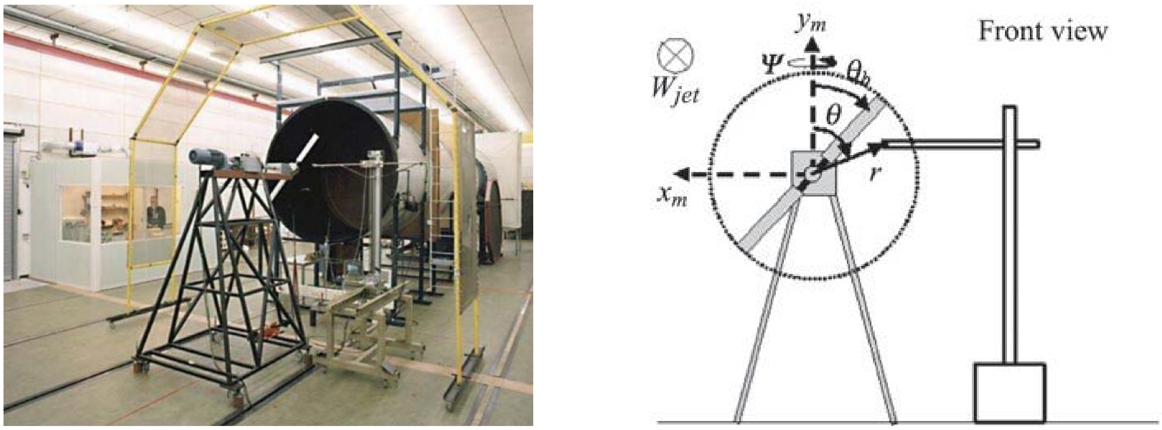

Figure 5-1: Open jet wind tunnel and model rotor, *Source: [32]*

Table 5-1 summarizes the geometric specifications of the rotor that was used during the measurement campaign.

Table 5-1: Geometry of TU Delft rotor

Parameter	Value	Unit
B	2	-
c	0.08	m (constant)
D	1.2	m
Rr	0.18	m
θ	$\theta(r/R) = (6 + \theta_{tip} - 6.67(r/R), 0.3 \leq (r/R) \leq 0.9$	$^\circ$
	$\theta(r/R) = \theta_{tip}, 0.9 \leq (r/R) \leq 1$	$^\circ$

The following measurements were performed, a more detailed description of the measurements is given in reference [32] and [11].

- The ambient wind speed of the jet equals $5.5m/s$ and the Tip Speed Ratio (TSR) of the rotor was fixed at 8.
- Measurements were taken using a Hot Film probe in vertical planes located at 3.5, 6.0 and $9.0cm$ downstream of the rotor, i.e. $0.0219D$, $0.05D$ and $0.075D$.
- The probe position is located at 7 radial stations along the blade and 24 stations in azimuthal (θ_b) direction.
- At each station the induced velocities are calculated for 180 azimuthal positions of the rotor with a step size of 2 degrees.

- Velocities are calculated using the so-called Phase Locked Average (PLA) procedure which means that velocities corresponding to a certain positions of the rotor are sampled for a number of cycles and then averaged over the amount of cycles. In this way, measurement uncertainties are reduced.

- Similar measurements have been carried out for different yaw angles of the rotor. The model should be able to deal with yawed flow, but in this case only axial flow conditions are considered.

5-1-2 Results

As mentioned before measurements are taken at 24 azimuthal stations and sampled for 180 positions of the rotor. Assuming uniform inflow conditions, the velocity contours corresponding to each of the 24 positions are similar in shape but shifted by 15 degrees relative to each other. Correcting for this phase shift allows calculating an averaged velocity contour plot for every downstream position with a resolutions of $7x180$ data points. In this way, uncertainties in the measurements are reduced. Note that this method of data reduction is only allowed in axial flow conditions with constant inflow and TSR.

A similar picture can easily be produced with the vortex code by simply calculating the induced velocities in the same vertical planes as used in the measurements. As opposed to the measurements the induced velocities are calculated only once and are not sampled multiple times. The simulated measurement plane has $180x40$ nodes in azimuthal and radial direction respectively which is fine enough compared to the spatial resolution of the measurement mesh. The nacelle area has not been included in the calculations here since only the blades are modeled in the vortex code.

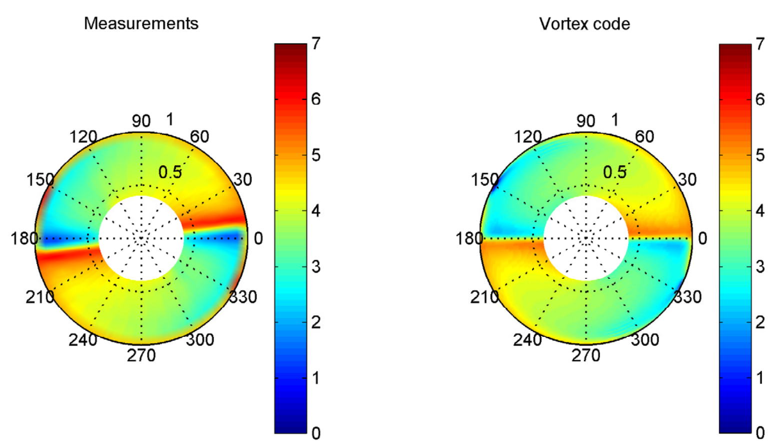

Figure 5-2: Comparison of vortex code and measurements at $3.5cm$ or $0.0219D$ downstream, colors represent axial velocity in the wake U_w, simulation settings: $N_b = 40$, $N_{rev} = 4$, $N_\phi = 65$, Measurements: 7 radial and 180 azimuthal points

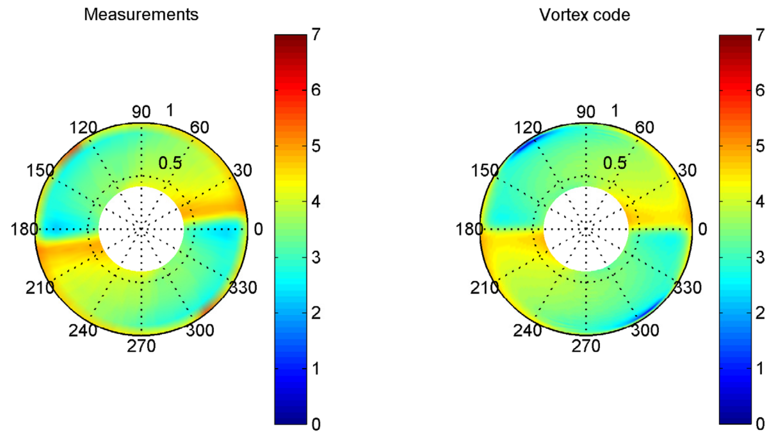

Figure 5-3: Comparison of vortex code and measurements at $6.0cm$ or $0.05D$ downstream, colors represent axial velocity in the wake U_w, simulation settings: $N_b = 40$, $N_{rev} = 4$, $N_\phi = 65$, Measurements: 7 radial and 180 azimuthal points

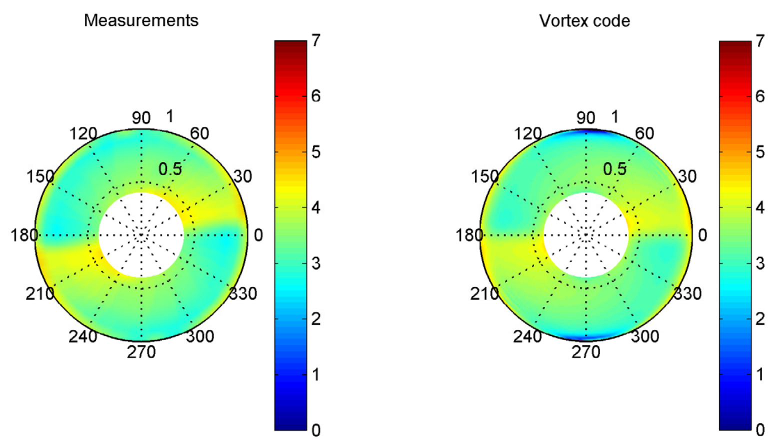

Figure 5-4: Comparison of vortex code and measurements at $9.0cm$ or $0.075D$ downstream, colors represent axial velocity in the wake U_w, simulation settings: $N_b = 40$, $N_{rev} = 4$, $N_\phi = 65$, Measurements: 7 radial and 180 azimuthal points

The measurements clearly show that the passage of the blade becomes less apparent as the probe is moved further away from the rotor. The simulation matches particularly well with the measurements at $6.0cm$. At $3.5cm$, the vortex code underestimates the up- and downwash near the blades edges which may be due to neglecting the thickness of the blades in the code.

Another striking result are the differences in induced velocities at the location where the tip vortex passes the plane. All measurements show an increase in axial velocity whereas the simulation shows a strong decrease. This means that the simulation shows a stronger wake expansion i.e. outward travel of the tip vortex than the measurements. Haans and Sant did not perform any measurements at radial positions larger than the rotor radius which would give more information on the position of the tip vortex and the differences between the code and the measurements.

5-2 Introduction to the MEXICO project

Previously in section 5-1 the vortex code has been validated using measurements of the very near wake. The velocities in the wake where evaluated at not more than $0.1D$ downstream. This comparison showed the ability of the vortex code to predict the induction in the rotor plane and near wake very well. Other verification tests of the code like the elliptic wing and comparison with a GE internal code have supported the results of the model.

Of course it may be expected that the vortex method performs well in the rotor region, the typical high Reynolds numbers of wind turbines justify the inviscid approach that forms the basis of the vortex method. Initially the wake has a very clear spiraling vortex structure which in the end due to mixing and viscous effects breaks up forming the typical Gaussian shaped wake that is often observed in the far wake. Although the model in this thesis does include viscous effects in the form of vortex decay models, the break down of the vortex structure and mixing effects are not captured. This implies that the model is only applicable in the region of the wake where the vortex structure still exists. Sant [32] shows by means of smoke visualizations that the vortex structure remains at least up to 1D downstream. Smoke trails are however quite diffusive which may show an earlier brake up of the tip vortex. Another disadvantage of smoke trail studies is their qualitative nature which makes is hard to extract information on vorticity and swirl velocities. More quantitative information about the flow can for example be obtained by means of PIV measurements.

To improve the physical understanding of the flow around the rotor and in the near wake of a wind turbine a series of wind tunnel experiments have been carried out at the Large Low-speed Facility (LLF) of the Duits Nederlandse Windtunnels (DNW) with a model wind turbine under controlled conditions; hence the name Model Experiments In Controlled Conditions. A thorough measurement campaign of the near wake behind a model wind turbine has been performed as part of the Model Experiments In Controlled Conditions (MEXICO) project. Detailed PIV pictures of the tip vortex as a function of downstream position are available. These measurements may give information on the vortex structure of the wake and the strength and decay of the tip vortex. Furthermore, the performance of the vortex method can be evaluated in terms of the ability to predict the position and strength of the tip vortex.

5-2-1 LLF tunnel:

Data from wind tunnel experiments should always be interpreted with care because scaling, wind tunnel wall or blockage effects may influence the flow to such an extent that comparison with full scale data is no longer valid. For example the rotor mentioned in [32] and section 5-1 has a chord length of $c = 8cm$; with a free stream of $U_\infty = 5m/s$ and TSR of $\lambda = 8$ gives a Reynolds number in the order of $Re = 200000$. Much less compared to a full scale rotor. For that reason model rotors should be tested at higher tunnel speeds or at lower temperatures to maximize Reynolds numbers.

Wind turbines are designed to effectively block or slow down the incoming flow. This means that testing a rotor in a closed test section may give significant blockage errors in the measurements that need to be accounted for. The LLF open jet facility is therefore a suitable wind tunnel. The dimensions of the test section are $9.5x9.5m$ allowing measurements on a relatively large model rotor, reducing the blockage and increasing the Reynolds number. In the test section flow speeds up to $62m/s$ can be achieved, well beyond the maximum operational wind speeds of full scale wind turbines.

Figure 5-5: LLF open jet tunnel from DNW

5-2-2 Model rotor:

The model used for the measurements has been specially designed for the goals of the MEXICO project. Since the LLF tunnel has a large test section an advanced model has been constructed that resembles a large industrial wind turbine. The machine has three blades that are both tapered and twisted and have three different airfoils along the blade. The rotor can be operated at variable pitch and rpm, but the rotor was typically kept at a constant rpm of 425.5 or $7Hz$. Along the blade the rotor is equipped with pressure sensors to measure the aerodynamic loads. Also strain gauges are installed at the blade roots to measure the bending moments. Finally the entire model is placed on a six-component balance to measure the forces and moments at the tower base. More detailed information on the rotor is presented in Appendix B.

Figure 5-6: MEXICO rotor in the LLF on the six component balance

5-3 PIV measurements

One of the most successful flow measurement techniques that emerged in the past decades is Particle Image Velocimetry or PIV. This technique allows measuring the instantaneous velocity field in a nonintrusive way which makes this technique appealing as a quantitative flow visualization tool as compared with smoke stream-traces or time lines. The principle of PIV is based on the measurement of the displacement of small tracer particles that are carried by the fluid during a short time interval. The tracer particles must be sufficiently small to accurately follow the fluid motion and not alter the fluid properties or flow characteristics. The tracer particles are illuminated within a thin light sheet generated from a pulsed light source, and the light scattered by them is recorded onto two subsequent image frames by a digital imaging device, typically a CCD camera placed perpendicular to the measurement plane. If two camera's are used the out of plane motion of the particles can be captured as well giving the full three dimensional instantaneous flow field. To obtain the flow field, two pictures of the flow are taken shortly after each other. The recorded images are fed into a computer that divides the pictures into small sub domains or interrogation windows. A cross-correlation analysis is performed on the interrogation windows yielding, combined with the hypothesis of uniform motion within the window during the time interval, the mean velocity vector in the interrogation window. Figure 5-7 gives a schematic of a typical PIV measurement set-up.

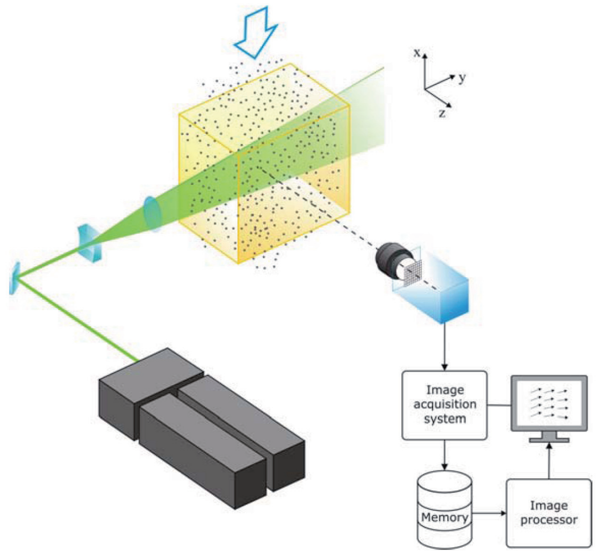

Figure 5-7: Schematic of typical PIV measurement system, *source: [33]*

In this case the seeding of tracer particles was done with tiny water bubbles that were introduced to the flow in the settling chamber of the tunnel. The time differences between two recording equals 200 nanoseconds. The size of the PIV sheet are $40x37cm$ with a spatial resolution of $0.0043m$ in both directions.

As depicted in Figure 5-8 the camera's can be moved such that the flow can be measured at various up and downstream positions of the rotor. The following PIV measurement campaigns have been performed on the MEXICO rotor: (see also [8])

- Two radial traverses between $y/R = 0.61$ and $y/R = 1.29$ at both $x/R = 0.066$ up- and downstream of the rotor. The measurements have been performed for six rotor azimuthal positions with a step size of 20°. These measurements may help to improve tip correction factors for BEM calculations.
- Two axial traverses between $x/R = -1.92$ and $x/R = 2.54$ at both $y/R = 0.61$ and $y/R = 0.82$.
- By means of trial and error the tip vortex has been tracked up to a distance of $x/R = 2$ downstream. These measurements give information on strength, position and decay of the tip vortex as it is convected downstream.

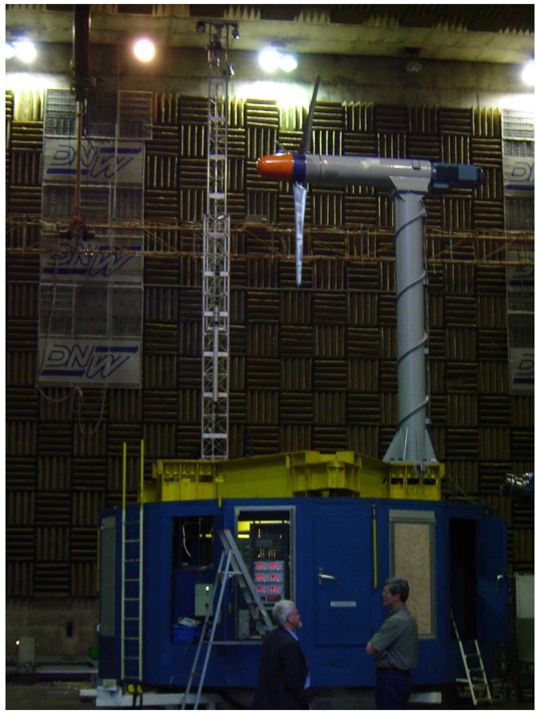

Figure 5-8: PIV camera's mounted to the traversing systems

5-4 Measurement and development of the tip vortex

The ability to focus the PIV camera's at different radial and axial positions allows for measuring the evolution of the flow field in the wake of the turbine. Within the first diameter downstream in the wake it is particularly interesting to track the position and strength of the tip vortex. The dimensions of the PIV plane are however no more than $40cm$ making it difficult to capture the tip vortex nicely centered in the PIV plane. Depending on the rotor thrust and tip speed ratio, the radial and downstream position of the tip vortex can be estimated and with a bit of trial and error the flow field in the neighborhood of the tip vortex was tracked up to $1D$ downstream in the wake, Figure:5-9.

Scatter on the data is reduced by calculating the PLA of each PIV plane using 30 samples. Each sample is recorded at the moment that blade three passes the PIV plane corresponding to an azimuth position of 240°.

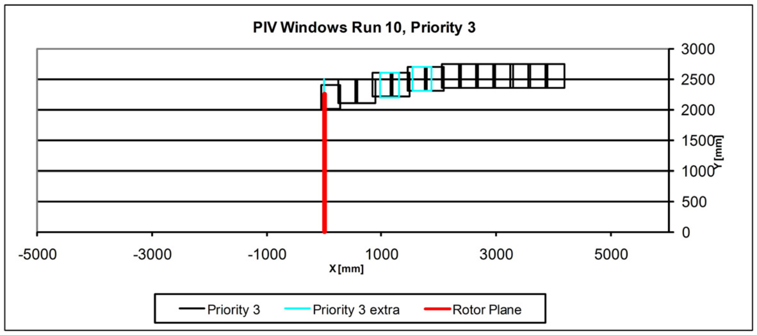

Figure 5-9: PIV Measurement planes at $U_\infty = 15m/s$ and $\lambda = 6.7$, *Source: [8]*

It is preferred that the tip vortex is nicely centered in the PIV plane such that the core and the surrounding flow field is captured correctly. Manual selection of the data gives six PIV planes that show a very clear picture of the tip vortex centered in the measurement plane. The age difference between two PIV planes is 120° following from the fact that the MEXICO rotor is a three bladed machine. The last plane that clearly shows the tip vortex is recorded at approximately $0.8D$ downstream which corresponds to a wake age of approximately 600°. Figure 5-10 displays the radial and downstream positions of the PIV planes, with the colors corresponding to either non dimensional vorticity or absolute velocity. Especially the plots of the vorticity allow an easy identification of the vortex core since this region typically contains very high vorticity whereas the flow outside the core is much more reminiscent of the classical potential vortex flow.

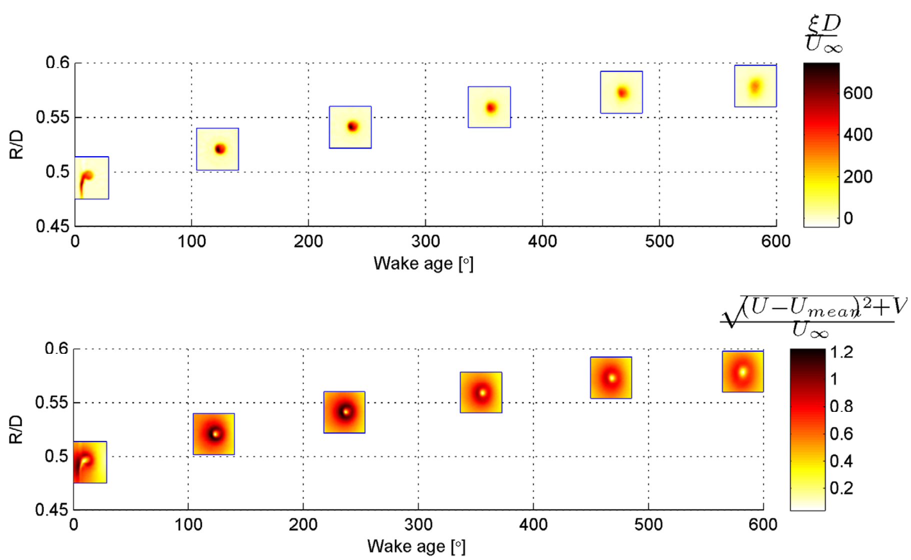

Figure 5-10: Measured tip vortex velocity and vorticity ($\xi D/U_\infty$) fields

5-4-1 Interpolation of the measurement data

As mentioned before the difference in age between the tip vortices as they pass the $X-Y$ plane is one third of a rotation or 120°. This means that the first PIV plane shows the tip vortex of blade three, the second image shows the tip vortex of blade two and the third shows the vortex of blade one. The fourth PIV plane is then again the tip vortex from blade three. Alternatively the image can be interpreted differently by assuming that the circulation distribution for all blades is constant i.e. the tip vortices have the same strength. In this case the turbine is operating in an almost uniform flow at very low turbulence intensities which validates the previous assumption. With the previous statements in mind, figure 5-10 can be interpreted as the evolution of a single tip vortex with a step size of one third of a rotation.

The raw measurement data can now be used to interpolate the position and strength of the tip vortex with a step size that is much smaller than the current 120°. For example the first two PIV pictures give the tip vortex flow field at azimuth positions of 0° and 120°; by means of a $3D$ linear interpolation routine the position and flow field of the tip vortex can be estimated at different azimuthal positions with a step size of 10°. The interpolation routine is summarized in the following steps:

1. Identify the position of the tip vortex core. This is done by making an initial guess of the core position visually and then looking for the maximum vorticity in the region of the estimated core position.

2. Define a new coordinate system for each PIV plane with its origin at the vortex core.

3. Define intermediate azimuth angles and use the $3D$ interpolation routine in Matlab to estimate the parameters X_i, R_i, U,V and W at the intermediate azimuthal positions. Basically this interpolation is not a pure interpolation in $3D$ space but local coordinates around the vortex core are used to estimate the absolute position and flow field at the intermediate positions. The following figures explains the routine more visually.

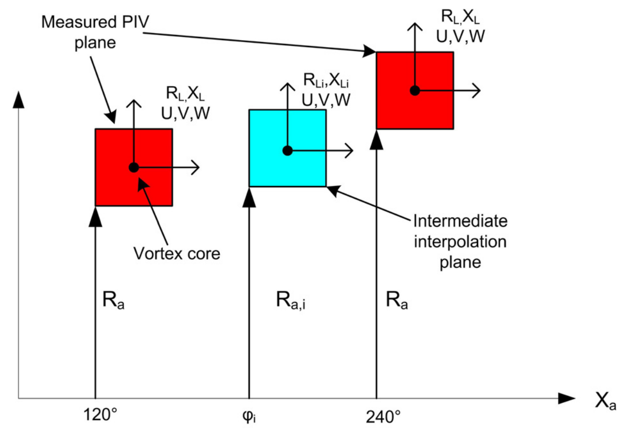

Figure 5-11: Visualization of the PIV interpolation routine showing measured PIV planes with absolute coordinates X_a, R_a, wake ages $120°$ and $240°$, and local coordinates coordinates X_L and R_L used to interpolate position and velocity at intermediate wake age ϕ_i with $120° \leq \phi_i \leq 240°$

Applying this interpolation routine gives the interpolated coordinates and in-plane velocities (U, V, W) at the required azimuthal positions. The results of the interpolation routine can be depicted in a similar manner as in figure 5-10. Note that the interpolated velocities are the in-plane velocities and are not expressed in the global inertial reference frame, the coordinate transformation is however relatively straightforward.

Note that figure 5-10 does not show all of the intermediate interpolated PIV panels otherwise the planes in the figure would overlap. The interpolation now shows a smooth transition between two measured PIV planes. Especially in the vortex core there is a strong decay of vorticity and swirl velocity due to the strong viscous forces that act on the flow. Moreover, remainders of the boundary layer from the blades cause an increased level of turbulence in the core give an additional source of vorticity decay.

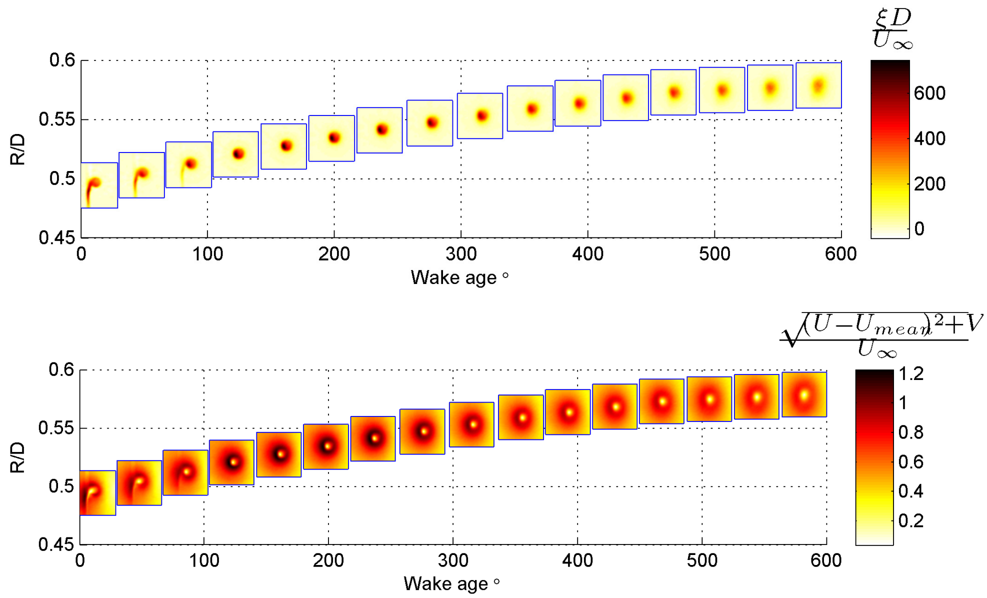

Figure 5-12: Interpolated tip vortex velocity and vorticity fields

5-4-2 Verification of interpolation routine

The main assumption of the interpolation routine is that linear interpolation is allowed between two measurements to calculate the tip vortex velocities for intermediate wake ages. The difference in wake age between two measured tip vortices equals 120° or one third of a rotation. These are quite significant steps and may give false or unrealistic velocity distributions for the the intermediate wake ages.

To test the assumption that linear interpolation is allowed, the interpolation is carried out one more time but now with the omission of one measurement plane that corresponds to a wake age of 240°. If a linear interpolation is valid there should be no significant differences between the two results. Figure 5-13 shows that the mean differences in velocities are in the order of two to four percent of the free stream velocity and the differences in position are less than one percent of the length of the PIV plane L_{PIV}. The maximum error occurs at 240° exactly were the omitted measurement plane would be located. On occasion however large differences occur locally, especially near the vortex core as small differences in core location estimation can give significant differences in flow velocities close to the core. But in general, the differences are small compared to U_∞ and the size of the PIV plane. This results therefore confirms that linear interpolation is indeed a valid approximation.

In an attempt to improve the interpolation a spline routine has been applied as well that uses more information than only the two neighboring PIV planes. The results are however not significantly better.

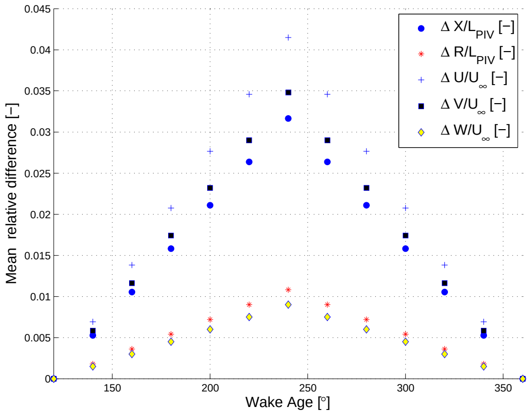

(a) linear

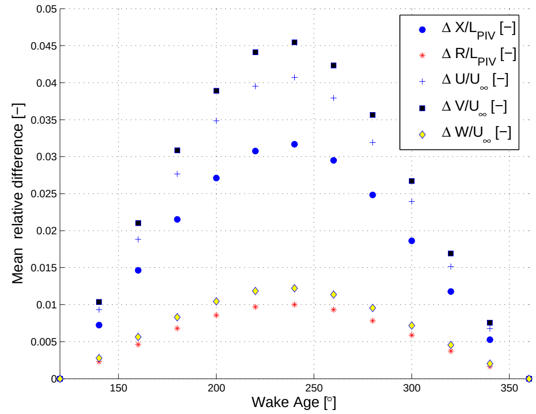

(b) spline

Figure 5-13: Effect of omission of measurements on interpolation of tip vortex position and velocities compared to interpolation using all of the available measurements

5-5 Comparison of the vortex code with the measurements

5-5-1 Three dimensional iso vorticity

An alternative way of presenting the interpolated data by transforming both the positions and in-plane velocities to the global coordinate system. In this way a measured and interpolated 3D iso-vorticity plot can be constructed showing the development of the tip vortex in 3D. Additionally, the solution from the lifting line code is added to the plot in transparent blue clearly showing that the position of the tip vortex is captured by the lifting line code. Depending on the chosen iso-vorticity level the shape of the iso-surface changes, a characteristic vorticity level can be estimated by $\xi_{iso} = \pi U_\infty / c$ which is a common factor to normalize a vorticity field. Using a lower iso-vorticity level gives a wider tube and sometimes even multiple tubes whereas a high value gives a narrow tube.

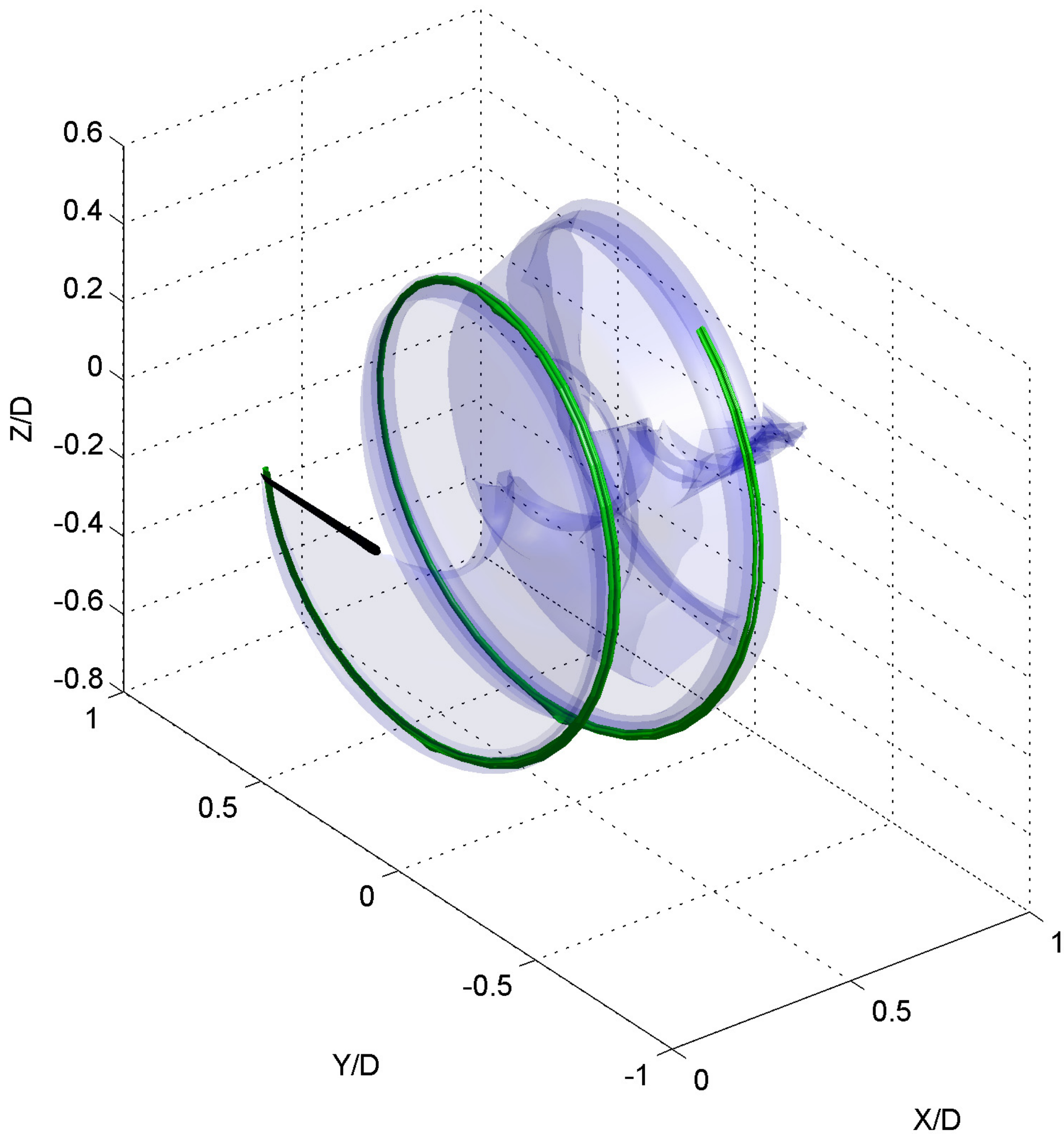

Figure 5-14: iso-vorticity surface of the tip vortex and free wake solution, $\xi_{iso} = \pi U_\infty / c$, green surface: measured and interpolated iso-vorticity surface, blue: position of the vortex sheet according to free wake simulations

5-5-2 Position of the tip vortex

The presence of the rotor induces a significant reduction in the wind speed behind the rotor hence the stream tube in which the rotor is located should expand to satisfy the conservation of mass. This expansion of the wake is also visible in the measurements explaining the outboard motion of the tip vortex with downstream distance. The potential flow model as used in the lifting line code should of course also satisfy the conservation of mass meaning that the wake expansion as observed in the measurements should be captured as well. Initial simulations showed however few wake expansion and a too large tip vortex pitch; it turned out that the blade pitch in the simulation was not defined correctly giving a too low thrust coefficient of $C_t = 0.56$. A lower rotor thrust means a smaller velocity deficit behind the rotor causing of course fewer wake expansion and an increased tip vortex pitch. Correct input settings gave however a much better correlation between the measured and simulated tip vortex positions as depicted in Figure 5-15. Note that it is not trivial to clearly define the simulated tip vortex position as the tip vortex in the simulation is represented by a number of vortex filaments that mimics the roll up behavior of the vortex sheet.

The initial wake expansion or outboard motion of the tip vortex is clearly driven by inviscous processes, explaining the good correlation between the measurements and simulations. Further downstream the wake continues to expand until eventually completely disappears. It is however more likely that this far-wake expansion is driven by viscous processes and turbulent mixing between the outer free stream flow and the wake. Moreover, in the far wake the vortex wake will not longer exist and has broken down in two much smaller scale eddies. Therefore, this model will not be able to capture the physics of the wake in the far wake i.e. at distances larger than one or two diameters downstream.

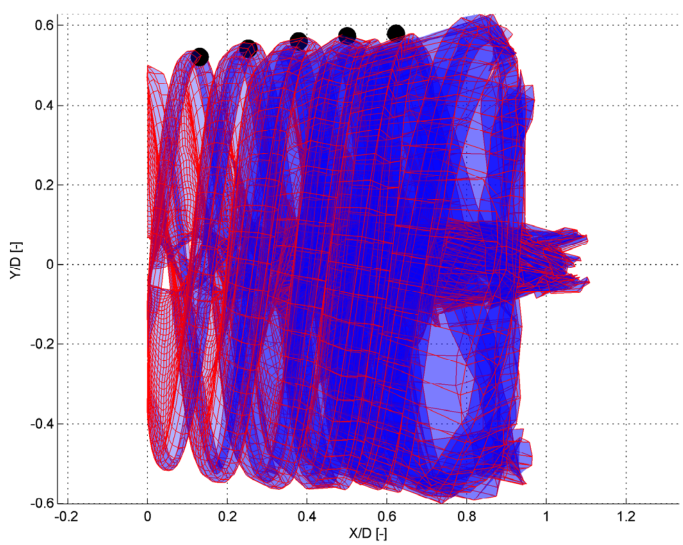

Figure 5-15: Comparison between measured and simulated tip vortex position at $C_t = 0.82$. Black dots show the measured positions of the tip vortex core.

5-5-3 Simulated and measured flow field

The previous analysis has shown that the vortex code is capable of capturing the position of the tip vortex quite accurately. A question that remains is whether the vortex code is able to reproduce or approximate the measured flow field in and around the tip vortex. The PIV measurements show that a single tip vortex emanates from each blade, decaying as it travels downstream. A free wake vortex code represents the tip vortex by a number of trailing vortices that roll around each other mimicking the behavior of the tip vortex. To evaluate the performance of the vortex code in this case, the induced velocities have been calculated in horizontal planes with the same coordinates and dimensions as the original PIV planes.

The simulated flow field completely different than the measurements. The regions of high vorticity are approximately at the correct location but the resulting flow field does not resemble the discrete vortex that is observed in the PIV measurements. Increasing the mesh resolution by a factor of two does not improve the solution dramatically, although the calculation took almost a week to complete. Performing the same simulation with an even finer mesh is therefore not a suitable option. Solutions must be found by trying to implement a second order time integration scheme which may give a much better approximation than the explicit Euler scheme which of the order $O(\Delta x)$.

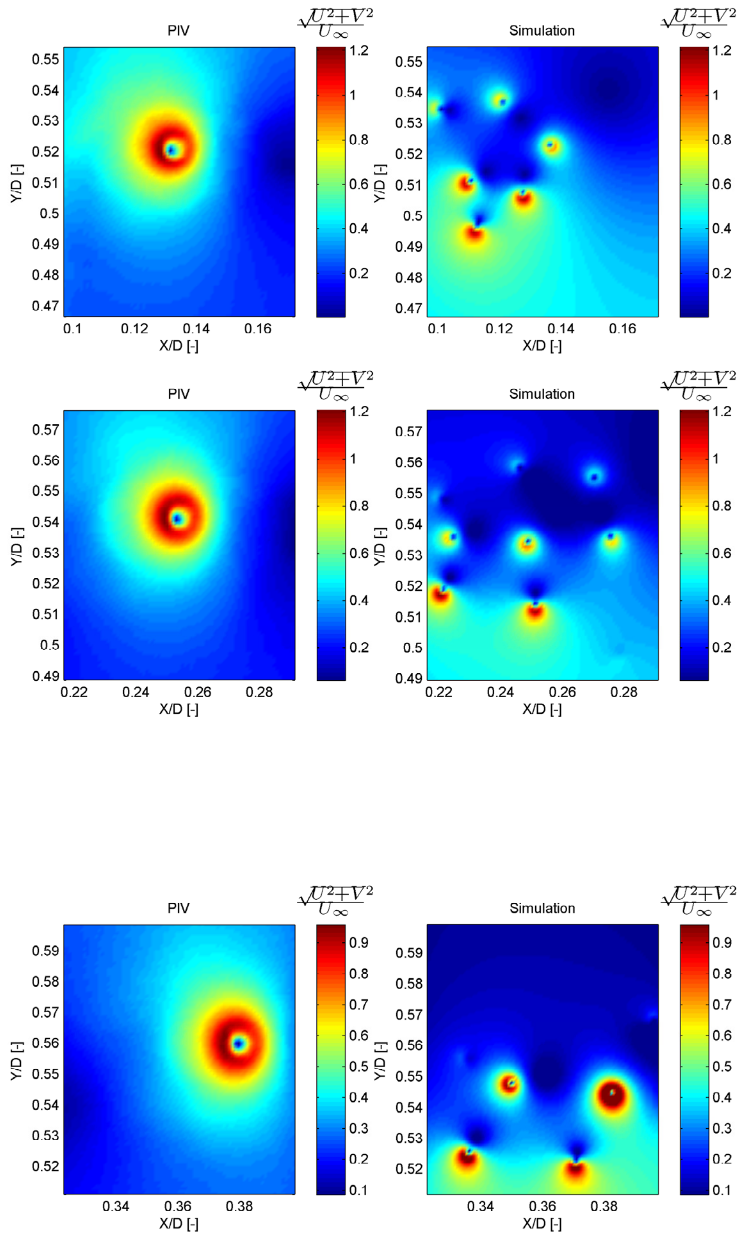

Figure 5-16: Comparison of simulated and measured induced velocities, simulation settings: $N_\phi = 50$, $N_b = 40$, $N_{rev} = 5$

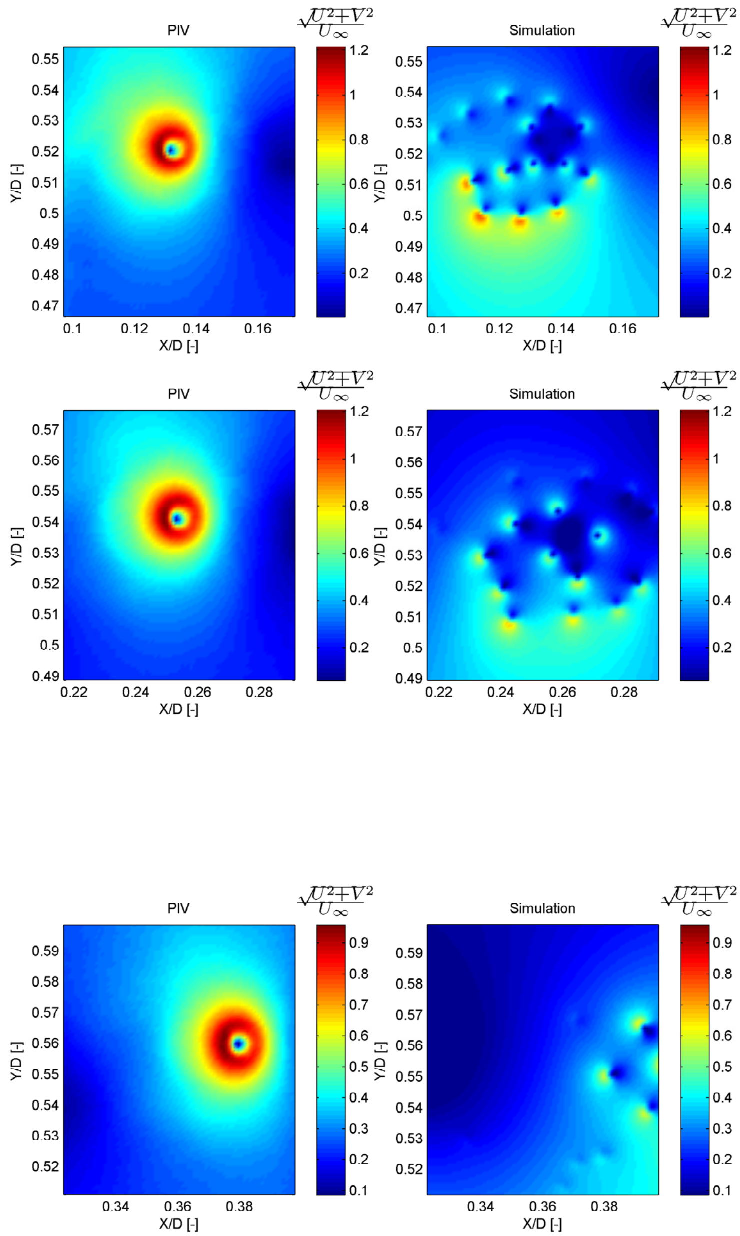

Figure 5-17: Comparison of simulated and measured induced velocities, simulation settings: $N_\phi = 80$, $N_b = 80$, $N_{rev} = 3$

Another possibility is comparing the total circulation strength given by the measurements and the PIV measurements. Problem with this analysis is that one does not know how many filaments should be considered as being part of the tip vortex. If only the last filament is taken into account the vortex strength is of course underestimated whereas on the other hand using all filaments may overestimate the total circulation strength. This unknown number of vortex filaments can then be used as a kind of tuning factor to match the simulated and measured vortex strength. Although this exercise is relatively straightforward it may not give any further insight in the behavior of the tip vortex which can possibly lead to a better vortex roll-up model.

Maybe more information on the formation and the strength of the tip vortex can be derived by comparing the ratio between the bound vortex strength and the eventual fully developed tip vortex. In this way one obtains insight in the redistribution of vorticity as it is shed from the blade into the vortex sheet and tip vortex. Vemeer shows in [40] that the strength of a fully developed tip vortex is approximately 80% of the maximum bound vortex strength. Similar results are obtained in this case but it must be noted that the maximum simulated bound vortex strength is used as a reference in this case. Results may be more accurate if the bound circulation is derived from the inflow measurements but should be in the same order of magnitude. Calculation of the tip vortex strength from measurements is described in section 5-7-3.

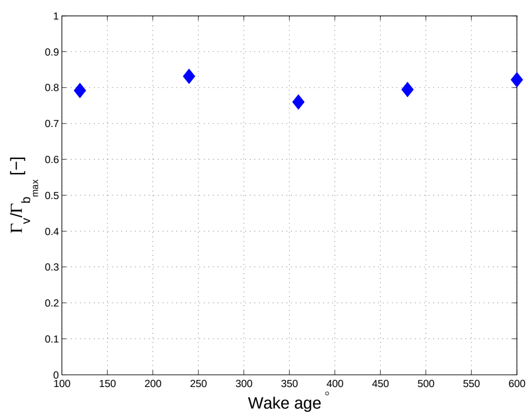

Figure 5-18: Ratio of Measured tip vortex strength Γ with maximum simulated bound vortex strength $\Gamma_{b_{max}}$ as a function of wake age

5-6 Wake rotation

With stereo PIV measurements the velocity vector can be measured in three dimensions, which in this case gives information on the out-of-plane velocity component of the tip vortex as a function of the wake age. The behavior of the third velocity component is described in this section.

5-6-1 Entry angle of the tip vortex

Note that the tip vortex is not intersecting the PIV plane with a normal angle but in entering with a small angle β with respect to the $z-axis$ in the $x-z$ plane. This inclination is caused by the combination of axial and rotational velocity that is experienced by the blade at the tip as it releases the tip vortex. By using simple geometry a simple formula can be derived for this angle.

$$\beta = tan^{-1}\left(\frac{1}{\lambda}\right) \tag{5-1}$$

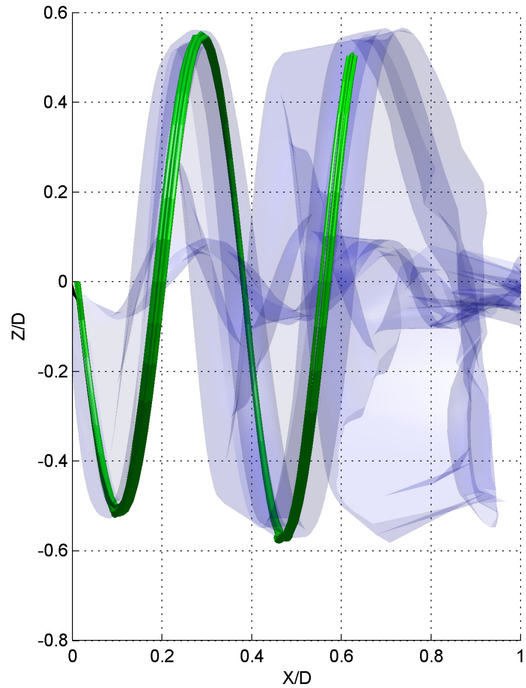

Figure 5-19: Visualization of the tip vortex inclination in $x - z$ plane

In the case of the described PIV measurements, $\lambda = 6.7$, resulting in an inclination of around eight degrees; therefore the tangential velocity of the tip vortex is not perfectly aligned with the horizontal plane but also has a component out of plane. Again simple geometry shows that this value is small compared to the in-plane velocities as $cos(8^\circ) \approx 0.99$. It is therefore not required to correct the velocity fields as presented previously for this small offset.

5-6-2 Measured out of plane velocity

The inclination of the tip vortex is clearly visible in the measured out-of-plane velocity component as depicted in figure 5-20. Depending on the location with respect to the vortex core the maximum out of plane velocity is plus/minus ten percent of the free stream velocity. The position of the vortex core is represented by the black dots in the figure. For $R > R_{core}$ the out-of-plane velocity is positive and for $R < R_{core}$ the velocity is negative. In the region where $R \approx R_{core}$ the velocity is close to zero.

As the wake age increases the difference between positive and negative out-of-plane velocities becomes smaller but remain still clearly visible confirming that the tip vortex stays intact within the first diameter downstream.

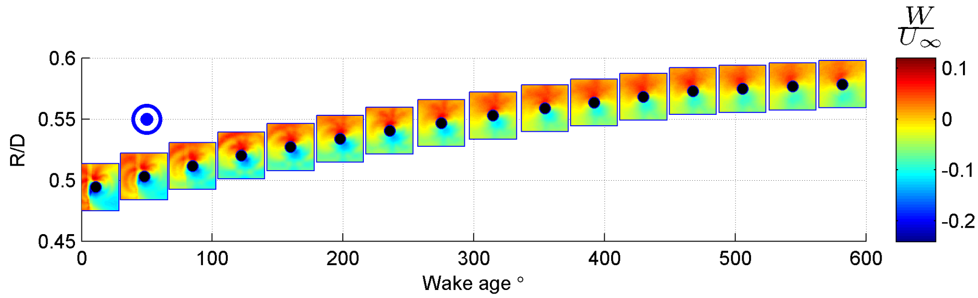

Figure 5-20: Evolution of wake rotation with wake age. Black dots show position of the vortex core. Z coordinate is positively upward

5-7 Validation of vortex core models

The previous analysis in paragraph 5-5-3 shows that the velocity field as produced by the vortex code is not useful for further comparison with the PIV measurements. Note that a viscous vortex core has been added to every vortex filament in the code to remove the singularities and to obtain realistic induced velocities in points very close to the filament. The dimensions of the vortex core are determined by either the core growth model by Lamb-Oseen (LO model) and the solution by Ramasamy and Leishman, (RL model). The default model for the tangential velocity distribution as a function of radial distance is the LO model; the implementation is described in section 4-2-6. A number of PIV measurements capture the tip vortex nicely centered in the measurement plane. These results are used to extract the tangential velocity distribution as a function of radial distance to the vortex core. The measured velocity distribution can be compared with the predictions of both the LO and RL models. Fitting the models through the data can however be done in a number of ways giving either improved or worsened fits.

5-7-1 Data reduction

The following steps are taken to extract the tangential velocity distribution from the PIV measurements:

1. Correct for the downstream travel of the tip vortex by subtracting the mean flow from the total flow. This exposes the tip vortex and swirling motion much more clearly.

2. The position of the vortex core must be known precisely. The position of the vortex core center corresponds to both a local maximum in the vorticity and zero velocity. However, due to strong centrifugal forces the density of seeding particles

is low which complicates the estimate of the vortex core center. The position of the vortex core is estimated both visually and numerically; no significant differences were found in both methods.

3. Determine the maximum radial distance from the vortex core to one of the borders of the PIV plane. If the vortex is centered in the PIV plane, the maximum radius is typically six or seven core radii.

4. Transform the coordinates in the PIV to polar coordinates with the origin at the vortex core center. Also transform the Cartesian velocity components into their equivalent tangential and radial component.

5. Make a scatter plot of all the data points giving a cloud of data points that can be used for fitting the core models.

The raw data as acquired with the previous analysis shows the typical shape of the tangential velocity distribution as known from the LO and RL models (see chapter 3). The scatter is however quite large, which may be caused by the error in vortex core location or subtraction of the mean flow. By using a moving average filter the scatter on the data can be reduced significantly. Such a filter 'moves' along the data and averages the data locally by using a predefined number of surrounding points, also known as the 'span' of the filter. Increasing the filter span reduces the bandwidth but also reduces the number of output data points, furthermore one runs of the risk of averaging the data too much. The following figure shows the influence of the filter on the data, in this case nine neighboring points have been used to average the data. Seeding particles are scarce in the vortex core explaining the scatter in that region. Application of the data filter reduces the data scatter significantly, the remaining interpolated data points clearly reveal the typical tangential velocity profile of a vortex.

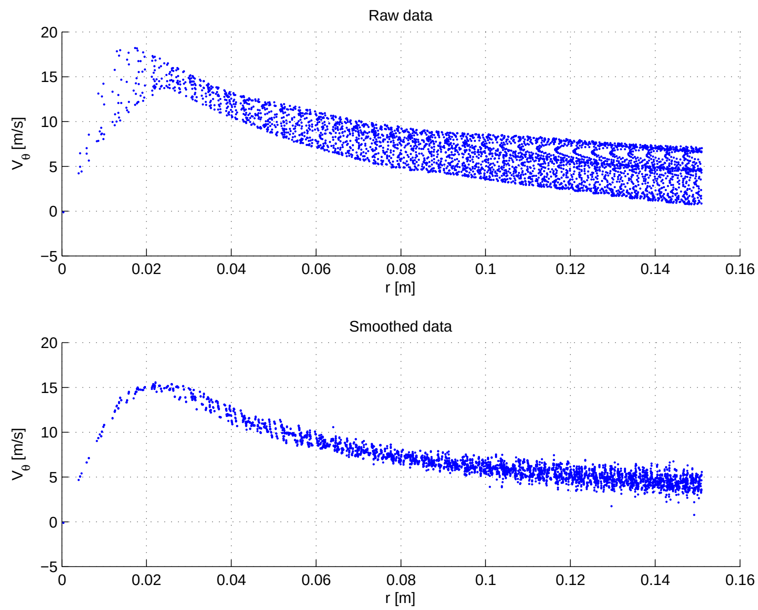

Figure 5-21: Influence of a moving average filter on the data scatter using a filter span of 9.

5-7-2 Tangential velocity distribution

The comparison of the analytical vortex core models can be carried out in many different ways. Recall the equations of the LO and RL models as presented in Chapter 3; both formula's require the circulation strength (Γ) and the core size (r_c) as an input. First and most straightforward is to calculate both parameters from the measurement data and use this information as an input for both the LO and RL models. In order to estimate these parameters, the average velocity profile is calculated. Typically, the location where the tangential velocity attains its maximum corresponds to the core radius. The vortex strength is determined by solving a numerical line integral along a circle centered around the vortex core. Initially the circulation increases rapidly with increasing radius of the circle around the core but as more vorticity is captured the circulation starts increasing asymptotically meaning that almost the entire vortex is captured.

Instead of a manual calculation of the vortex core radius and strength, a curve fitting routine can be used to estimate these parameters. A nonlinear Least-Squares Estimator (LSE) is used which linearizes the models by means of a Taylor expansion and then solves the linearized problem for a number of times until the solution converges below a certain predefined threshold. An initial guess of the best fit solution is required, the quality of this guess may improve the rate of convergence. Applying this method to both the LO and RL model then gives the values of Γ and r_c that give the best fit to the measurement data. One must however be careful when estimating two parameters that are not independent simultaneously. It is highly unlikely that the core radius and the vortex strength are independent and it is therefore recommended to estimate both parameters separately, meaning that either Γ or r_c should be estimated manually.

Remember the formulation by Ramasamy and Leishman of their vortex core model containing six coefficients a_n and b_n that were derived from numerical simulations for Reynolds numbers between $Re_v = 1$ and $Re_v = 1 \cdot 10^6$. Using the LSE it is also possible to allow these coefficients to vary in order to improve the data fit. In this case, it is however required to calculate r_c and Γ manually, otherwise there are too many degrees of freedom in the fitting routine giving bad convergence properties. Values for a_n and b_n are given in [28]; the fitting routine is constrained to look for solutions that are in the same range as the values provided in the table. Furthermore, the curve fit is made in such a way that the sum of coefficients a_n is equal to one as to satisfy the boundary condition that the tangential velocity is zero at the vortex core center.

The quality of the data fit is quantified with the R^2 value, which ranges between zero and one; the closer to one, the better the fit. The values of the fitted coefficients a_n and b_n are presented in Appendix D.

$$R^2 = 1 - \frac{\sum_{i=1}^{N} (f_i - f_{fit_i})^2}{\sum_{i=1}^{N} f_i^2} \tag{5-2}$$

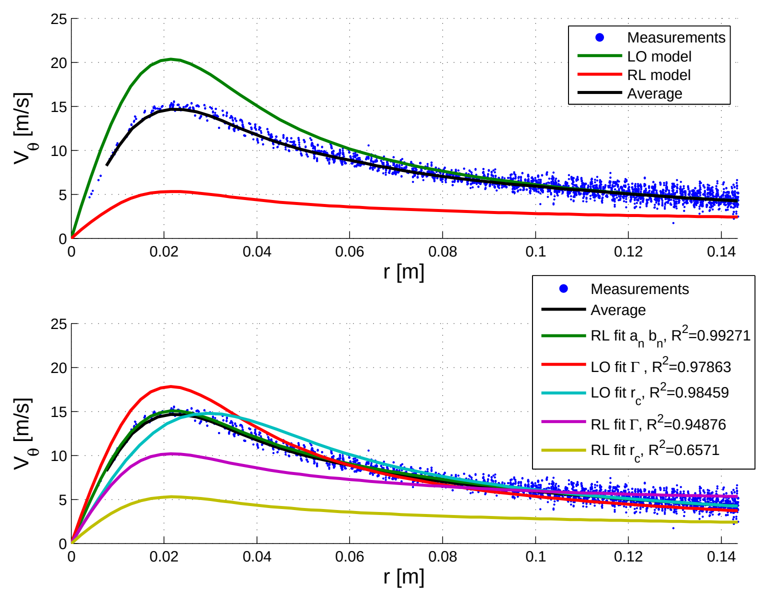

Figure 5-22: Data fitting results at $X/D = 0.13$. Top figure: r_c and Γ are estimated manually from the measurements, bottom figure: r_c and Γ are estimated using non linear LSE.

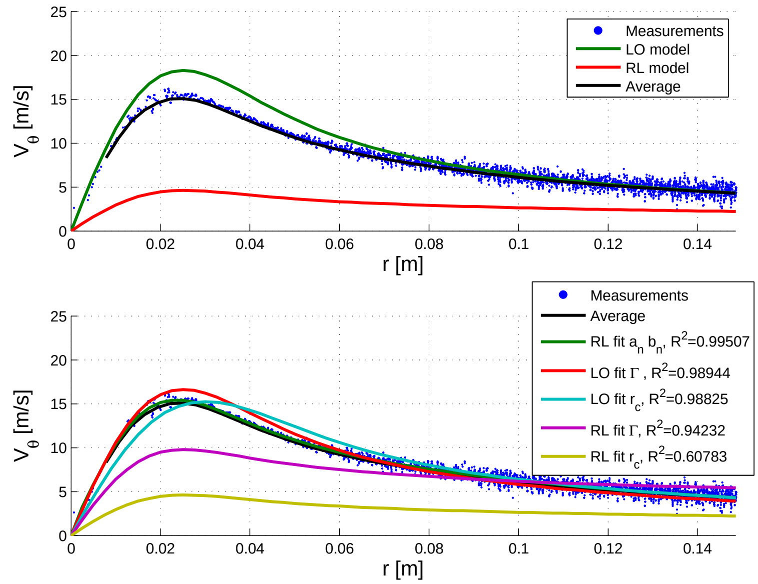

Figure 5-23: Data fitting results at $X/D = 0.253$. Top figure: r_c and Γ are estimated manually from the measurements, bottom figure: r_c and Γ are estimated using non linear LSE.

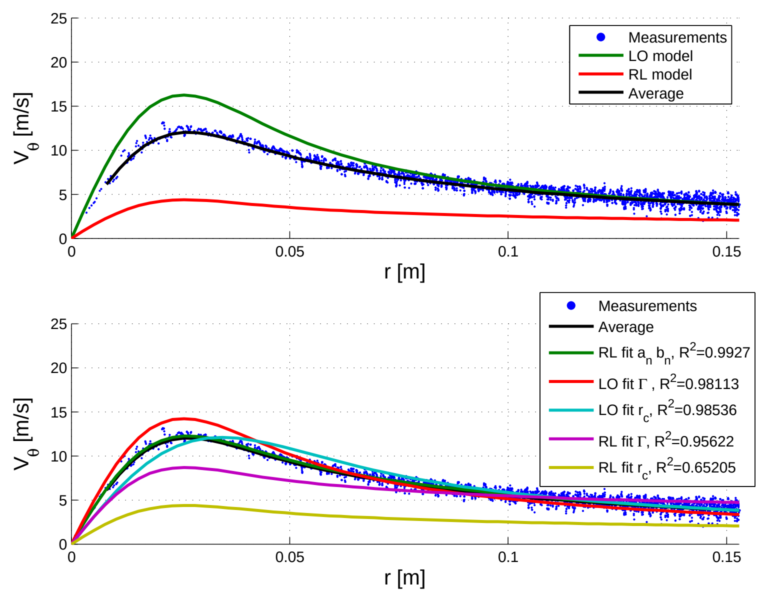

Figure 5-24: Data fitting results at $X/D = 0.38$. Top figure: r_c and Γ are estimated manually from the measurements, bottom figure: r_c and Γ are estimated using non linear LSE.

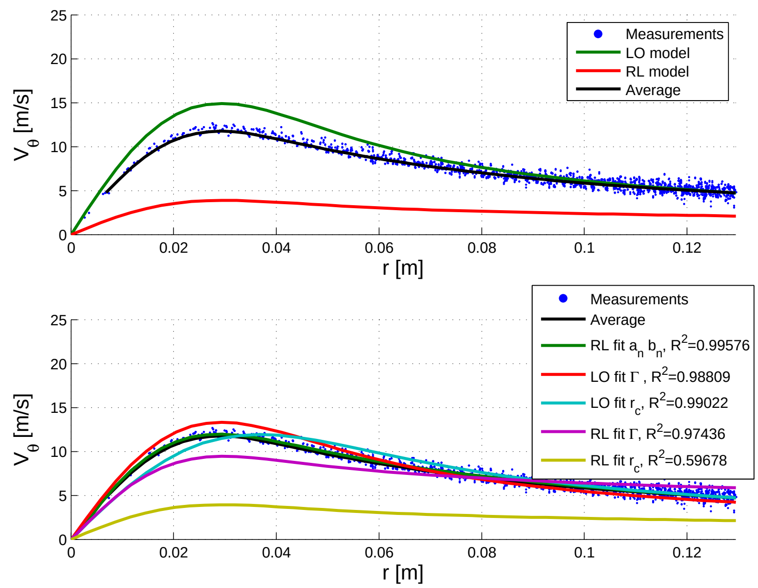

Figure 5-25: Data fitting results at $X/D = 0.501$. Top figure: r_c and Γ are estimated manually from the measurements, bottom figure: r_c and Γ are estimated using non linear LSE.

All results show that the RL model as presented in [28] underestimates the tangential velocity distribution significantly. Indeed, based on the vortex Reynolds number ($Re_v = 5e5$) the velocity profile is expected to be much flatter as also shown by the simulations from Ramasamy and Leishman and figure 3-6. The LO model shows an overestimation of the tangential velocity in the region around the vortex core. This overestimation can be explained by the fact that the measured velocity profile does not exactly decrease asymptotically with $V_\theta \sim 1/r$ as predicted by the LO model. The circulation far away from the core is therefore higher than predicted by the LO model for a given peak swirl velocity.

Allowing the coefficients a_n and b_n to be variables in the fitting procedure combined with a manual calculation of r_c and Γ gives the best fit in all figures. This result makes sense since the LSE has five degrees of freedom in this allowing for a better fit through the data. The values of a_n and b_n are constrained to be in the same range as the initial values by Ramasamy and Leishman but now lose their physical meaning in terms of dependence on the vortex Reynolds number.

5-7-3 Estimation of circulation strength

Also presented in figures 5-22 to 5-22 are the data fits for both the RL and LO models estimating either r_c or Γ. Again here the RL model underestimates the tangential distribution significantly whereas the estimation of the vortex core size is quite similar to the measurements. The LO model shows and overestimation in the core region when estimating Γ and gives a slightly larger core size when estimating the r_c. Differences become even more apparent if the predicted circulation is plotted versus the non-dimensional distance to the core. The LO model attains is maximum circulation after two core radii, this can be explained by the fact that the tangential velocity decreases exactly with $1/r$. The RL fit still shows a strong gradient after six core radii. This is due to the unrealistically high vortex strength that is found by the fitting routine in order to get a reasonable fit. Although not as strong, some measurements also show that there still a slight increase in circulation after six core radii.

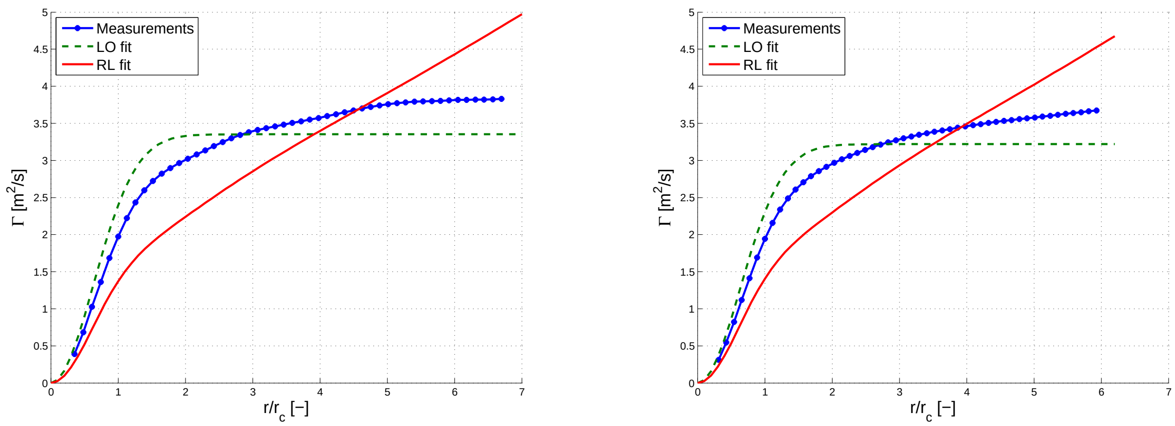

Figure 5-26: Predicted and measured circulation distribution with radial distance from the vortex core at $X/D = 0.13$ (left) and $X/D = 0.38$ (right)

Measurements in the LLF have been performed at very low ambient turbulence intensities, therefore turbulent decay caused by external influences are not noticeable. This also means that the MEXICO measurements are not suitable for tuning the turbulent vortex decay parameters as presented by Han in [12] and in chapter 3. More apparent is the decay in maximum tangential velocity; the measurements and all data fitting routines give similar trends as the wake age increases. This decay is not caused by external ambient turbulence but rather by viscous forces and turbulence from the blade's boundary layer.

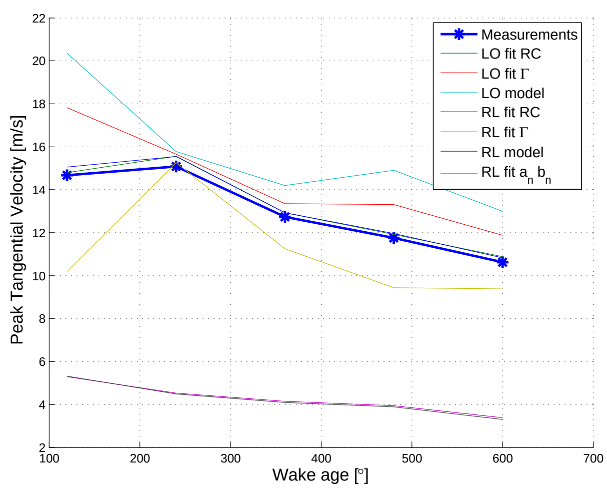

Figure 5-27: Decay of measured and simulated maximum tangential velocity with wake age

5-7-4 Vortex core growth

The decay of a vortex results in the growth of the vortex core. In chapter 3, two models are mentioned that try to capture the size of the vortex core as a function of the wake age. The classical LO model assumes that the growth of the vortex core is completely laminar and is therefore only driven by laminar viscous forces. In this case the typical Reynolds number of the tip vortex is approximately $Re_v = 5 \cdot 10^5$ and therefore one can no longer assume that the flow inside the tip vortex is completely laminar. Ramasamy and Leishman developed a more physical model that describes the size of the vortex core as a function of the wake age and vortex Reynolds number [28].

The diameter of the vortex core is either estimated manually from the measurements or calculated by the fitting routines as described before. Figure 5-28 shows that the manual calculation and RL fit give approximately the same results, whereas the LO fit consistently estimates a radius that is approximately 20% higher. As expected, the figure shows that the core growth according to the laminar LO model is way too low. Addition of the turbulent growth parameter ,$\delta = 50$, gives a much more rapid growth of the vortex core. The value of δ is not fixed and may be used as a tuning parameter to match the measurements to the calculations. In [32] a thorough sensitivity study is performed on the effect of δ on wake expansion and induced velocities in the rotor plane. According to the LO model $r_c \sim \sqrt{\delta t}$, which means that doubling the value of δ will increase the growth rate with a factor of $\sqrt{2}$. Sant used values ranging between $\delta = 1 - 100$ and showed that the effect on wake expansion and induced velocities in the rotor plane is not as significant as on the vortex core growth (see [32]).

The RL model matches quite well with the measured core growth. Note however that the measured core size does not seem to follow the trend of $r_c \sim \sqrt{t}$ as predicted by both the LO and RL models. Although this behavior is quite unexpected, the number of measurements are too limited to draw any strong conclusions from this plot.

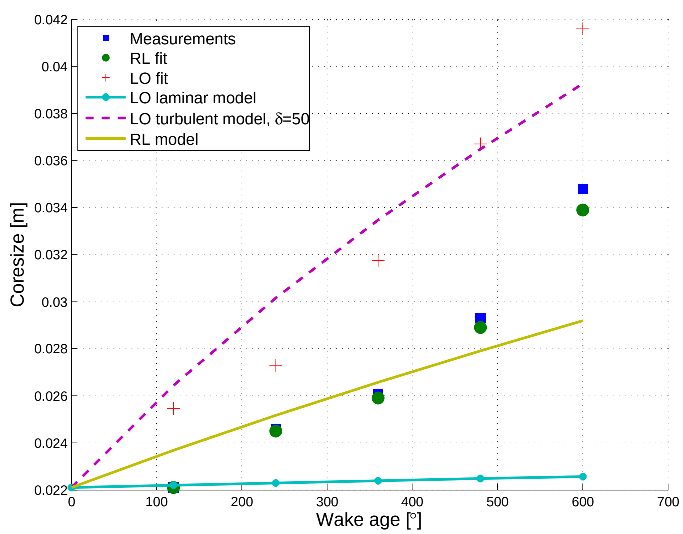

Figure 5-28: Comparison of measured and calculated vortex core growth

Chapter 6

Application of the vortex model on a full scale wind turbine

The previous chapter presented the validation of the vortex code with measurements performed at low ambient turbulence intensities. No measurements are however available that can validate the model in section 3-3-2 which has also been implemented in the vortex code. Instead the first section of this chapter presents a sensitivity analysis on the inputs of the turbulent decay model on the vertical axial velocity deficit profile at various downstream positions in the wake. Secondly attempts are made to include models for the nacelle and blade root of a wind turbine in order obtain a more realistic velocity deficit profile. A model for wind shear is included in the free wake code as well allowing simulation of a turbine in the Earth's atmospheric boundary layer. Finally recommendations are presented for an experiment that could validate the model that describes the vortex decay as a function of ambient turbulence intensity. The Model Experiments In Controlled Conditions (MEXICO) measurements in the previous chapter are performed at very low ambient turbulence levels and therefore not suitable for the validation of the turbulent vortex decay model.

6-1 Sensitivity towards wake decay constant

As mentioned in chapter 3 the decay of vortices is a predominant process in the near wake region. In an attempt to capture the decay in vortex strength a simple vortex decay model has been implemented into the vortex code. The details of this model are discussed in [12] and in chapter 3. The model contains an integration constant c_1 that is from here on referred to as the Vortex Decay Constant (VDC). The value of VDC is not known yet and can be used as a tuning parameter when comparing the model with actual (wind tunnel) measurements.

A first order of this parameter may be found when observing the axial velocity profiles at different downstream positions for a range of different values for VDC. High values of VDC cause a rapid decay of the vortices in the wake which leads to a decrease in velocity deficit. At $1 - 2D$ downstream the presence of the turbine upstream clearly noticeable with velocity deficits in the order of $30 - 50\%$ [29] and [40]. This information can be used to try to find the order of magnitude of the VDC.

6-1-1 Fixed wake simulations

To keep the initial analysis simple and quick it is chosen to use a prescribed wake model for the simulations. In this way the influence of different values on the downstream velocity profile can be quickly assessed. Downside of using a prescribed wake model is however that the roll-up process and the expansion of the wake is no longer included. This means that the location of the vortex filaments and diameter of the wake is not captured correctly. It is therefore important to interpret this analysis as an intermediate step towards a more physical model of the wake. Figure 6-1 shows the resulting velocity profile for different values of VDC and increasing downstream distance. The ambient turbulence (I_∞) is chosen to be 0.15 which is a reasonable value for turbines operating on flat terrain.

Clearly the top two plots show a too rapid decay of the wake since at $2D$ downstream there is almost no velocity deficit anymore. The bottom two figures give more realistic values in terms of velocity deficit. Decreasing VDC even further to for example $1 \cdot 10^{-6}$ results in a almost negligible decay of the wake within the first two rotor diameters downstream. This analysis therefore shows that VDC should be in the range of $1 \cdot 10^{-5} - 1 \cdot 10^{-6}$.

Note that the thrust coefficient on the rotor is quite low compared to the typical value of $0.8 - 0.9$ for wind turbines that operate at optimal C_p. This low value is due to an incorrect setting in the pitch angle of the blade which was discovered after all simulations were finished. A correct pitch setting and higher corresponding C_t will yield a larger velocity deficit i.e. a deeper axial velocity profile.

Ideally the VDC should be estimated from measurements with a well known turbulent inflow conditions. The MEXICO measurements are not suitable in this case since these measurements were performed at very low turbulence intensities hence there is no significant turbulent decay of the vortex wake.

It must be noted that the velocity profile near the center of the wake is not at all reminiscent to the shape that typically is found in the wake. For example Sørensen shows that there is a distinct minimum in the velocity deficit in the near wake region due to the high drag forces that occur in the nacelle and root area of the rotor [41]. In this case there is even an increase in the flow velocity in the region near the root caused by the presence of the strong root vortex filaments. The untypical behavior in figure 6-1 can be simply explained by the fact that in the vortex code the blade root and the nacelle are not modeled. Further on in this chapter an attempt to fix this problem is discussed.

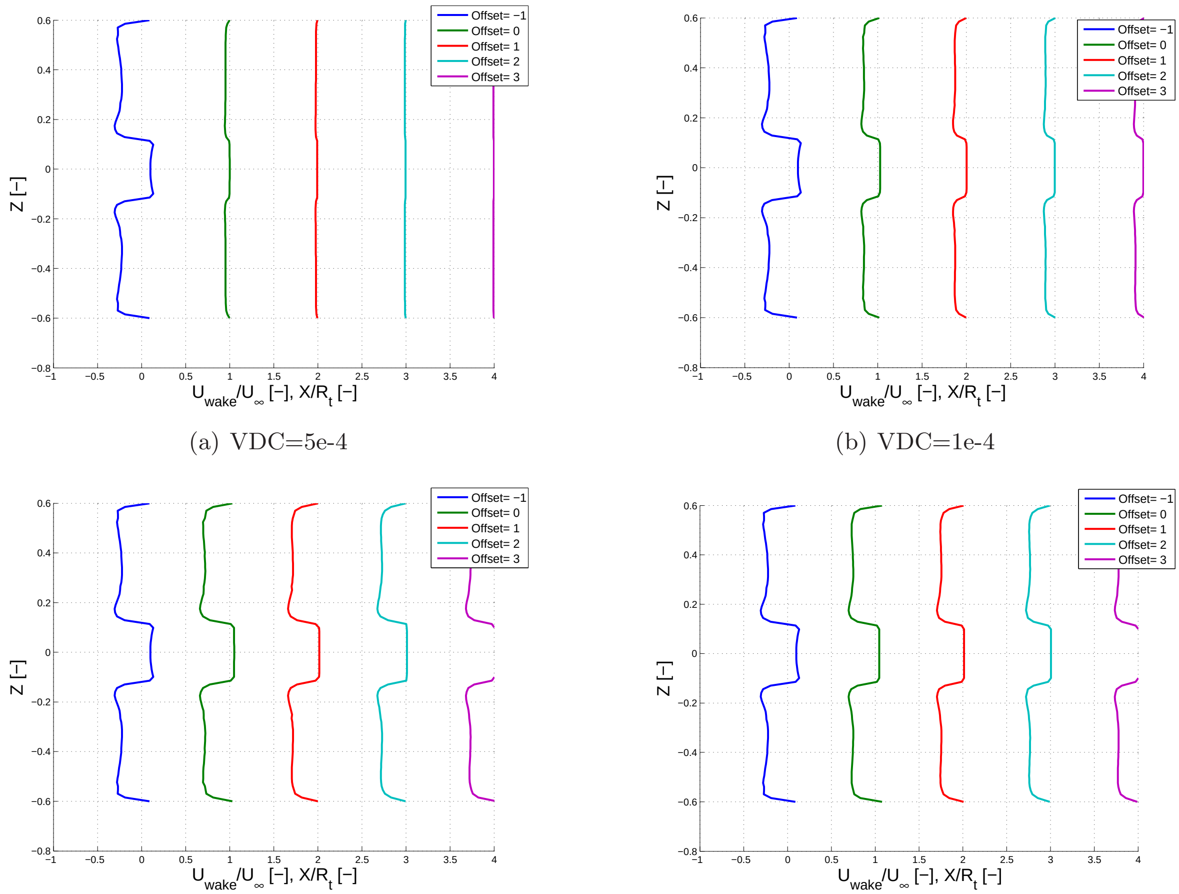

(a) VDC=5e-4

(b) VDC=1e-4

(c) VDC=1e-5

(d) VDC=2e-5

Figure 6-1: Influence of VDC on vertical azimuthal averaged velocity deficit profile $U_w(z)$ with fixed wake, $U_\infty = 12m/s$, $I_\infty = 15\%$, $C_t = 0.59$, turbine: NREL 5MW

6-1-2 Free wake simulations in far wake

The validation studies in the previous sections show that the vortex code is able to capture the expansion of the wake and pitch of the tip vortex quite well within the first diameter downstream. With this in mind a very heavy free wake simulation has been performed extending the wake up to $3.5D$ downstream. The same operating conditions have been used as in the previous section, the only difference is that the wake is now allowed to roll up. Due to the relatively low C_t the wake expansion is not as apparent as in the MEXICO simulation. The resulting velocity profile is quite similar to the profiles obtained with the fixed wake simulations but becomes a little less smooth in the end caused by the accumulated errors from the time integration.

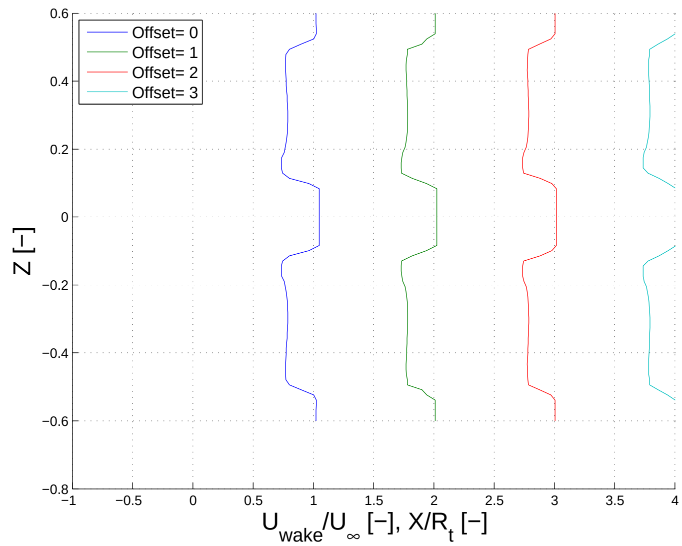

Figure 6-2: Velocity deficit profile for a free wake simulation, $VDC = 1 \cdot 10^{-5}$

The velocity profile obtained by the simulations may be applicable to initialize for example the Ainslie far wake model or other similar Reynolds Averaged Navier-Stokes (RANS) models. These models are typically only valid at distances $\geq 2D$ downstream due to the fact that the streamwise pressure gradient is not taken into consideration.

6-2 Model for the nacelle and blade root

It is challenging to model the influence of the blade root and the nacelle on the lifting surfaces of the blade and the wake. These areas are mainly governed by separated flow and high drag forces and turbulence levels. Inherently a potential flow around any object will give zero pressure drag which is more commonly known as the paradox of D'Alembert. Since the flow phenomena in the vortex code are modeled with vortices an attempt could be made to model the flow around the nacelle by creating an impenetrable object at the wake centerline by means of a series of vortex rings.

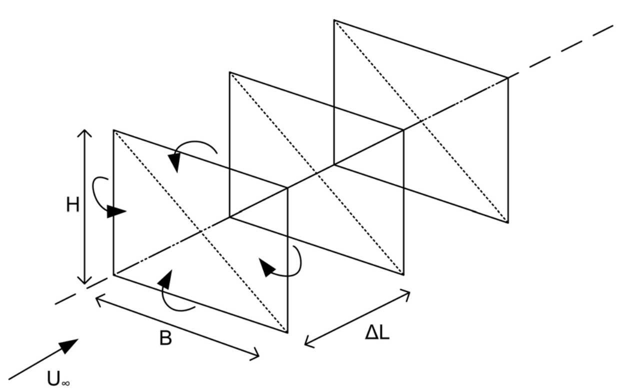

Figure 6-3: Series of vortex rings representing a simple model for the nacelle

6-2-1 Model for the nacelle

The strength of the vortex rings can be calculated by imposing a non-entry boundary condition at the wake center point where normally the hub would be. The net effect of the vortex rings is that the streamlines now follow a path that looks like a rectangular box by changing the dimensions and pitch of the vortex rings the size of the box can be altered(see Figure 6-4). Due to the presence of the vortices the flow is slowed down both up- and downstream of the nacelle and sped up around the nacelle. Due to the fact that the nacelle does not produce any lift, it may be better to model the nacelle with sources instead. However numerical studies have shown that the nacelle is a source of vorticity in the flow which makes the application of vortex rings more acceptable.

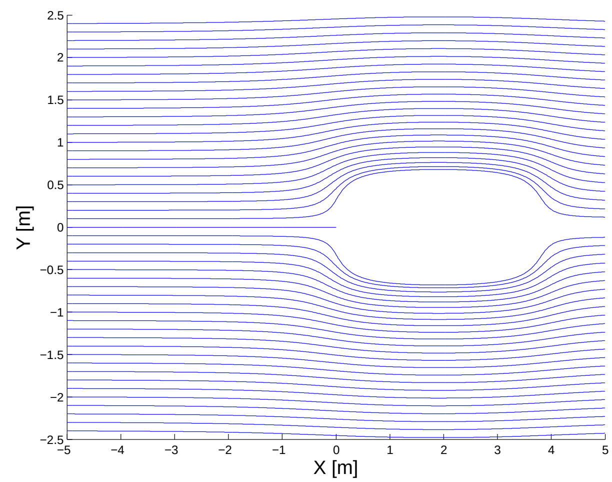

Figure 6-4: Streamlines around nacelle with a size of $1x4m$, $U_\infty = 10m/s$

The model described above is implemented in the vortex code and its influence on the development of the wake is evaluated. Unfortunately, no significant changes in behavior of the wake are noticeable by including this simple nacelle model. The ring vortices from the nacelle are too weak to disturb the induction of the wake onto itself. Especially the root vortex filaments, that cause the roll-up of the wake are strong compared to the ring vortices from the nacelle and are not influenced by the presence of the nacelle. A desired effect of the nacelle would for example be that the root vortex on both sides of the nacelle is dragged towards the wake centerline, which then would close or reduce the size of the gap in the wake.

Apparently the effect of the nacelle on the flow is too local, whereas in reality there is a strong wake behind the nacelle. Therefore it may be better to use more vortex rings and increase the length of the nacelle. In this way the region of reduced flow velocities near the center of the wake is noticeable on a larger scale instead of only locally.

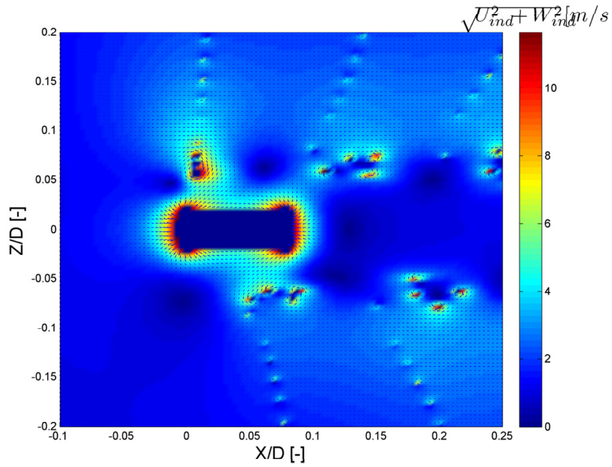

Figure 6-5: Induced velocity field in hub region including a model of the nacelle $U_\infty = 12m/s$. Colors represent the absolute value of the induced velocity

6-2-2 Including a cylindrical root section

In the current model the behavior of the root area is similar to the blade tip, i.e. there is a large gradient in the circulation distribution which causes strong trailing vorticity in the wake. However in most modern wind turbines the lifting surfaces near the root are connected to a cylindrical section of the blade which then connects the blade to the hub. Some designs by turbine manufacturer Enercon have blades where the lifting surfaces are extended towards the hub. Johansen [18] claims that this increases the Annual Energy Production (AEP) by approximately one percent.

Figure 6-6: Difference in hub design of Enercon and GE turbines

In an attempt to get a more realistic root vortex it is assumed that there is a smooth transition between the lifting surface and the cylindrical section the lift and drag properties are then interpolated in a similar way as described in paragraph 4-6. In this way the gradient in circulation distribution near the root may be reduced which results in a weaker root vortex that is shed into the wake. Another possible advantage is that a larger part of the blade and its wake is modeled which reduces the size of the gap in the axial velocity profile as depicted in figure 6-1. The following table gives an overview of the adaptations that have been made to the blade of the NREL 5MW turbine, see Appendix B.

Table 6-1: Blade adaptations

Parameter	Old	New	Unit
R_b	52.2	56.7	m
R_r	10.8	6.3	m
R_t	63	63	m

In order quantify the effect of this blade adaptation the flow field around the hub is plotted in the vertical XZ-plane. The colors in the plot correspond to the level of vorticity in the flow. Clearly the vertical distance between the root vortices has been reduced as an effect of the blade extension. The strength of the root vortex is however not significantly reduced, which may be due to the fact that the blade experiences high angles of attack near the root.

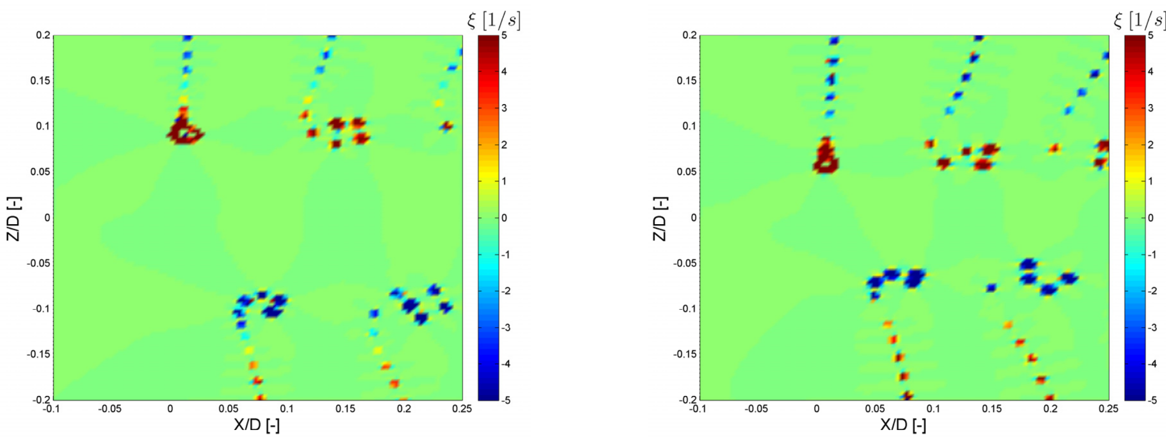

Figure 6-7: Vorticity field around old (left) and adapted (right) blade. Colors represent the level of vorticity ξ.

Observing the bound circulation distribution, Figure 6-8 also shows that there is no significant difference in gradient in the distribution near the root, i.e. differences in trailing vorticity will be small.

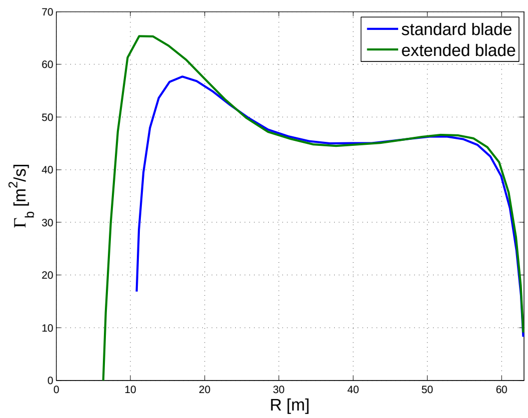

Figure 6-8: Differences in bound circulation distribution for standard and adapted blade

6-3 Implementation of a wind shear model

The vortex code as described in the previous chapter assumes that the rotor experiences a uniform and steady free stream velocity. Winds on a real site are however typically unsteady and vary with the altitude. The variation of wind speed with altitude is often referred to as wind shear. This effect has become very important for the current multi-megawatt wind turbines with hub heights and rotor diameters exceeding one hundred meters. In a free wake vortex code it is quite simple to include a wind shear model making the inflow conditions somewhat more realistic.

Wind turbines typically operate within the Earth's atmospheric boundary layer which can be described with the following logarithmic equation, where κ is the Von Karman constant and z_0 the roughness length. Appendix C gives a table of common values for the roughness length depending on the site conditions.

$$U(z) = \frac{u_*}{\kappa} ln\left(\frac{z}{z_0}\right) \tag{6-1}$$

The parameter u_* is the friction velocity which is commonly defined as the ratio between shear stress at the surface τ_w and the air density.

$$u_* = \frac{\tau_w}{\rho} \tag{6-2}$$

Both the friction velocity and the roughness lengths can be estimated from met mast measurements by applying linear regression on equation 6-3 on a semilogarithmic scale. The slope of this graph is κ/u_* and from a graph of experimental data u_* and z_0 can be calculated.

$$ln(z) = \frac{k}{u_*} u(z) + ln(z_0) \tag{6-3}$$

In the European Wind Turbine Standards II (EWTS), it is however recommended to model the wind shear with the power law, which obeys the following expression, where m represents the shear exponent. Taking the logarithm of this expression gives a linear equation which can be used to find the value of m from wind measurements at different altitudes.

$$U(z) = U_0 \left(\frac{z}{z_0}\right)^m \tag{6-4}$$

In Appendix C typical values for shear exponent m are presented in a table that are used in Wind Resource Assessment (WRA) software like WindPRO.

The power law has been implemented in the vortex code. It must be noted that mathematically it is not allowed to use a non-linear shear in potential flow field since this violates the assumption that the flow is irrotational. However this assumption is already violated when using either the RL or LO vortex core models as described in chapter 3.

The blade now moves through a wind field that changes with the azimuthal position of the blade, this means that the blade circulation changes continuously and therefore there is also a continuous shedding of vorticity in the wake. From a physical perspective this shedding of vorticity may be interpreted as an increase in the unsteadiness of the wake that occurs due to the presence of the wind shear gradient. Note that generation of turbulence by the presence of a shear layer is a viscous process that cannot be captured by the vortex code. A blade that moves upward experiences an increase in circulation, applying Kelvin's theorem gives negative shed vorticity in the wake. Similarly a downward moving blade gives positive shed vorticity in the wake. This behavior is clearly visible in Figure 6-9 where the wake is plotted for two different values for the shear exponent.

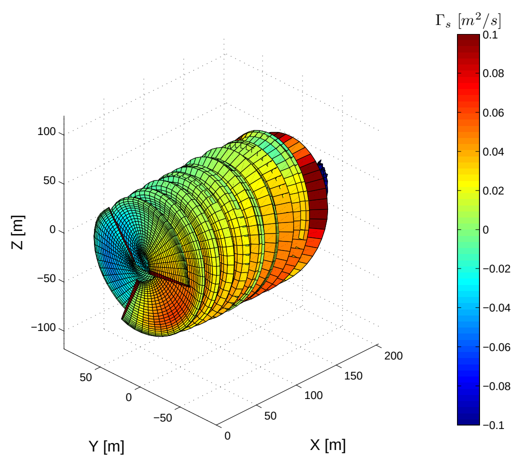

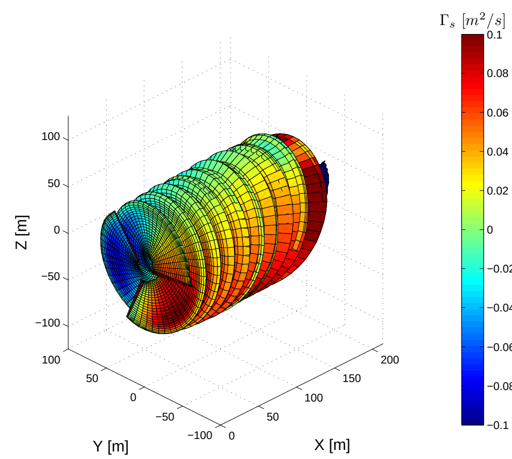

Figure 6-9: Effect of shear on the wake, left: $m = 0.15$, right: $m = 0.25$. Colors represent the level of shed vortex strengths Γ_s in the wake

Secondly in sheared flow the bottom half of the wake will travel downstream more slowly than the top half caused by the difference in local convection speed.

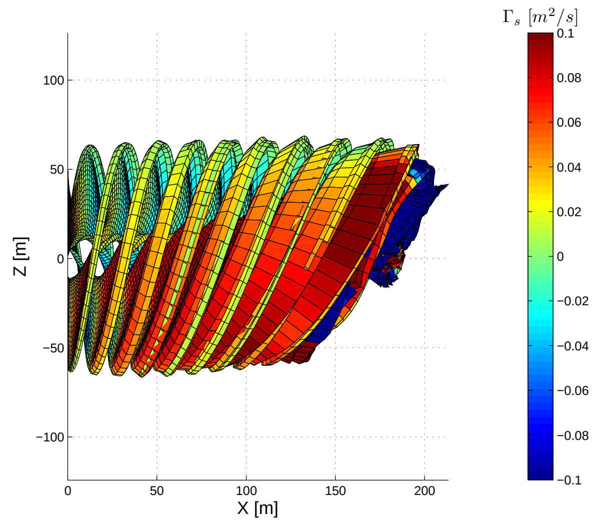

Figure 6-10: Effect of shear on downstream convection of the wake, $m = 0.25$, Colors represent the level of shed vortex strengths Γ_s in the wake

Potentially this model can give valuable information on the loads that occur due to the continuously changing wind speed that is experienced by the rotating blades. A blade that is moving upward will increase its circulation and therefore its contribution to the thrust and torque will increase as well. In particular it is expected that blade root bending moments are significantly influenced by the shear as an increase in circulation on the outboard part of the blade will give a relatively strong increase in bending moment at the hub. The following figure shows the relative influence of the sheared flow on the bound circulation of a blade that starts at lower tip height. Relative changes in bound vortex strength are in the order of 5% for a shear exponent of $m = 0.25$. It is recommended and interesting to make similar figures for torque, thrust and flapping moments. Possibly this could contribute to the improvement of Blade Element Method (BEM) models by deriving simple correction factors from free wake simulations. In [32] such correction factors are derived for yawed flow using also a free wake model.

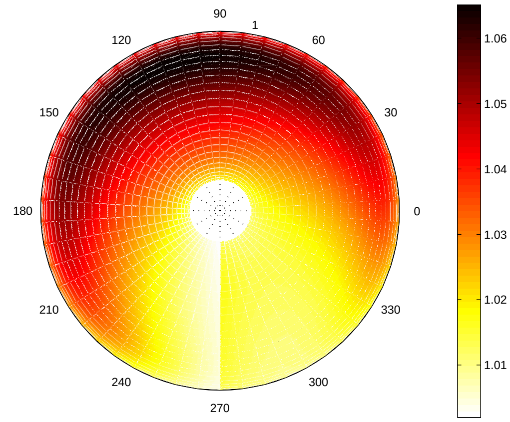

Figure 6-11: Effect of shear on bound circulation distribution during a full rotation starting at lower tip height ($\phi = 270°$), $m = 0.25$, Colors represent the relative bound circulation strength with respect to the value at $\phi = 270°$, simulation settings: $N_{rev} = 5$, $N_\phi = 50$, $N_b = 30$

Note that there is a jump from light to darker yellow at 270°, meaning that the bound vortex has not exactly returned to its initial value after one rotation. Compared to the changes in bound vortex strength during the revolution this jump is relatively large. Five revolutions were used, more revolutions are required to ensure perfectly periodic behavior of the bound vortex strength.

The bottom half of the wake travels downstream more slowly hence the tip vortices remain closer to each other. For that reason it is expected that the axial velocity deficit for that part of the wake will be higher. Figure 6-12 indeed shows this behavior, differences in velocity deficit between upper and lower half of the wake are in the order of 5%. More detailed analysis and longer simulations of the shear model are recommended before any strong conclusions can be drawn about the effect of wind shear on the rotor loads and wind speed deficit profile.

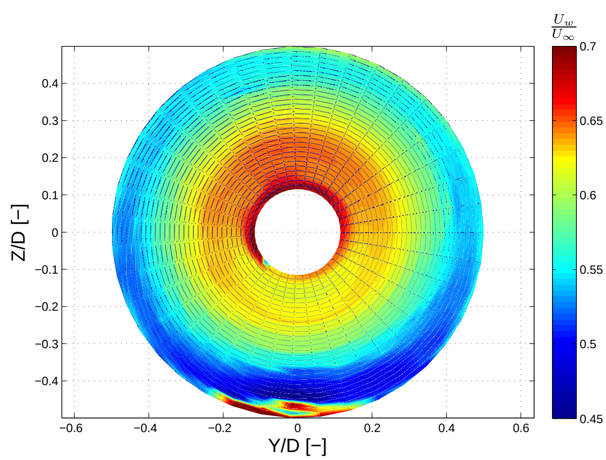

Figure 6-12: Effect of shear on axial velocity deficit at $0.5D$ downstream in the wake, $m = 0.25$, simulation settings: $N_{rev} = 5$, $N_\phi = 50$, $N_b = 30$

6-4 Recommendations for an experiment

During this thesis there have been no suitable measurement data available that could be used to validate the turbulent vortex decay models as described before. The measurements from Sant and Haans were limited to a distance of $0.1D$ downstream; during the MEXICO project no measurements have been performed on the development of the velocity deficit profile as function of downstream position. Moreover the turbulence levels inside the Large Low-speed Facility (LLF) were too low compared to the levels that a wind turbine in the field typically experiences.

6-4-1 Field measurements

A lot of measurement data is available from ECN's test site in Wieringermeer; the layout of the site is depicted below. For example one could for example measure the deficit in power that occurs between two turbines for wind directions in which one or the latter experiences a wake. The power deficit could than be translated into a single value for the velocity deficit at hub height. Only limited information can be extracted from these measurements as no real velocity profile is obtained. Wind turbines in wind farms are typically separated by $3D - 6D$ which is too large for a validation study of the vortex decay models as these will no longer be valid at such large distances downstream.

Alternatively one could measure the velocity deficit profile experienced by a met mast in the wake of an upstream turbine, this would however require the presence of an additional met mast that measures the inflow conditions of the turbine. At the site of Wieringermeer there is no opportunity to perform such measurements. More flexibility could be achieved by placing a Light Imaging Detection And Ranging (LIDAR) system on the site that can be easily moved around such that both the up-and downstream flow conditions can be captured. Downside of using field measurements is that the wind is never continuously from the same direction; yaw errors should therefore be taken into account. Secondly it is unlikely that the tip vortex will be visible in the field measurements, a metmast or LIDAR is not able to measure such a flow structure in detail. Comparison of the measured and simulated axial velocity deficit profiles seems to be the most plausible way of validating the model against field measurements.

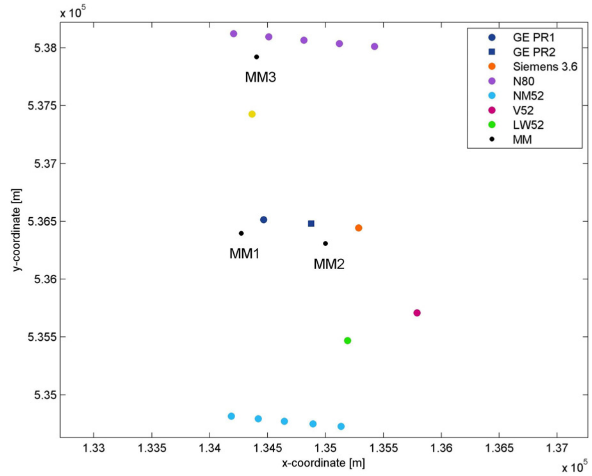

Figure 6-13: Layout of test site at Wieringermeer, *source: [29]*

6-4-2 Measurements in Open Jet Facility (OJF)

Field measurements will always remain very important for the assessment of wind turbine interaction in wind farms. A major disadvantage is however that one cannot control the input conditions making it difficult to isolate the effects of certain parameters. In a wind tunnel it is possible to change for example the incoming wind speed or the yaw angle of the rotor. Recently a new OJF has been opened at the faculty of Aerospace Engineering in Delft. This facility is similar to the LLF from Duits Nederlandse Windtunnels (DNW) and therefore very useful for research on wind turbine aerodynamics.

Table 6-2: Specifications of the OJF,*source:[1]*

Parameter	Value	Unit
Wind speed	30	m/s
Jet area	9	m^2 (constant)
Test section	6x6.5x13.5	m
Typical rotor diameter	1.8	m

The main source of turbulence inside a wind tunnel is the propeller that drives the flow, more turbulence can be created by the wall and the shedding of vortices from the model. For that reason a number of countermeasures are taken to remove the turbulence from the flow and obtain a nice steady jet inside the test section. Corner vanes ease the flow around corners preventing the formation of strong flow stagnation in the tunnel. Vortices are broken down by a series of meshes with increasing fineness. After passing through the turbulence meshes the flow enters the settling chamber were it slows down and expands reducing the turbulence even further, then the flow is contracted through a nozzle and enters the test section. This cascade of countermeasures allows for measuring at turbulence levels at less than one percent.

If an experiment requires an increased level of turbulence inside the test section, for example when examining the effect if turbulence on vortex decay, a turbulence grid can be placed at the jet exit the destabilizes the laminar flow from the nozzle. The laminar flow passes through a grid of small rods which cause instable shear layers leading to turbulent flow downstream of the grid. Depending on the resolution of the grid the level of turbulence and length-scales can be controlled. Sufficiently far away from the grid the turbulence has mixed completely and is therefore isotropic. Additional turbulence can for example be generated by placing a number of cylinders in the nozzle exit that will shed vorticity in the flow. It is not likely however that the turbulence inside the test section has the same time- and length scales and frequencies as occurs in real wind fields. Scaling the small-scale turbulence in the wind tunnel in attempt to predict the behavior of full-size turbines may therefore by quite challenging.

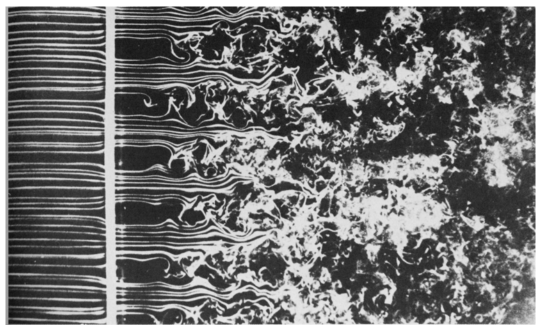

Figure 6-14: Generation of turbulence with a grid, *Source:[15]*

A lot of understanding can already be derived from the Particle Image Velocimetry (PIV) data from the MEXICO on the formation and decay of the tip vortex in low turbulent conditions. The next step is understanding how ambient turbulence influences the tip vortex as it may be expected that the turbulence will "eat" the circulation giving a quicker decay. Additionally it is desirable to measure the vertical velocity profile as a function of downstream distance; this will increase the understanding of the formation of the far wake from the near wake. Based on the experience gained from the MEXICO project it is recommended to perform the following measurement campaign in the OJF.

- The presence of the turbulence grid introduces disturbances in the flow hence a higher level of turbulence. The inflow conditions of the rotor should therefore be known accurately. Therefore the first step should be an extensive measurement of the upstream flow conditions validating that the wind field is indeed isotropic. Moreover the influence of the rotor on the upstream wind speed and turbulence intensity has to be verified.

- The level of turbulence intensity depends on the resolution of the turbulence grid and on dimensions and shape of any other disturbance objects that can be placed at the nozzle exit. Typically wind turbines operate at turbulence intensities ranging between 5% and 20% depending on the roughness of the terrain. It is recommended to perform the measurements at similar turbulence levels.

- Similar PIV measurements can be performed in the OJF tracking the evolution of the tip vortex as it moves downstream. Information on the persistence of the tip vortex can be obtained as a function of different turbulence intensities. As a baseline perform the measurements in clean tunnel conditions, i.e. no added turbulence.

- Measure the axial vertical velocity profile with a hot-wire at distances between $0.5D$ and $3D$ downstream with steps of $0.5D$ for different values of the ambient turbulence. Measure both the Phase Locked Average (PLA) profile and the azimuthal averaged profile; as the vortex wake decays the difference between the two profiles should become less significant.

- The forces on the blades will continuously change as a consequence of the turbulence in the test section, possibly influencing the strength of the tip vortex. This effect should be taken into when interpreting the results.

Chapter 7

Conclusions and Recommendations

7-1 Conclusions

The development of the near wake downstream of a wind turbine is a complex process involving both viscous and turbulent mixing effects. Especially evaluating the dynamics of the wake in a turbulent atmosphere is difficult and still much remains unknown on the exact processes that play a role.

7-1-1 Conclusions chapter four

A free wake lifting line has been developed successfully and has been extended with models that capture both the viscous and turbulent decay of the vorticity in the wake. In this way viscous and turbulent mixing effects are implicitly modeled in the potential flow code.

Free wake simulations are computational intensive especially for multi bladed machines. The computation time can be reduced by implementing a parallel computation of the induction of the wake onto itself. Such a routine has been developed but has not been tested thoroughly. In theory a coarser grid can be applied when using a second order time integration scheme like the predictor/corrector method. On the other hand this requires two velocity field evaluations per time step reducing its computational efficiency. Further verification of the scheme is required.

The code compared well with the predictions from another fixed wake code developed by GE Wind Energy. Reproduction of the elliptic lift distribution of corresponding to a wing with an elliptical planform gave promising results.

7-1-2 Conclusions chapter five

The lifting line code proves to be a valuable tool to obtain a first order estimate of the near wake within the first diameter downstream of the rotor. In the rotor region the predictions of axial induced velocities by the code matched very well with the hot-film measurements. Further downstream the vortex code proved its ability to capture the expansion of the wake and pitch of the tip vortex. The roll up of the vortex sheet is captured as well but comparing the Particle Image Velocimetry (PIV) images with the simulated flow field showed significant differences. In reality the tip vortex is a single discrete vortex whereas the code mimics the tip vortex with a number of discrete vortex filaments. Simulations with a smaller time step improved the roll up a bit but in general a first order time integration method is not suitable for capturing the roll up of the wake accurately.

An accurate fit through the measured tangential velocity profiles of the tip vortices is obtained when coefficients a_n and b_n of the RL model are allowed to vary freely within the limits specified in [28]. The physical validity of the model is however lost in this way since the coefficients represent the dependence of the velocity profile on the vortex Reynolds number. The Classical RL model underestimates the velocity profile whereas the LO model tends to overestimate the peak velocity near the core.

The tip vortex remained clearly visible in the PIV measurements up to $0.8D$ downstream of the rotor. The decay of vorticity with wake age is mainly governed by viscous forces in this case as the ambient turbulence in the Large Low-speed Facility (LLF) was less than one percent. The diameter of the vortex core increased with wake age although no strong conclusions can be drawn from the comparison between the measured and calculated core growth.

7-1-3 Conclusions chapter six

Depending on the value of the Vortex Decay Constant (VDC) the rate of turbulent decay of the vortex wake and the vertical axial velocity deficit profile can be influenced. Previous work has shown that there is s strong decay in vortex strength within the first two diameters of the wake, but no suitable measurements were available to examine this phenomenon thoroughly. No conclusion can therefore be drawn yet on the ability of the model to predict turbulent and viscous decay of the near wake accurately. In the future after a more thorough validation study the model may be applicable to initialize for example the Ainslie far wake model or other similar models that are based on the Reynolds Averaged Navier-Stokes (RANS) equations.

Models for the nacelle and blade root have been added in order to obtain a more realistic model of the wake centerline. The nacelle and blade root models are however not able to capture the wake centerline properly, in reality high drag forces play a predominant part in the development of that part of the wake making it difficult to implement this in a lifting line code.

The free wake model can quite easily deal with wind shear which is a source of cyclic loads on the blades due to the continuously changing wind speed. This may in the future help to improve understanding the effect of shear on fatigue loads.

It is unlikely that the vortex code will be able to capture the physics of the wake at distances greater than $2D$ downstream as then the wake does not posses the typical vortex structure anymore. The Model Experiments In Controlled Conditions (MEXICO) measurements show that the vortex wake remains in existence within the first diameter downstream at low turbulence levels. The vortex code will not be able to predict the breakdown of large scale vortices into sub-scale eddies and has only potential validity in regions where the vortex structure of the wake is still existing.

7-2 Recommendations for future research

The computational speed of the lifting line code can be reduced significantly by using a parallelized computation of the Biot-Savart law during each time step. It is therefore recommended to improve the already existing parallel computation routine and use it on a multi-core workstation or on a cluster of computers. In terms of programming the speed of the code can be improved by eliminating elements that are far away from each other and have negligible influence. The explicit Euler time marching solution is slightly better than a first order solution; a second order scheme would allow for a coarser grid increasing the computational efficiency.

Although the position of the tip vortex is predicted quite well by the vortex code the resulting flow field differs a lot from the measured field. It may be desirable to apply a higher order method locally to capture the roll up of the vortex sheet in greater detail. For instance the predictor/corrector or Adams-Bashforth methods can be applied here. Parallelized computation allows for a simulation on a very fine mesh which may improve the results as well; for a single CPU the computational effort will be too great in that case. Initial steps cowards higher order schemes and parallel computation are presented in chapter 4.

The development of a simple model of the velocity deficit at the wake centerline and root region was unsuccessful. For future models it may be better to use empirical estimates of the wake behind such bluff bodies as they are difficult to simulate.

As an alternative to the simple decay models as implemented in the vortex code it is recommended to couple the lifting line code to a $3D$ RANS solver. The output of the lifting line code at for example $0.5D$ to $1D$ downstream can be used as an input for the RANS algorithm. This model would capture more of the physics of the wake but may also overestimate the decay of vorticity due to numerical diffusion [8].

To examine the effect of ambient turbulence on vortex decay it is useful to perform a wind tunnel experiment in the Open Jet Facility (OJF) measuring both the evolution of the tip vortex and the (axial) velocity profile in the wake at increasing downstream positions. Research has to be carried out on how to create artificial turbulence in the tunnel that can somehow be compared to atmospheric conditions. Possibly knowledge about roughness effects in boundary layer tunnels can be applied here.

Bibliography

[1] http://www.lr.tudelft.nl/live/pagina.jsp?id=78a106ae-0553-4af5-b68f-e7e1d7f12e0e&lang=en. visited 07-05-2009.

[2] EMD International A/S. Windpro/park introduction to wind turbine wake modelling and wake generated turbulence. 2005.

[3] K.R. Dixon B.A.Sc. The near wake structure of a vertical axis wind turbine. *Master of Science Thesis*, April 2008.

[4] F. Vermolen J. van Kan C. Vuik, P. van Beek. Numerieke methoden voor differentiaalvergelijkingen. *Delft University of Technology*, 2004.

[5] J.F. Corbett. J.f. corbett, the new wasp flow model: a fast,linearized mixed spectral-integration model applicable to complex terrain. In *European Wind Energy Conference (EWEC) 2007*, 2007.

[6] A. Crespo. Numerical analysis of wind turbine wakes. In *Delphi workshop*, 1985.

[7] M. Van Dyke. *An Album of Fluid Motion*. 1982.

[8] ECN. Model experiments in controlled conditions. *Final report*, February 2007.

[9] S. Frandsen, R. Barthelmie, S. Pryor, O. Rathmann, S. Larsen, and J. Hjstrup. Analytical modelling of wind speed deficit in large offshore wind farms. *Wind Energy*, 9, 2006.

[10] G.C. Greene. An approximate model of vortex decay in the atmosphere. *Journal of Aircraft*, 23, July 1986.

[11] W. Haans. Hawt near-wake aerodynamics part 1: Axial flow conditions. *Wind Energy*, 11, 2008.

[12] J. Han. Numerical study of wake vortex decay and descent in homogeneous atmospheric turbulence. *AIAA Journal*, 38, April 2000.

[13] F. Holzäpfel. The turbulent decay of trailing vortex pairs in stably stratified environments. *Aerospace Science and Technology*, 5, 2001.

[14] F. Holzäpfel. Analysis of wake vortex decay mechanisms in the atmosphere. *Aerospace Science and Technology*, 7, 2003.

[15] J. Scott J. Mathieu. *An introduction to turbulent flow*. Cambridge University Press, 2000.

[16] N.O. Jensen. A note on wind generator interaction. *Ris National Laboratory*, 1983.

[17] A. Jimenez. Advances in large-eddy simulation of a wind turbine wake. *Journal of Physics*, 75, 2007.

[18] J. Johansen. Numerical investigation of a wind turbine rotor with an aerodynamically redesigned hub-region. In *EWEC 2006*, 2006.

[19] J.D. Anderson Jr. *Fundamentals of Aerodynamics*. McGraw-Hill Higher Education, 2001.

[20] A. El. Kasmi and C. Masson. An extended $k-\epsilon$ model for turbulent flows through horizontal-axis wind turbines. *Journal of Wind Energy and Industrial Aerodynamics*, 96, March 2007.

[21] J. Katz and A. Plotkin. *Low-Speed Aerodynamics*. Cambridge University Press, 2001.

[22] P.K. Kundu and I.M. Cohen. *Fluid Mechanics*. Elsevier Academic Press, 2004.

[23] G.C. Larsen. A simple wake calculation procedure. *Technical Report Ris-M-2760*, December 1988.

[24] J.G. Leishman. *Principles of Helicopter Aerodynamics*. Cambridge University Press, Cambridge, 2006.

[25] R. Mikkelsen. *Actuator Disc Methods Applied to Wind Turbines*. Doctoral dissertation, 1995.

[26] M. Ramasamy. *Contributions to the Measurement and Analysis of Helicopter Blade Tip Vortices*. Doctoral dissertation, 2004.

[27] M. Ramasamy and J. Leishman. A generalized model for transitional blade tip vortices. *Journal of the American Helicopter Society*, 51:92–103, January 2006.

[28] M. Ramasamy and J. Leishman. Reynolds number-based blade tip vortex model. *Journal of the American Helicopter Society*, July 2007.

[29] D.J. Renkema. Validation of windpro wake models and the development of a new model for wind farm optimization. *Master of Science thesis, GE confidential*, June 2007.

[30] S. Ross. *Natural hazards*. Nelson Thornes, 1998.

[31] P.G. Saffman. *Vortex Dynamics*. Cambridge University Press, 1992.

[32] T. Sant. *Improving BEM-based Aerodynamic Models in Wind Turbine Design Codes*. Doctoral dissertation, Delft, 2007.

[33] F. Scarano. Experimental methods in aerodynamics lecture notes. *Delft University of Technology*, 2007.

[34] J.G. Schepers. Endow: Validation and improvement of ecn's wake model. *ECN report*, 2003.

[35] J.G. Schepers. Wakefarm aerodynamics. *Lecture at Delft University of Technology*, June 2007.

[36] J.N. Sorensen. Model for unsteady rotor aerodynamics. *Journal of Wind Energy and Industrial Aerodynamics*, 1995.

[37] H.B. Squire. The growth of a vortex in turbulent flow. *Aeronotical Quarterly*, 16, Summer 1965.

[38] N. Troldborg, J.N. Srensen, and R. Mikkelsen. Numerical simulations of wakes of wind turbines in wind farms. 2006.

[39] A. van Garrel. Development of a wind turbine aerodynamics simulation module. *ECN report*, August 2003.

[40] L. Vermeer. How strong is a tip vortex? In *Proceedings 17th BWEA Conference*, 1995.

[41] L.J. Vermeer, J.N. Srensen, and A. Crespo. Wind turbine wake aerodynamics. *Elsevier*, 2003.

[42] S.G. Voutsinas, K.G. Rados, and A. Zervos. Investigation of the effect of the initial velocity profile on the wake development of a wind turbine. *Journal of Wind Energy and Industrial Aerodynamics*, 39, 1992.

[43] S.G. Voutsinas, K.G. Rados, and A. Zervos. On the effect of rotor geometry on the formation and the development of its wake. *Journal of Wind Energy and Industrial Aerodynamics*, 39, 1992.

Appendices

Appendix A

Manual of the Code

This appendix gives an overview of the structure of the Free Wake Vortex Code that has been developed as a part of this thesis. It is highly recommended to also read chapter 4 of this thesis since the theoretical background of the the code is discussed there.

Before using the code it is important to understand the various sub functions that are being used during every simulation and in which order calculations follow each other. The following flow chart gives a clear overview of the calculations that are carried out during every time step.

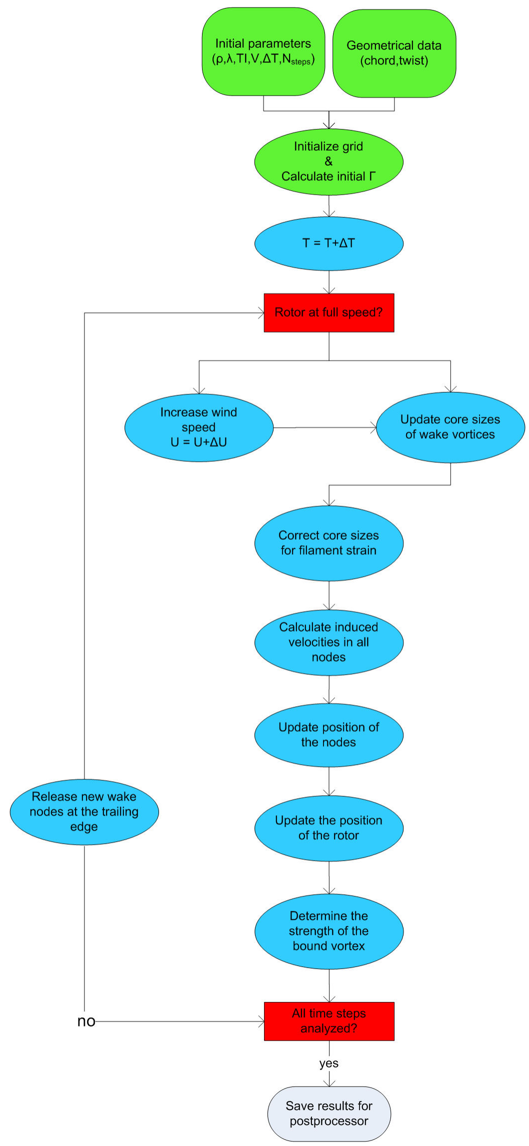

Figure A-1: Succession of calculations of free wake vortex code

A-1 Subroutines

Time_step.m

This is the main routine that is the backbone of the entire code. This file calls all the subroutines in the right order and makes sure the output is stored in the correct structure. Also in this file the initial settings as TSR, N_{ϕ}, N_{rev} etc. Furthermore different options can be chosen for example the core model, vortex filament straining and free or fixed wake.

geometry.m

A function that reads in the geometric data from the required folder and based on that generates the location of trailing and leading edge, control points and collocation points in the local blade coordinate system. In this routine the number of blade nodes N_b and the blade pitch angle ψ_b can also be defined.

airfoil.m

This program reads in the airfoil lift curves that are used along the blades. This information might be used by *AOA_condition.m*.

initial_coresize.m

This function calculates the initial coresize of the vortices that are shed into the wake. The user can chose between a fixed initial core size or a pre-aged vortex model as presented in [28].

coresize_LO.m

This routine updates the core sizes of all vortex filaments according to the Lamb-Oseen vortex growth model. Turbulent decay parameter δ is set to 50.

coresize_LO.m

This routine updates the core sizes of all vortex filaments according to the Ramasamy and Leishmann vortex growth model. A turbulent decay parameter is not necessary for this model.

filament_strain.m

When switched on calculated the effective core sizes based on the straining effect of the vortex filaments. This makes sure that vorticity is not added to the domain.

Turb_decay.m

If switched on this method uses a model for the turbulent decay of both trailing and shed vortices in the domain of computation. It can be sued for the exploration of the near wake as a function of turbulence intensity.

velocity.m

This function calculates the induced velocities of all vortex filaments in the domain on all nodes in the grid. Also it calculates the induced velocities of the wake on the blades. The calculation is based on the Biot-Savart law, hence *velocity.m* calls the routines *Biotsavart_shed.m* for shed filaments and *Biotsavart_trail.m* for trailing filaments. As an alternative *velocity_2.m* can be called which is made suitable for computation on multiple cores. In case a prescribed wake is used *velocity_prescribed.m* is called which skips the calculation of the wake onto itself and only calculates the effect of the wake on the blades.

nodespos.m

Based on the induced velocities in all nodes the position of all nodes in updated for the current time step by means of an Euler implicit model. The first nodes that are shed from the blade are treated differently. They are either located at $c/4$ behind the trailing edge in the direction of the local blade angle or in the direction of the local flow angle. Alternatively the nodes are positioned at 25% fo the wind convected distance.

rotorpos.m

this routines simply shifts the rotor and its attached control points and collocation points by one azimuthal step

non_entry.m

This routine calculates the new value of the bound vortex strength based on a non-entry boundary condition that is evaluated in the collocation points of each blade. The method is described in chapter 4.

AOA_condition.m

As an alternative to the direct non-entry boundary condition an iterative method can be used that is also described in chapter 4. This routine is however also capable of interpolating lift curves of the airfoils that are used along the blade.

release.m

A very simple function that releases new wake nodes at the trailing edge of each blade.

strength.m

Calculates the strength of the newly shed vortex filaments based on Kelvin's theorem. Also the value of the new trailing vortices are calculated using the principle of a superposition of multiple horseshoe vortices.

error_analysis

A simple tool to keep track of the convergence of the solution. If the difference in bound vortex strength between current and previous time step has reduced to a certain level convergence is achieved.

performance.m

Based on the lift distribution, TSR and RMP and U_∞ the performance parameters of the turbine can be calculated. Viscous drag based on $Cd - \alpha$ curves is not (yet) included here.

wake_plane.m

If one is interested in the induced velocities in a vertical disk at a certain downstream position in the wake this routine can be used to sample the wake for a predefined number of time steps.

A-2 Using the code

A-2-1 Data input structure

Input required on the operation of the turbine can be changed in the first lines of *Time_step.m*. Data on the geometry must however be loaded into the Matlab workspace. This data should be in *'.txt'* format and stored in a folder with a user defined name in the folder 'geometry'. The following text files must be present in the folder:

- **'Blade.txt'** contains the information on the root and tip radius and the number of blades.
- **'chord.txt'** contains the chord distribution as a function of the local span wise blade coordinate that is normalized with the blade length. The origin of this coordinate starts at the root of the blade.
- **'twist.txt'** contains the twist distribution as a function of the local span wise blade coordinate that is normalized with the blade length. The origin of this coordinate starts at the root of the blade.
- **'airfoil_input.txt'** gives the positions on the blade where a switch is made between airfoil type in local blade coordinate normalized with the blade length.
- Depending on the number of airfoils that are used along the blade, there should be an equal amount of text files each containing the $Cd - \alpha$ and $Cl - \alpha$ curves of every airfoil. For example the first airfoil is stored under the name **'airfoil_1.txt'**.

During the start-up of a simulation Matlab will prompt for the name of the folder where your geometric information is stored. By typing the name of your folder between quotes in the command window, Matlab will automatically load the correct data.

A-2-2 Data output structure

All data are stored in Matlab structs such that the output of the program is clarifying. This section discusses all structs that are used and what kind of data is stored.

aero The most important struct is the one with all aerodynamic information. This structure contains the values of the lift distribution, Vortex strengths, vortex core sizes, induced velocities in all points, angles of attack, inflow angles etc.

ini

All initial settings like tip speed ratio, free stream velocity, number of revolutions and time step are stored in this struct.

mesh

This struct contains all information on the current and previous position of the wake nodes.

rotor

All the relevant information of the current and previous position of the rotor is located here. Also the perceived wind velocity in each point due to the motion of the blade is stored here.

geom

All information by the subroutine *geometry.m* is stored in this struct. For example: blade twist and chord distributions, position of leading/trailing edge and position control/collocation points. All information is however expressed within the local blade coordinate system.

option

Options that are predefined before the simulation is activated are saved in the 'option' struct. The options can be user defined in the *Time_step.m* routine.

'wake' and 'sample'

These structs contain all information that is generated during the sampling of the wake at a certain downstream position. Each wake sample is stored in a separate sub-struct.

perform

The blade loads, shaft power and axial thrust are saved in this struct. Viscous drag based on $Cd - \alpha$ curves is not (yet) included here.

After the simulation Matlab tries to store the results in a folder with the same name that is given by the user at the beginning of the simulation in the folder called 'Results'. If the user has not created the correct directory in the 'Results' folder the simulation will be stored in the folder 'overige'.

A-2-3 Running the code

If the text files with the geometric information is stored in the right directory and a directory is created where the results can be stored, beginning the simulation is straightforward.

- Open the files **Time_step.m** and **geometry.m**. These are the only two files that are require attention before running a simulation
- In **geometry.m**: Select the number of blade nodes (N_b). Do not use a very high number since the computation time increases quadratically with N_b.
- In **Time_step.m**: Go to the cell 'Initial parameters'. Here you can set values as N_{rev}, N_ϕ and Tip Speed Ratio (TSR) and the free stream velocities. Use parameter U_inf_set to define the free stream velocity instead of U_inf.Note that a the computation time increases quadratically with N_ϕ!
- The initial rotation angles ϕ,ψ and θ are needed to translate the local blade coordinates to global coordinates. ϕ is the rotor azimuth position, ψ is the rotor yaw angle and θ is the rotor tilt angle.
- If the user is not interested in calculating the velocities in the wake then set *ini.sample_size* to zero. In **wake_plane.m** the resolution of the vertical disk can be defined.

- Go to the cell 'options'. Here you can define which options of the code are required for the simulation.
- Run the file **Time_step.m** and Matlab will ask for an input in the command window. Type here the name of the folder where your geometric data is stored between quotes. Make sure that you have also created a folder with the same name in the *'Results'* folder.
- If everything is set right now, the code should run without any problems or errors.

Appendix B

Geometrical information

B-1 NREL 5MW turbine

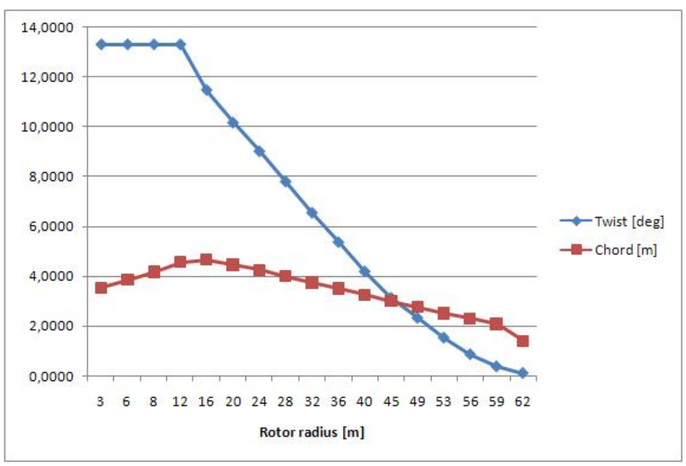

Figure B-1: Chord and twist distributions of NREL 5MW reference turbine

Table B-1: Specifications of NREL 5MW rotor

Parameter	Value	Unit
B	3	-
D	126	m
R_r	10.75	m
V_{rated}	12	m/s
$Hubheight$	87.6	m

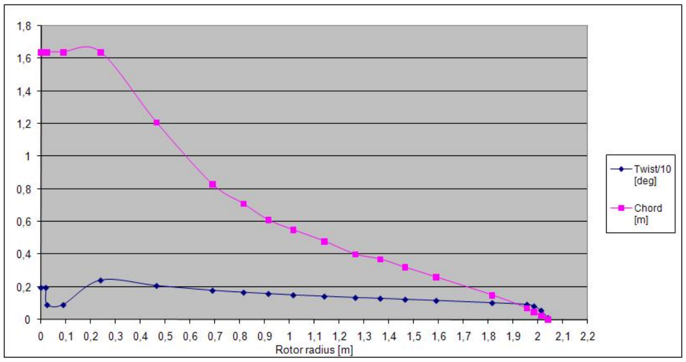

Figure B-3: Chord and twist distributions of MEXICO reference turbine

Table B-4: Specifications of MEXICO rotor, *Courtesy:* [8]

Parameter	Value	Unit
B	3	-
D	4.5	m
R_r	0.18	m
λ_{design}	6.7	-
V_{design}	15	m/s
C_p	0.45	-
C_t	0.89	-
$airfoil1$	$DU91-W2-250$, root	-
$airfoil2$	$RISA1-21$, mid span	-
; $airfoil3$	$NACA64-418$, outer part	-
; $Hubheight$	?	m

Appendix C

Roughness lengths

The following table gives typical values for the roughness length z_0 that are used in Wind Resource Assessment (WRA) and wind field models to describe the logarithmic profile of the earth's atmospheric boundary layer.

Table C-1: Roughness lengths, *Source:[29]*

Terrain classification	Rougness class	Roughness length [m]
Offshore, water areas	0.0	0.0002
Mixed water and land	0.5	0.0024
Very open farmland	1.0	0.0300
Open farmland	1.5	0.0550
Mixed farmland	2.0	0.1000
Trees and farmland	2.5	0.2000
Forests and villages	3.0	0.4000
Large towns and cities	3.5	0.8000
Large build up cities	4.0	1.6000

Table C-2: Shear exponents power law *source:[2]*

Roughness class	Rougness length	Wind gradient exponent
0	0.0002	0.1
1	0.03	0.15
2	0.1	0.2
3	0.4	0.3

Appendix D

Data fitting results

Table D-1: Coefficients a_n and b_n as suggested by RL model in [28]

Re_v	a_1	a_2	a_3	b_1	b_2	b_3
1	0	0	1.256	0	0	
1e2	1	0	0	1.2515	0	0
1e3	1	0	0	1.2328	0	0
1e4	0.8247	0.1753	0	1.2073	0.0263	0
2.5e4	0.5933	0.2678	0.1389	1.3480	0.01870	0.2070
4.8e4	0.4602	0.3800	0.1598	1.3660	0.01380	0.1674
7.5e4	0.3574	0.4840	0.1586	1.3995	0.01300	0.1636
1e5	0.3021	0.5448	0.1531	1.4219	0.0122	0.1624
2.5e5	0.1838	0.6854	0.1308	1.4563	0.0083	0.1412
5e5	0.1598	0.7167	0.1235	1.5584	0.0099	0.1834
7.5e5	0.1407	0.7420	0.1173	1.7228	0.0139	0.2592
1e6	0.1231	0.7667	0.1102	1.7912	0.0145	0.2733

The following table gives the results of the coefficients from the data fit. All coefficients are bounded by the maximum value of each coefficient in the previous table.

Table D-2: Coefficients a_n and b_n as found from data fit using the PIV measurements from the MEXICO project

Wake age [°]	a_1	a_2	a_3	b_1	b_2	b_3
120	0.6630	0	0.3374	1.3117	0.03000	0.1435
240	0.7158	0	0.2828	1.5178	0.03000	0.1614
360	0.6807	0	0.3191	1.2985	0.03000	0.1512
480	0.6233	0	0.3783	1.5477	0.03000	0.2538